NOVEL OPTICAL PROPERTIES IN SIZE TUNED CERIUM OXIDE CRYSTALS FOR FUNCTIONAL APPLICATIONS

THESIS SUBMITTED TO

COCHIN UNIVERSITY OF SCIENCE AND TECHNOLOGY
IN PARTIAL FULFILMENT OF THE REQUIREMENTS
FOR THE DEGREE OF

DOCTOR OF PHILOSOPHY
IN CHEMISTRY

UNDER THE FACULTY OF SCIENCE

BY

ASHA KRISHNAN

Under the Supervision of

Dr. Swapankumar Ghosh

Materials Science and Technology Division
NATIONAL INSTITUTE FOR INTERDISCIPLINARY SCIENCE AND TECHNOLOGY

Council of Scientific and Industrial Research
Thiruvananthapuram, Kerala, India – 695 019

November 2015

Declaration

I hereby declare that the work embodied in the thesis entitled "**NOVEL OPTICAL PROPERTIES IN SIZE TUNED CERIUM OXIDE CRYSTALS FOR FUNCTIONAL APPLICATIONS**" is the result of the investigations carried out by me, at the Materials Science and Technology Division, National Institute for Interdisciplinary Science and Technology (formerly Regional Research Laboratory), CSIR, Thiruvananthapuram, under the supervision of Dr. Swapankumar Ghosh and the same has not been submitted elsewhere for any other degree.

Asha Krishnan

Thiruvananthapuram
November 2015

Acknowledgements

My years at NIIST for the PhD programme from the joining period to the final design of the present thesis have had mentorship from numerous outstanding individuals both from within and outside the Institute. It is to these individuals, that my heartfelt gratitude and thanks go out to, for without their help, this thesis would not have seen possible.

Words fall short in expressing my immense gratitude to Dr. Swapankumar Ghosh, my research supervisor, Senior Principal Scientist, CG&CRI, Kolkata (formerly at NIIST, Thiruvananthapuram) whom I am obliged to in each and every step of the course. He provided me with the idea of the present work, valuable suggestions and expertise, which provided a good basis for the present thesis. He was always accessible and willing to help his students with their research and his friendly nature permitted us to clear even the minute scientific doubts. In addition, his understanding, support and personal guidance during adverse time helped me to complete the course in a satisfactory way.

I am extremely thankful to Dr. A. Ajayaghosh, present Director and former Directors of NIIST for providing the facilities to carry out this research work.

I am always indebted to Dr. U. S. Hareesh for the support rendered to me by him in the absence of my research supervisor and allowing me to access all the lab facilities freely. I would like to say a special word of thanks to Dr. K. G. K. Warrier for lending his valuable time in engaging with scientific discussions regarding my work. His detailed and constructive suggestions were crucial in planning the work and moulding it in the present form.

My deep and sincere thanks must go to Dr. S. Shukla, Dr. S. Ananthakumar and Dr. Balagopal N. Nair for their critical suggestions and advices during the course of my work. I also express my heart bound thanks to Dr. Sailaja G. S., Associate Professor, Department of Polymer Science and Rubber Technology, CUSAT, for her helping hands toward my PhD work. Her insight into nanotechnology was supportive to me during the various stages of my work.

I am extremely grateful to Mr. A. Peer Mohamed for extending his help any time in carrying out almost all of the characterisation presented in this thesis. Thanks are also due to Mr. P. Perumal for his support. Special gratitude goes to TEM and XRD groups of NIIST for their indispensible contributions to this work. I also thank all scientists and technical staffs of NIIST for their kind co-operation.

I am deeply beholden to Dr. Sree remya T.S., without her strong support, this thesis may not come into reality. I thank her for introducing me into the experimental

works presented in this thesis and making me familiarized with data analysis. She was always ready to help me, clear my queries and share my anxieties and I gratefully acknowledge the fruitful discussions with her. Besides, she has always been a source of motivation, both in personal and research life and I warmly cherish the companionship and affection which she has provided to me.

I wish to remember the smiling face of Dr. Jaimy K. B. for providing her full support, motivational advices and memorable friendship to me during the course. I gratefully thank her for spending her precious time in shaping the thesis in the final form. Ms. Shijina. K is specially acknowledged for helping me in designing the thesis. Special regards to Ms. Suyana P. for helping me to carry out certain characterisations presented in the thesis by making use of her broad friends circle in NIIST.

I always cherish the sincere support and warm friendship of my former colleagues Dr. Anas S., Dr. Smitha V. S., Dr. Manjumol K. A., Dr. Akhil K. Nair, Mr. Mirash, Mr. Divish and Mr. Senguttuvan, which made my days at NIIST memorable. I would like to thank all my buddies at the Functional materials lab, Dr. Sankar Sasidharan, Mr. Mahesh., Ms. Babitha, Ms. Harsha, Ms. Linsha, Ms. Mega, Mr. Manu, Ms. Minju Thomas, Ms. Swetha, Ms. Sumina, Ms. Subha, Ms. Vidhya, Mr. Sujith, Mr. Midhun, Mr. Firoz, Mr. Vaisakh, Mr. Balanand, Mr. Reymond, Ms. Soumya, Ms. Jeen Maria, Ms. Minju N. , Ms. Suhailath and Dr. Seethalekshmi Sunil. Their support, humour and companionship helped me to lessen tensions regarding research. I am thankful to them for making NIIST 'a home far away from home' to me.

During the period of my PhD course, I have accessed help from numerous other people from various institutes whom I wish to acknowledge. I thank Dr. Prabha D. Nair, SCIMST, Trivandrum, for water contact angle measurements. I am thankful to Mr. Mathew Joy and Ms. Srividhya J. Iyengar, CG&CRI, Kolkata for helping me to carry out XRD and XPS at their institute. I also remember their warm friendship throughout their stay at NIIST. I thankfully acknowledge Ms. Cinthya and Ms. Nimi (SCIMST, Trivandrum), Dr. Kala N. Raj, Dr. Beena K. B., Dr. Vijayadas K. N. and Mr. Jijil (NCL, Pune), Dr. Nandajan, Dr. Divya, Ms. Athira, and Ms. Remya (NIIST, Trivandrum) for their contribution toward my PhD work.

I acknowledge the Council of Scientific & Industrial Research, New Delhi, for the Research Fellowship.

I wish to gratefully acknowledge Dr. G. Rajendran, one of my teachers during my graduation studies, who has inspired and helped me to understand the basics of chemistry, which I believe was the stepping stone to all of my further achievements.

During this final stage of my doctoral studies, I feel the unseen presence of my loving parents and mother-in-law, who would have been over delighted at this golden moment of my life. I feel short of words while remembering the facilities my parents provided me to study well and I believe that this thesis has come into being from their heavenly blessings. My deepest gratitude goes to my loving husband, Mr. Raju Thankappan, who motivated and supported me throughout my ups and downs and this dissertation is simply impossible without him. I thank him for being a strong pillar near me, which helped me to complete the course by overcoming all the obstacles I faced in my life. I thank all my family members including my father-in-law, sisters, sister-in-law and others for their unflagging love and support throughout my life. I also wish to cherish the warm companionship of my childhood friends, Lekshmy, Resmi, Vrinda and Sini, who motivated me to balance both family and research life. This acknowledgement note will be totally incomplete if I do not mention my dearest little daughter, Prarthana, who might have missed my care and affection when I was busy with the thesis. I thank her for being a good baby when her 'mamma' was writing the thesis.

All of the above, I bow before ***'DEVI-The Almighty'*** *for, I believe, I could complete the course only because of the immense blessings showered to me by her and I dedicate this thesis before her.*

Thiruvananthapuram
20/11/2015

Asha Krishnan

CONTENTS PAGE

Preface

The physical dimensions of nanocrystals often serve as a resource of innovative photochemical properties and this makes nanotechnology a fascinating field of current research. Due to their nanoscale, usually smaller than the exciton Bohr radius, these 'artificial atoms' are called quantum dots and they render a wide range of applications endowed by the effect of quantum confinement. Also the high surface to volume ratio associated with nanoscaling of materials imparts enhancement in bulk properties with respect to the high fraction of atoms lying on or near the surface. Significant advances in current technologies and the potential for more revolutionary impacts in areas such as clean energy production, electronics, medicine, and environment have fuelled major research and development efforts in nanotechnology around the world. This leads to the opportunity to use such nanostructured materials in novel applications and devices.

The advances in nanotechnology have boosted the efficiency of many functionally significant materials like cerium dioxide. Cerium dioxide or ceria is one of the imperative rare earth oxides bestowed with unique properties like high thermal and chemical stability, UV absorption capability, hardness, redox nature, oxygen storage capacity, ionic conductivity, luminescence etc. The superior potential of ceria has been widely exploited for a variety of applications in fields like solid oxide fuel cells, cosmetics, chemical mechanical polishing, catalysis, gas sensing, oxygen permeation membrane systems etc. Infact, the vital source of the utility of ceria is its ability to exist in two stable oxidation states, +3 and +4 which are interconvertable depending on the oxygen partial pressure. The consequent oxygen vacancies in the crystal have been utilised as the key component for the fabrication of ceria based nano devices. Therefore, any aspect capable

of amplifying the oxygen vacancies circuitously improves the performance of such devices.

In accordance with previous studies, the size of ceria nanostructures is pivotal in determining the stoichiometric concentration of Ce^{3+} and the subsequent oxygen storage capacity of the domain. The size induced enrichment of oxygen vacancies is attributed to the high Ce^{3+} to Ce^{4+} ratio associated with the increased surface of the crystals, which makes size controlled synthesis of ceria nanostructures important. However, proper understanding of the effect of size reduction in the property as well as their roles in the activity of ceria at the atomic level is still lacking.

The present thesis addresses the size selective synthesis of ceria nanoparticles by facile ammonia precipitation and thermal decomposition methods with acetate or nitrate salts of cerium as precursor. Attempts have been made to study the size induced effects on the properties cerium dioxide and to tailor the novel properties for practical applications. The thesis contains four chapters in total. The first chapter provides introduction to nanomaterials, nanocrystalline ceria and its applications in a broad way. A brief and updated literature review on ceria nanoparticles, with special emphasis on the size selective synthesis and its multi functional applications are covered. Various synthetic procedures adopted for the synthesis of ceria nanoparticles are described in detail. Based on critical assessment of the reported information, the present research problem has been defined.

The second chapter describes the size controlled of ceria nanoparticles by thermal decomposition and ammonia precipitation method respectively with the aid of different surfactants. Among the various methods and surfactants used, ceria nanoparticles of

uniform size as small as 2 nm has been obtained *via* a thermal decomposition method with the aid of oleic acid as surfactant. The surfactant capping onto the particle surface ensured the ultra-small particles with a narrow size distribution and enabled the easy phase transfer of the synthesised particles into apolar solvents. The effective size reduction rendered by oleic acid has been explained on account of its kinked structure. The synthesized particles had been characterised by different analytical techniques and they exhibited size dependant optical properties such as a red-shift in absorption and band gap. As a result, the nanocrystals emit photons in the visible region with broad photoluminescence spectra, resulting in multi-coloured fluorescence. The novel properties has been explained on account of the defects which originated in the crystal lattice owing to the higher Ce^{3+} content of ceria while approaching molecular dimensions. Based on the observations, a mechanism had been proposed for the novel size dependent properties of ceria which has been rationalised by the XPS and Raman spectroscopy.

The third chapter involves the study of the concentration dependent quenching of the fluorescence exhibited by the nanoparticles in dispersion. The energy exchange phenomena of cerium oxide based nanoparticles in a medium have been inspected by means of a meticulous approach. A concentration dependent non-radiative pathway has been revealed to the particles in highly concentrated dispersions due to the close proximity between them, which rendered the extinction of fluorescence. The calibration plot according to the Stern-Volmer equation showed a good linear relationship within the error limit and the value of Q denoting exchange interaction was close to 6 implying dipolar coupling between particles. Analysis of spectroscopic data exposed that Förster

resonance energy transfer (FRET) is the dominant mechanism responsible for the interparticle excitation transfer and the distance calculated between particles according to Förster theory falls within the FRET limits. The distance dependence of FRET has been utilised to explicate the conformation and chain length of fatty acids by interrupting the energy transfer efficiency between particles and thus a simple analytical tool based on FRET for the qualitative assessment of fatty acids have been projected.

The fourth chapter covers the successful dispersion of nanoparticles in water to yield a stable aqueous dispersion and to tailor it as a 'turn-on' fluorescent sensor for vitamin C under ultra dilution. One of the major challenges in the implementing ceria as a sensor for a highly water soluble molecule like vitamin C is its inherent hydrophobicity. In the absence of any chemical modification, surface of ceria is hydrophobic due to their unique electronic structure, which prevents it from hydrogen bonding with interfacial water. The present chapter deals with the aqueous dispersion of the oleic acid capped nanoparticles, the surface of which is hydrophobic due to the surfactant. The particle surface had been rendered hydrophilic by giving a bilayer surface coating using oleic acid. The experimental conditions have been optimised to yield aqueous dispersions, which were stable for more than two months. The properties of the so modified particles have been investigated and compared with that before bilayer surface functionalisation. The redox property of the ceria dispersion and its realistic perspective as a vitamin C sensor by modulating the Ce^{3+} content have been demonstrated in this chapter. Vitamin C or ascorbic acid is a biologically important molecule, whose deficiency causes serious medical conditions and there are many analytical techniques developed so far towards its sensible detection, each of them having their own flaws and faults. The present work is

expected to receive much attention due to the efficiency of the method to sense vitamin C at a concentration as low as 6 μM with higher reproducibility, selectivity and rapidness. The method was adapted for the determination of vitamin C in various commercial pharmaceutical preparations and the recoveries obtained were in the satisfactory error limits.

Abbreviations

AOAC	Association of Official Analytical Chemists
BLNP	Bi-layer surfactant modified nanoparticles
CB	Conduction band
DA	Decanoic acid
DANP	Decanoic acid coated nanoparticles
DLVO	Derjaguin-Landau-Verwey-Overbeek
DOS	Density of states
FT-IR	Fourier Transform Infrared Spectroscopy
FRET	Förster resonance energy transfer
IB	Intermediate band
LoD	Limit of detection
MLNP	Monolayer surfactant modified nanoparticles
OA	Oleic acid
OANP	Oleic acid coated nanoparticles
OSC	Oxygen storage capacity
PAA	Polyacrylic acid
PANP	Polyacrylic acid coated nanoparticles
PCS	Photon correlation spectroscopy
PIS	Precipitant into salt
PL	Photoluminescence
QD	Quantum dot
RSD	Relative standard deviation
SA	Stearic acid
SANP	Stearic acid coated nanoparticles
SPR	Surface plasmon resonance
SIP	Salt into precipitant
TEM	Transmission Electron Microscopy
TGA	Thermogravimetric Analysis
UCNP	Uncoated nanoparticles
VB	Valence band
XPS	X-ray Photoelectron Spectroscopy
XRD	X-ray diffraction

CHAPTER 1

Introduction to Nanotechnology, Cerium dioxide, its size controlled synthesis and Functional Applications

1.1 Nanotechnology

In its original sense, 'nanotechnology' refers to the projected ability of constructing well defined structures of dimension in the order of ~100 nm, using techniques which are being developed to make high performance devices. More perceptibly, it is a technical design to understand, control and manipulate matter at the level of individual atoms and molecules. The theoretical prospective of this bottom-up process was envisioned as early as 1959 by Nobel laureate physicist, Richard P. Feynman in the famous lecture "There's Plenty of Room at the Bottom", given at California Institute of Technology.[1] Feynman considered the possibility of direct manipulation of individual atoms as a more powerful form of synthetic chemistry than those used at the time. The talk is considered to be a seminal event in the history of nanotechnology, as it inspired the conceptual beginnings of the field, decades later. Even though the term 'nanotechnology' was coined by Norio Taniguchi in 1974, the usage was widely accepted only after several years, mostly in the midst of 1980s. Another pioneer propagator of the technology was Eric Drexler, who proposed the idea of 'nanoscale assembly' in 1986.[2] Drexler's research works popularised a conceptual frame work for nanotechnology, which later flourished as a prominent field of science during the end of the 1980s and dragged worldwide attention. The major breakthrough in nanotechnology came up with the invention of scanning tunnelling microscopy in 1981, which allowed the visualisation of individual atoms and bonds.[3] Another

landmark in the advance of nanotechnology was the invention of fullerenes (C_{60}) in 1985, thus initialising the fabrication of nanodimension materials.[4]

Over years, nanotechnology has advanced as a major branch of science as well as engineering and in the modern era, it has transformed to a general purpose technique, owing to its significant impact on almost all areas including energy production, electronics, biomedical technology, food and agriculture, health care, textiles etc. The major interest behind this technology is laid on the unique properties endowed to the materials when their dimension falls in the nano range. There are mainly two basic size-dependent effects manipulating the properties of materials in the nano level, related to the fraction of atoms at the surface and quantum effects, which show discontinuous behaviour due to completion of shells in systems with delocalised electrons.[3] Surface plasmon resonance is another phenomenon influencing the properties of metal nanoparticles.[5]

(i) High Surface to Volume ratio

The enhanced number of surface atom play crucial role in the hyperactivity of nanoparticles compared to bulk materials. The surface property of nanomaterials could be better understood by considering the corresponding radius '*r*', when the particle size is transformed from bulk to nano. During this process, while the surface area of the sphere scales with the square of *r*, its volume extents as a function of r^3.[3] Generally, the fraction of atoms at the surface scales up according to the ratio of surface area to volume. Thus it could be presumed that the total number of atoms *N* varies with the inverse radius or diameter. Fig. 1.1 displays the schematic representation of this concept.

The atoms at the surface have few direct neighbours whereas bulk atoms are surrounded by other atoms proportionally enough to neutralise any inter particle interaction. Therefore surface atoms have a low mean coordination number and high residual valency, which enhances their surface energy. Consequently, in order to get rid of the excess energy, nanomaterials are persuaded to form bonds with other interacting molecules. In effect, compared to bulk, nanomaterials have high affinity for chemical reactions and are functionally more active.

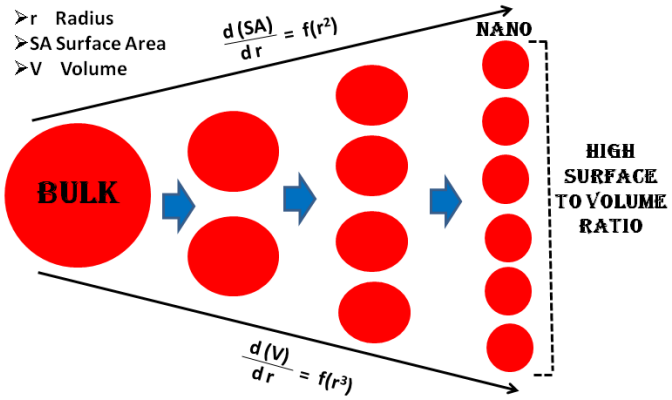

Fig. 1.1 Enhancement in aspect ratio of particles during the nanoscaling process.

A further consequence of the lower stabilisation of atoms at the surface is the lower melting point of surface layers. The inverse relation of melting point with radius of particle is very well known according to the Gibbs–Thomson equation [6]

$$\frac{\Delta T_{\mathrm{m}}}{T_{\mathrm{m}}^{*}} = \frac{2\,V_{\mathrm{m}}(l)\,\upsilon_{\mathrm{sl}}}{\Delta H_{\mathrm{m}} r} \qquad (1)$$

where T^{*}_{m} is the melting point of bulk, ΔT_{m} is the shift in melting point, when its dimension is scaled down to nano with a radius r, $V_{\mathrm{m}}(l)$ is the molar volume of the material, υ_{sl} is the interfacial tension between the solid and the liquid surface layer, and ΔH_{m} is the bulk latent heat of melting. As phase transition is a collective phenomena, the lowering of melting point of surface layers affect the whole process

with the absence of a sharper peak corresponding to the phase transition temperature. Nanomaterials usually resemble more to molecules than their own bulk and behave like isomers of molecules with distinct features, depending upon their position at surface or bulk.[3]

(ii) Quantum confinement Effect

Another outcome of the reduction in size of domains, comparable to the wavelength of electron, is the quantum confinement effect. The electronic organisation of molecules results in the creation of extended band structures and the total number of atoms contributes to the width of this band.[7] Furthermore, the density of states (DOS) within a band is proportional to the total number of atom in that ensemble. The DOS is in the order of number of atoms, *N* per eV, which is very large for bulk and low for nanomaterials.[8] Therefore, the band structure in bulk materials will be continuous whereas discontinuities arise in the case of nanomaterials. Many of the energy levels in the continuous band structure of the bulk will disappear due to the variation in DOS associated with the size reduction. As a result, the band structure is more or less quantised, leading to the formation of discrete energy levels. This quantisation of energy levels which is basically due to the restricted motion of electrons in the nanomaterials on account of the spatial confinement is generally called as quantum confinement.[9] More simply, the free motion of electrons in bulk materials in turn creates continuous energy levels in the band structure as the electronic environment remarkably varies with the position of electron. But in nanocrystals, the electron is allowed to move in a congested volume with only discrete energy levels in the band structure. As a result, most of the energy levels present earlier will be absent in nano crystals, which may influence the band-gap and

consequently the optical properties of the material. The theoretical perception of quantum confinement has been depicted in Fig. 1.2.

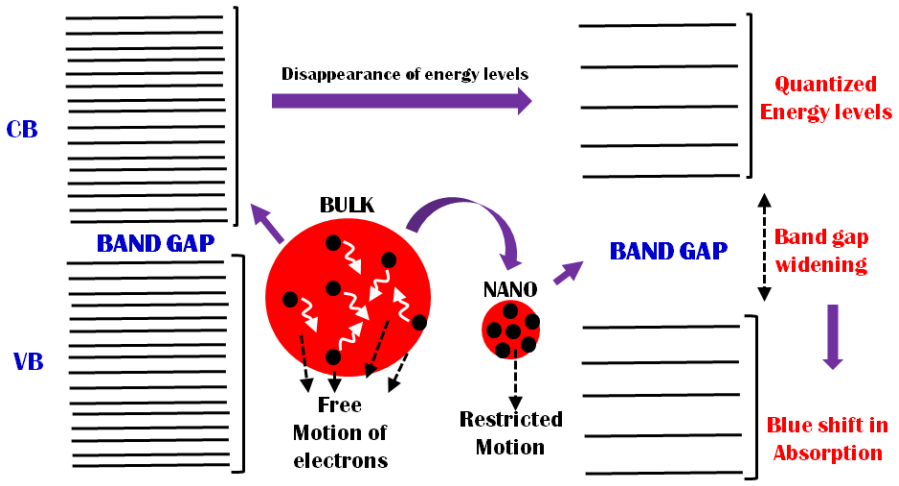

Fig. 1.2 Quantum confinement effects in the optical properties of semiconductor nanocrystals.

The effect of quantum confinement is more prominent in semiconductors, where the valence and conduction band is well separated in terms of band gap. The outcome would be best experienced in the optical properties of these materials with the widening of band gap, as shown in Fig. 1.2. This leads to the blue shift in their absorbance and emission properties, with an emission in the visible region.[10] Consequently, most of these semiconductor nanocrystals commonly called as 'quantum dots' are fluorescent; the emission colour being depends on the size of the crystal. In short, by adjusting the size of the quantum dots, their emission properties could be tuned, thus opening up newer possibility of using this material as an alternative for conventional organic flourophores. Applications of quantum dots includes light emitting diodes (LEDs), lasers, bioimaging, photovoltaics, quantum computing and other potential future devices involving quantum electronics such as anti-counterfeiting, defence applications etc.[11-14]

(iii) Surface Plasmon Resonance

Surface plasmon resonance is the resonant oscillation of conduction electrons stimulated by incident light at the interface between a negative and positive permittivity material. In materials like metals, the freely moving valence electrons are under the influence of restoring force exerted by the nuclei, thus inducing oscillations at the surface called as 'surface plasmons'. When an electromagnetic radiation of frequency similar to the natural frequency of surface plasmon strikes the interface, the radiation will be absorbed with the onset of collective surface oscillations called 'plasma oscillations' and the phenomenon is termed as 'surface plasmon resonance' (SPR).[15] The plasmon frequency is exquisitely sensitive to the surface properties and any surface changes like surface modification, aggregation etc. leads to shifting of plasmon frequencies and associated colorimetric change. In metal nanoparticles like Au and Ag, the plasmon frequencies is largely dependent on the size of the domain and upon irradiation with light, they exhibit different colours based on their size. Whereas, quantum confinement effect is the critical phenomenon controlling the optical properties of semiconductor nanocrystals, it is the SPR effects which determines the optical performance of metal nanoparticles.[15]

The impact of all these effects on nanomaterials enables the tuning of their chemical properties which has tremendously extended the potential of chemistry. Over the past two decades, owing to the significance of nanotechnology, scientists and engineers have been mastering the intricacies of working with nanoscale materials. The integrated technologies provided to society by unifying the features at the nanoscale with science are inestimable. In short, the privileges bestowed by nanotechnology could be reflected in our day to day life. Silver nanoparticles has been commonly used for anti-bacterial wound dressings.[1] Applications of gold

nanoparticles involve DNA detection, drug delivery, cancer therapy, bioimaging etc.[16] Nanocrystalline zinc selenide, zinc sulphide, cadmium sulphide and lead telluride are the candidates for the next generation light-emitting phosphors.[17] Nickel hydride batteries fabricated out of nanocrystalline Ni are envisioned to require less frequent recharging and long lasting owing to their large grain boundary.[18] It has been shown that magnets made of nanocrystalline yttrium–samarium–cobalt grains possess unusual magnetic properties due to their extremely large surface area, thus increasing the capacity of storage device based on these magnetic materials.[19] Nanocrystalline silicon carbide is a candidate material for artificial heart valves primarily because of its low density, high strength and inertness.[20] Nanomaterials based on carbon are being experimented as effective adsorbents for contaminants and desalination, in the process of water purification.[21] Carbon nanotubes (CNT), an allotrope of carbon have been explored for a variety of applications involving electronics and optics on account of their unique electrical properties.[22] Iron oxide nanoparticles have received significant attention as contrast agents for magnetic resonance imaging and as magnetic ferrofluids.[23] Ceramic oxides are also no way out of the influence of nanotechnology and oxides of cerium, zirconium, aluminium, zinc, and titanium are prominent oxides having immense applications as nanomaterials. Nanocrystalline zirconia is hard, wear resistant, bio-corrosion resistant and bio-compatible and is used as an alternative for bio-implants.[24] Nanoscale titania or zinc oxide has been incorporated in sunscreen lotions as they are transparent to UV radiations.[25]

Among the rare earth oxides, cerium oxide or ceria has attained special interest on the grounds of their high abundance, low cost and vast applications. Another merit of this oxide is the simplicity in its fabrication into 1, 2 and 3-dimensional

nanostructures.[26] On this background, there has been considerable interest on ceria based research, globally, especially in the nano level, in order to enhance the properties of the material and extract its utmost potential for the construction of functional devices. The present thesis is focused on the size controlled synthesis of ceria and investigation of the properties in association with its nano dimension. Further, attempts has been made to tailor the novel size dependent properties of these material for applications including identification of fatty acids and ultra dilute sensing of vitamin C. The other sections of this chapter put emphasis on the structure, physico-chemical properties, processing techniques, size controlled synthesis and functional applications of this versatile rare earth oxide.

1.2 Cerium dioxide

The history of cerium dioxide or cerium oxide, commonly called ceria started more than 220 years ago, when Klaproth found a black stone in Germany in the year 1803 and named as 'Ceres'.[27] It was actually named after an asteroid which was discovered two years earlier, which in turn was named for the Roman deity of agriculture. Concurrently, in the same year, it was also discovered independently by Berzelius and Hisinger at Sweden.[28] So the recognition for discovering this rare earth oxide is shared equally by the three chemists. The isolated ceria was then only 45% pure with the co-existence of almost all other lanthanides. In the 1830s, Carl Gustaf Mosander succeeded in obtaining pure ceria, after separating other lanthanides from it.[28] Ceria exists in the form of different minerals, monazite and bastnasite being the most important. Monazite and bastanite are the phosphates and carbonate-fluoride of cerium respectively. Among these, monazite deposits are found abundantly in India, especially in the beach sands of certain regions including Kollam, Kerala.

Ceria is visualised as pale yellow-white powder, slightly hygroscopic at atmospheric conditions. It is usually obtained by calcination of cerium salts. The electronic configuration of Ce atom is $[Xe]4f^2 6s^2$ and during chemical reactions, it usually exist as Ce^{4+} or Ce^{3+} ions by losing the 4f and 6s electrons. Stoichiometrically, it is expected that during the formation of the corresponding oxide, it combines with two moles of oxygen, by donating four electrons to form ceria with formula CeO_2.

Table 1.1 Generalized physical properties of stoichiometric ceria

Property	Value (Unit)
Molar Mass	172.1 g/mol
Appearance	Yellow Powder
Solubility	Insoluble in almost all solvents
Melting Point	2400°C
Boiling Point	3400°C
Lattice Constant	5.41Å
Hardness	6 (Mohs Scale)
Refractive index	2.1
Density	7.2 g/cm^3
Band Gap	4 eV
Absorbance	UV Region

But in reality, ceria is a non-stoichiometric oxide due to the mixed valence state (+4 and +3) of Ce ions in the oxide structure, which will be discussed in detail in the later sections of this chapter. Ceria is the most abundant among the rare earth oxides and is a technologically important material explored for their structural as well as chemical properties including non-toxicity, redox behaviour, oxygen storage capacity, ionic conductivity etc.[29-33] Another versatile properties of this material is its UV absorption capability, high hardness, thermal and chemical stability and high refractive index. Some of the physical properties endowed to this oxide have been tabulated in Table 1.1.

1.2.1 Structure of cerium dioxide

At ambient conditions, in its most stable state, ceria adopts a classic cubic fluorite structure (CaF_2) with a space group of $Fm\bar{3}m$.[34] The crystal lattice of ceria as depicted in Fig. 1.3 involves a face centred cubic arrangement of ions. Ce^{4+} ions are located at the corners as well as face centres of the lattice and oxide ions occupy the tetrahedral sites of the crystal. Therefore the coordination number of ceria is 8.[35]

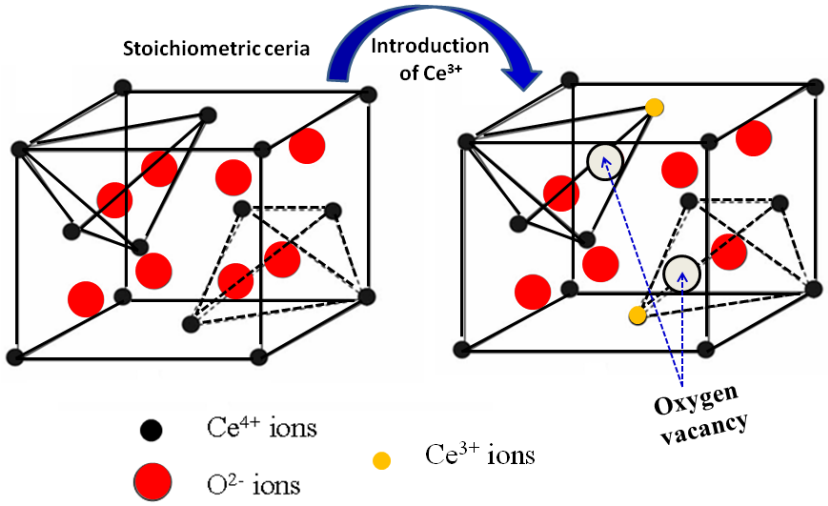

Fig. 1.3 Cubic Fluorite crystal structure of stoichiometric cerium oxide system and the creation of lattice oxygen vacancies by the replacement of Ce^{4+} with Ce^{3+}.

In the oxide structure of ceria, besides the +4 oxidation state, Ce ions can also exist as Ce^{3+} in stable state with one additional electron in the 4f energy level. Due to the similar energy of 4f and 5d electronic states, these two states can be flip-flopped in a redox reaction. The noteworthy fact is that, this interconversion can be effected at a low expense of energy ~1.7 eV and therefore the two oxidation states co-exist in the crystal facet of ceria even at room temperature.[36] Consequently, Ce^{3+} replaces Ce^{4+} in the crystal lattice of ceria, thus reducing the coordination of Ce ions to seven. In this event, in order to maintain charge neutrality, proportional amounts of oxygen will be released from the crystal. The Ce^{3+} would any time convert back to Ce^{4+} by the addition of oxygen in the crystal, depending upon the oxygen partial pressure of the

atmosphere. Thus in summary, the interconversion of the two oxidation states of ceria imparts an oxygen vacancy in the crystal structure of ceria as depicted in Fig. 1.3. The introduction of Ce^{3+} having a higher ionic radius (1.03 Å) than that of Ce^{4+} (0.92 Å) is succeeded by a series of alterations in the crystal symmetry. In order to compensate the strain associated with the occupancy of a larger ion in the crystal, it will undergo slight lattice expansion with a subsequent distortion in its symmetry.[35] In fact, the crystal structure of ceria varies from a perfect to distorted cubic fluorite type arrangement, depending upon the amount of Ce^{3+} in the lattice.

1.2.2 Redox behaviour and oxygen storage capacity of ceria

The prime recognition of ceria as a functional material is relied on its redox nature in association with the oxygen vacancies in the crystal. The cycling of cerium ions between Ce^{3+} and Ce^{4+} states impart ceria the ability to undergo oxidation as well as reduction reaction, depending upon the chemical environment.[37] Therefore, ceria is good mediator in redox reactions, which is comparable to that of biological antioxidants.

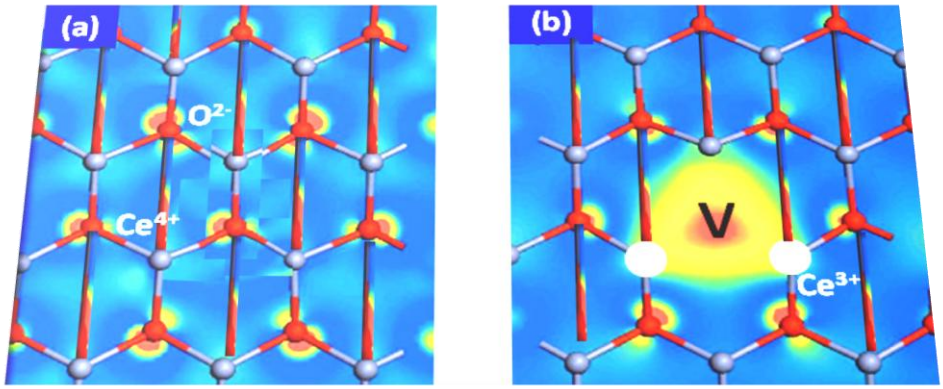

Fig. 1.4 Top-view model of ceria surface with (a) perfect crystal structure, and (b) defects due to the formation of oxygen vacancy (V).

Simultaneously, the mixed valency of cerium ions in ceria also facilitates the storage and release of oxygen from its surface commonly referred as the oxygen storage capacity (OSC). The mechanism of oxygen vacancy formation over the ceria surface has been displayed in Fig. 1.4

The stoichiometric representation of switching of Ce^{3+} and Ce^{4+} states in ceria is illustrated as equation (2).

$$2\ CeO_2 \leftrightarrow Ce_2O_3 + \frac{1}{2}\ O_2 \qquad (2)$$

Accordingly, the conversion of two Ce^{4+} to Ce^{3+} ions is followed by the evolution of oxygen from the lattice. When it reverts back to the initial state, the oxygen is added up to the vacancy. Equation (2) is a simple representation showing the complete reduction of Ce^{4+} to Ce^{3+}. The more realistic illustration of the concept is given as equation (3)

$$CeO_2 \rightarrow Ce_{(1-x)}\,(IV).\ Ce_x\,(III).\ O_{(2-\frac{x}{2})}.\ (\frac{x}{2})V_O^{\bullet\bullet} + \frac{x}{4}\,O_2 \qquad (3)$$

Virtually, both the oxidation states will be present in the lattice with the possibility of either release or absorbance of oxygen, which solely depends on the chemical environment as well as the partial pressure of atmospheric oxygen. This possibility has been theoretically notated as oxygen vacancy, $V_O^{\cdot\cdot}$.[35] The redox nature and related oxygen vacancy endows the oxide many versatile properties like anti-oxidant capacity, oxygen ion conductivity and catalytic ability involving redox reactions. The abundance of these 'intrinsic vacancies' which in turn determines the redox ability of ceria is tuneable with the Ce^{3+} concentration in the crystal and any aspect capable of amplifying the reduce state of Ce ions circuitously improves its redox ability.

Thermodynamically it is evaluated that Ce^{3+} segregates more at the surface than in the bulk. This assessment is based on the fact that the partial molar entropy of oxygen at the reduced surface is larger than that at the bulk.[38] Therefore at the surface, the

Ce ions exist mostly in the +3 oxidation state with remarkable stability. Thus, it could be understood that scaling down of the dimension of ceria crystals should attenuate the Ce^{3+}-to-Ce^{4+} ratio and related oxygen vacancies. In other words, it implies that nanoceria posses more oxygen vacancies and are more active than their bulk in accordance with its higher grain boundary. Deshpande *et al.* reported an enhancement in Ce^{3+} concentration by a factor of 15% when the particle size decreased from 6 to 3 nm.[35] Also with reference to literature, the shape of the nano structure is pivotal in determining the stoichiometric concentration of Ce^{3+} and the subsequent oxygen storage capacity of the nano domains. This is because, the stability of Ce^{3+} also varies with the energies of the various crystallographic facets of the crystal. Therefore, the abundance of oxygen vacancies will be concomitantly decided by the exposed planes of a particular morphology. For e.g., the studies by Mai *et al.* divulge that the experimental oxygen storage capacity was the highest for nanocubes compared to rods and polyhedra. They correlated the higher number of oxygen vacancies with the (100)-dominated surface of the nanocubes.[39] Besides, 'extrinsic oxygen vacancies' can also be introduced in ceria crystal by doping with tetravalent rare-earth oxides like samaria, yttria and gadolinia.[40] Overall, the redox property and associated oxygen vacancies in the ceria crystal could be controlled by varying the size and shape of the nano domains as well as the addition of dopants in the lattice.

1.2.3 Optical properties of ceria

Ceria is a renowned UV blocking material owing to the charge transfer transition from the O^{2-} (2p) to Ce^{4+} (4f) orbitals.[41] The band gap bulk ceria is ~4 eV with a strong absorption band in the UV A region of the electromagnetic spectrum.[42] O_{2p} is commonly considered as the valence band and Ce_{4f} as the conduction band of ceria. But certain researchers refer Ce_{4f} state as more or less atom like localised and

extended band of Ce_{5d} which is ~6 eV above the O_{2p} band.[42] However, the peak observed in the UV region is mostly assigned as transition to the Ce_{4f} level. The fact that Ce^{4+} ions have no 4f electron implies that it can be a promising luminescence host material due to strong light absorption through charge transfer from O– to –Ce.[43] But as its optical properties are more or less prevailed in the UV range, ceria is conventionally a non-luminescent material. However, the properties can be red shifted to visible region by the addition of suitable dopants. This is effected by the energy exchange between the charge transfer state of ceria to the dopants.[44] Rare earth elements are the common dopants for ceria, on account of their similar ionic radii and electronegativity.[44] Since the 4f electrons of these trivalent ions are well shielded from the surroundings, the emission transitions yield sharp lines in the spectra to produce strong emissions with distinctive colours due to their intra configurational transitions. The common dopant ions for ceria as host matrix are Sm^{3+}, Eu^{3+}, Tb^{3+} and Dy^{3+}.

Sm^{3+} doped ceria nanoparticles prepared by Wu *et al. via* poly vinyl alcohol assisted combustion reaction process could be effectively excited with 370 nm and emitted strong orange-red light, offering its application as high efficiency UV LEDs.[44] Luminescent films fabricated by Fujihara *et al.* using ceria as the host matrix with Eu^{3+} and Sm^{3+} as activators exhibited photons in the red region of visible spectra owing to the transfer of electrons from the excited Ce^{4+} energy levels to the dopant level.[45] Vimal *et al.* designed ceria based nanophosphors by the addition of Eu^{3+} by a thermal decomposition approach which displayed red emission, revealing the energy transfer between Ce^{4+} and dopant.[46] Kumar *et al.* doped ceria crystal with Eu^{3+} by a simple precipitation method and the crystals emit energy corresponding to a wavelength ~611 nm.[47] Thorot *et al.* observed a broad peak at ~608 nm for Eu^{3+}

doped ceria nanoparticles, which they have attributed to the Ce^{4+}–O^{2-} charge transfer of ceria with the overlap of intraconfigurational Eu 4f-4f transitions.[48] Nanostructured Tb^{3+} doped ceria film engineered by Ansari *et al.* through sol-gel technique exhibited a broad band in the blue region in association with the energy transfer between Ce^{4+} and the dopant ion.[49] Dutta *et al.* produced luminescent ceria by sonochemical method with Dy^{3+}, $Tb^{3+}$and Eu^{3+} as dopants which emits at blue, green and red region respectively.[43] Moreover, they also obtained white emission upon triply co-doping the ions, which show promise for adaptation as novel lighting device.

Besides, there are also certain secluded studies on the size dependent red shift of ceria nanoparticles. Accordingly, nano ceria exhibits a lower fundamental gap than their bulk, although the quantum-size effects are expected to induce a blue shift of the band gap.[42] In that case, the shift in optical properties is such that the particle emits in the blue- green region at ~400 nm. However, there are also controversial reports presenting the blue shift in the absorbance of ceria with size reduction.[50] The noteworthy fact is that the red shift and luminescence of bare ceria has been relatively less explored compared to its other research area. Therefore, a detailed understanding of the effect of the microstructure on the optical performance has to be carried out, which is one of the major objectives of the present study.

1.3 Impact of nanotechnology on ceria based research

The revolutionary impacts of nanotechnology have brought about beneficial leaps in material research contributed by several functionally active species. It is of no surprise that ceria based research was also stirred by the storms of nanotechnology. The preparation of polycrystalline ceria colloids by Matijevic *et al.* in 1988 is considered as the pioneer research involving nanoceria synthesis.[51] The strategy is

based on the forced hydrolysis of cerium salts and then the finest particle posses a size of ~30 nm. Since then numerous techniques has developed for obtaining high quality ceria nanocrystals with good control over size as well as morphology. In the present scenario, with the advance of nanotechnology, the accessible chemical methods allow the easy fabrication of ceria nanocrystals of size preferably below ~10 nm. Careful inspection of the literature on ceria undoubtfully establishes that the size of the ceria nanodomains constructively dominates their properties and applications, thus accentuating the significance of its size controlled synthesis. This motivates the world-wide ceria based scientific community to work with nanoceria with size as fine as possible, despite the kind of application they are focussing on.

1.3.1 Synthetic strategies for ceria nanoparticles

In a typical colloidal nanocrystals synthesis, under the prevailed reaction condition, the precursors chemically transform into active molecular species called 'monomers' which subsequently get converted into nanocrystals. Nanocrystal formation consists of two steps, of which the first one is the 'nucleation' involving the formation of numerous small crystallites called initial seed.[52] After nucleation, it undergoes various rearrangements and segregation involving additional monomers present in the reaction medium to form thermodynamically stable structures referred as 'crystal growth' process.[53] Suitable diffusion coefficient, concentration of the monomers and temperature are some of the deciding factors of the growth mode and size of the nanocrystals.[32] Also the synthetic technique and the related procedures are crucial in controlling the crystal size. The current synthetic routes for obtaining ceria crystals of size in the nano range include hydrolysis,[54] precipitation,[55] thermal deposition,[56] combustion or flame-synthesis,[57] sol–gel,[58] hydrothermal or solvothermal,[59] microemulsion,[60] gas condensation,[61] sonochemical,[62] electrochemical

techniques,[63] spray pyrolysis,[64] microwave heating[65] and so on. A brief overview of some of the commonly adopted synthetic methods is provided in the following section.

(i) Precipitation method

The aqueous precipitation technique is one of the commonly adopted methods on account of its advantages including simplicity, easy scale-up and cost efficiency.[66] This method involves the precipitation of the insoluble product from the parent precursor solution by the addition of precipitant. In a typical procedure, to a low concentration precursor solution, a suitable ligand is added, which triggers the formation of the corresponding product. Once the concentration of the product in the reaction media reaches the supersaturation level and exceeds the solubility limit, precipitation occurs.[67] In this process, the typical method of precipitating the solid-phase from the solution is pivotal in deciding the size of the final crystal. If the procedure involves rapid change of solution concentration and localisation of precipitant in the media due to its discontinuous addition, there is little control over the size of the particles. This type of heterogeneous nucleation requires less energy and therefore occurs more often. Instead if the precipitates are generated simultaneously and uniformly throughout the solution by the systematic addition of the precipitant ligand, a narrow range of size distribution can be achieved and the process is often referred as 'homogenous precipitation'. This method involves two different ways of addition of the precipitant, SIP (salt into precipitant) and PIS (precipitant into salt). It is believed that in the case of PIS method, the controlled release of the precipitant to the reaction media facilitates the formation finest size particle with least agglomeration.

For ceria, the precursor is predominantly a salt of Ce, commonly nitrates or chlorides. However, the precipitated species may be usually a precursor of the oxide, e.g., hydroxide or carbonate, which on thermal treatment transforms to the desired form after the elimination of gaseous products. Upon the addition of a base, say ammonia, $Ce(OH)_3$, will be formed, which will precipitate out due to its lower solubility product of $\sim 7\times10^{-24}$.[68] The +3 state will be oxidised in the oxygen atmosphere to form $Ce(OH)_4$, which upon drying get dehydrated to form the final oxide. The fine size of the oxide is ensured by the low precursor concentration which is nucleated to the oxide by homogenous precipitation. There have been numerous reports presenting the fabrication of nanoceria with size below 10 nm by adopting this technique, owing to its advantages. For example, Zhou *et al.* has produced 4 nm ceria by precipitating cerium nitrate using ammonia.[69] Fine ceria of size in the range of 2–4 nm has been prepared by Yamashita *et al.* from the chlorides of cerium using sodium hydroxide in the presence of hydrogen peroxide.[70] Ceria nanoparticles synthesised by Perez *et al.* by the aqueous precipitation of cerium nitrate using ammonia possessed an average size of ~4 nm.[71] Uekawa *et al.* achieved ceria particles of size in between 7–9 nm when cerium nitrate was precipitated in polyethylene glycol.[72]

(ii) Thermal decomposition process

The synthetic protocol of thermal decomposition process is based on the principle of breaking down of a thermally less stable nanoparticle precursor by the supply of heat from a high boiling solvent. Usually, organic solvents are adopted as the heat source, owing to its high boiling points and the method is generally a non-hydrolytic approach. The method was initiated by Bawendi and co-workers who successfully synthesized CdSe nanocrystals by injecting a solution of dimethyl cadmium and

trioctylphosphine selenide (TOPSe) into hot trioctlyphosphine oxide (TOPO).[73] They obtained highly monodisperse nanocrystals whose size could be tuned between 1.2 and 11.5 nm by varying the experimental conditions. Later, Hyeon *et al.* demonstrated the suitability of this method for large scale synthesis of nanoparticles. They synthesised bulk quantities of uniform-sized nanoparticles including Fe_3O_4, MnO and CoO in a single reaction without a size-sorting step.[74] Presently, this nonhydrolytic chemical route has developed as one of the most widely adopted methods for synthesising high-quality nanocrystals of metals, metal oxides and metal sulphides.[75]

The primary stage of this process involves the decision of the suitable reaction temperature which could provide enough thermal energy to decompose the precursor and allow rearrangement of atoms within a growing nanocrystal to form the final ultra small particles. Infact, one of the crucial factors which determine the success of this method is the perfect match between the decomposing temperature and boiling point of the precursor and solvent respectively.[52] The precursor, under the influence of heat decomposes rapidly to yield monomers, the reactive species of the process, which then diffuse into the reaction liquid.[75] When the liquid becomes supersaturated with monomer, they pass through the nucleation and growth stages and eventually crystallise along specific directions to form the final product.[75]

The concentration of precursor and temperature of reaction controls the size of the crystallised particles. The monomer concentration affects its diffusion coefficient in the reaction liquid which in turn decides the growth mode of the nanocrystals.[32] At low precursor concentrations, due to low diffusion flux of monomer in parent liquid, equilibrium is reached between dissolution and crystallisation, which restricts the crystal growth and produces fine crystals of similar growth patterns.[32] Increased

temperature of the reaction is beneficial because it speeds up the monomers to undergo nucleation and growth, but too much high temperature leads to uncontrolled growth.[52] Therefore the precise control of the reaction temperature and low precursor concentration are key factors controlling the size of the domains. The use of surfactant along with the precursor is also beneficial in controlling the size and their role requires special mention on the account of the ability to adhere on specific crystal facets and control further crystal growth.[76]

For the synthesis of metal oxide nanoparticles *via* thermal decomposition, the corresponding carboxylates are the commonly accepted precursors. It is believed that the decomposition process is accompanied by the formation of free radicals as intermediates. These radicals can undergo various reactions such as recombination, decay into smaller fragments, or propagate the decomposition by reacting with other carboxylate complexes which ultimately leads to the formation of the target metal oxide compounds.[77] In the case of ceria, during the heating up process, the precursor decomposes to generate free radicals including Ce-O$^{\cdot}$ and Ce$^{\cdot}$ which combine to form Ce–O–Ce links with the evolution of the final oxide structure.[78] Ceria nanostructures of size below 5 nm were fabricated by Lin *et al.* by thermally decomposing cerium acetate in 1-octadecane in the presence of oleic acid and oleyl amine.[56] Spherical ceria nanoparticles of tuneable size in the range 3 to 10 nm have been synthesised by Lee *et al.* by the thermal decomposition of different precursors including cerium acetylacetonate, cerium oleylamine and cerium nitrate using 1-octadecene as solvent and oleic acid as surfactant.[79] Monodisperse ceria nanoparticles of size as fine as 5 nm were prepared by Gu *et al.* by heating cerium oleate complex in octyl ether with the aid of oleic acid surfactant. By the thermal decomposition of ammonium cerium nitrate in a solution of diphenyl ether /oleic acid/oleyl amine, Imagawa *et al.* obtained

4 nm sized ceria particles.[80] Besides, our research group were also successful in synthesising ceria particles with an average size of ~5 nm by the thermal decomposition of cerium oleate in diphenyl ether in the presence of oleic acid and oleyl amine.

The nanocrystals fabricated *via* this non-aqueous thermal decomposition route, in general, exhibit excellent crystallinity and monodispersity compared to other aqueous routes. This can be explained on the basis of "separation of nucleation and growth" mechanism.[77] Accordingly, in thermal decomposition process, as all particles emerge virtually at the same time, their growth histories are nearly identical and remain independent from the nucleation event. Therefore, their size distribution will be exceptionally narrow and particles will be monodisperse in nature.[77] To summarise, by thermal decomposition route, a slow heating rate of precursor at a low concentration in suitable organic solvent in the presence of an efficient surfactant facilities slow and uniform rate of crystal growth, which ensures the formation of ultra fine and monodisperse particles.

(iii) Other Methods

Hydrothermal: The solvothermal synthesis of ceria nanoparticles under high pressure is renowned for the morphology controlled fabrication. The process is generally performed in an autoclave at temperatures between the boiling and critical points of solvents.[81] The temperature of the solvents can be brought to temperatures well above their boiling points by increasing autogenous pressure generated during heating. Whereas other synthetic methods of nanoceria demands the assistance of surfactants, activators or templates for the control over size and morphology, thus diminishing its active surface sites, this method is proficient in producing nanostructured ceria with bare surface. This method has been regarded as one of the

most effective and economical routes, as it has the merits of a single step low temperature synthesis, superior composition, morphological control and powder reactivity.[39] Uniform, crystalline nanostructures of ceria were synthesised by Yan *et al. via* the hydrothermal treatment of the corresponding nitrate in the presence of sodium phosphate as mineraliser. The morphology was tuned between octahedron and rod by adjusting the treatment time.[82]

Microemulsion: Microemulsion is an efficient method for producing highly monodisperse and fine ceria nanoparticles.[74] Microemulsion is generally defined as a thermodynamically stable system composed of two immiscible liquids and a surfactant.[60] In water-in-oil microemulsions, the aqueous phase is dispersed as nanosize water droplets covered with a monolayer film of surfactant and co-surfactant molecules in a continuous non-polar organic solvent such as hydrocarbons. As the surfactants are aligned in the emulsion in an opposite manner of their arrangement as micelle, this method is often called as 'reverse micellear process'. In a typical procedure, a microemulsion is made from the aqueous precursor solution in a non-polar solvent. As a second step, a water-in-oil emulsion is also prepared in which the aqueous phase consists of a chemical reagent capable of producing the target compound, metal oxide or metal from the precursor. The two microemulsions are mixed well and during this process, the micro aqueous droplets of precursor and the reagent continuously exchange their contents with one another.[60] In short, if two water-in-oil microemulsions are mixed, due to the reaction between the precursor and reagent, the final product will be formed in each micro droplet. As the reaction field is limited inside the fine reversed micelles, the particles obtained will be ultra fine with narrow size distribution.

There are several studies on the preparation of ultra fine ceria nanoparticles using this technique. For example, Masui *et al.* synthesised ceria nanoparticles of size below 5 nm from a water-in-oil microemulsion consisting of cerium nitrate and ammonium hydroxide in the aqueous phase.[60] Even though it is one of the proficient methods for nanoparticle synthesis, this process is difficult to scale- up, thus limiting its commercialisation.

Sonochemical Process: In recent years, nanomaterials have been extensively prepared by the so called 'sonochemistry' which involves irradiation by ultrasound waves. The attraction of this method is the ability to form ultra fine particles with high surface area.[83] The physical effects of ultrasound arise from acoustic cavitation, which is the formation, growth, and implosive collapse of bubbles occurring in a liquid medium.[84] During this process, an impactive force equivalent to a temperature of 5000°C, a pressure of ~20 MPa, and a very high cooling rate of 109°C/s could be attained at the location of the microbubbles. This could break down the larger particles to ultra fine size. For e.g., Gedanken *et al.* reported the preparation of 3.3 nm ceria particles by the sonochemical treatment of cerium nitrate and azodicarbonamide in the presence of ethylenediamine or tetraalkylammonium hydroxide as additives.[83]

Sol-gel method: The sol–gel method is a wet-chemical technique recognised for almost two centuries, which has been widely used for the processing of metal oxides and ceramic materials. This process includes the formation of a sol and gel state as intermediate stage. The starting solution typically consists of a precursor capable of forming integrated network of particles by undergoing various reactions. The commonly used precursor for metal oxide nanoparticles are their corresponding alkoxides or chlorides.[85] The process can be divided into different stages including a) hydrolysis of precursors-sol formation, b) polycondensation of hydrolysed precursors-

gelation, c) aging, d) drying, and e) calcinations. The hydrolysis of precursor solution results in the formation of sol which on ageing is converted into the gel form. Gel is a three dimensional structure of solid enclosing the solvent which on drying followed by calcination gives the final oxide particles. The sol-gel approach is a cheap and low-temperature technique that allows the fine control of the particle size and chemical composition. Owing to their advantages, this technique has been coupled with the manufacturing process of various metal oxides including ceria. Handy *et al.* has prepared ceria sol from its chloride salt using citric acid and ethanol. Thin films have been fabricated out of this sol, which has been utilized as an anti-corrosion coating for aluminium alloys.

1.3.2 Stabilisation of ceria nanoparticles

In the present scenario of ceria based research, it is unarguable that there are numerous facile and inexpensive solution techniques proficient in readily bringing down the size of this metal oxide to ultra fine level, as illustrated in the preceding section. The nanoscaling of this material has obviously boosted the efficiency of this material and broadened its techno-commercial importance as evidenced from the literature. But a key aspect which prevents its application as a dexterous nanomaterial is its inability to form stable dispersion. The tendency of nanomaterials to agglomerate in the dispersion, on account of the high surface to volume ratio is one of their inherent properties. The segregation of the particles eventually leads to their settling and the instability of the dispersion. This feature is more pronounced in ceria nano-system on account of their high density. Though this event does not have much impact on the applications involving powder reactivity, it certainly decreases the efficiency of ceria based devices involving liquid phase interactions. Under such a circumstance, stabilisation of ceria nanoparticles becomes highly relevant and there

are two major approaches for the fulfilment of this target based on the Derjaguin-Landau-Verwey-Overbeek (DLVO) theory.[86] Accordingly, the stability of nanoparticle in dispersions is determined by the combined influence of electrostatic, steric, and van der Waals forces among each other. The overall interparticle potential in a dispersion is given by

$$E = E_{vdW} + E_r \quad (3)$$

where E is the resultant energy over the particle , E_{vdW} and E_r are the contributions from the van der Waals attractive force and repulsive among the particles respectively.[87] If E_{vdW} overcomes $E_{r,}$ particles will attract each other and agglomerates. In the case of higher repulsive force in which $E_{vdW} < E_r$,the particles remain farther to each other and thus will form stable dispersions. The E_r can be bring about either by controlling the surface charge or co-ordinating with bulky groups and are usually called as electrostatic and sterric stabilisation, the principle being elaborated in the following section.

(i) Electrostatic stabilisation

The nanoparticle in its dispersion possesses a surface charge which might have developed through one or more of the following mechanisms:

(a) Preferential adsorption of ions

(b) Dissociation of surface charged species

(c) Isomorphic substitution of ions

(d) Accumulation or depletion of electrons at the surface

(e) Physical adsorption of charged species onto the surface

The surface charge in oxides is mainly derived from preferential dissolution or deposition of ions. Ions adsorbed on the solid surface determine the surface charge,

and they are referred to as charge determining ions, also known as co-ions. In the oxide systems, typical charge determining ions are protons and hydroxyl groups and as their concentration varies, the surface charge density changes from positive to negative or vice versa. When a surface charge density of a solid surface is established, there will be an electrostatic force between the nanoparticle surface and the charged species in the proximity to segregate positive and negatively charged species towards it. As a result a layer of oppositely charged ions called counter ions is introduced over the nanoparticle. This firm layer of counter ions is called a stern layer. At the same time, a layer of counter ions diffuse over the medium towards the stern layer which is only loosely attracted to the colloidal surface. This diffused layer of loosely bound ions in between stern layer and bulk is called Gouy-Chapman layer.[88] As the ions are farther from the nanoparticle, the electrostatic influence goes on decreasing and the bulk solution is usually neutral. This creates the formation of an 'electrical double layer' in the colloidal dispersion. Subsequently, there arises a potential difference across the double layer usually termed as the 'zeta-potential'.

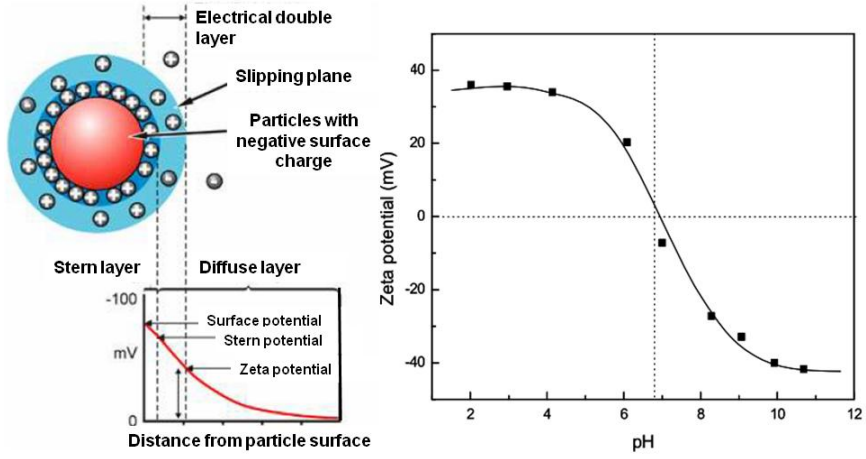

Fig. 1.5 Depiction of the principle of electrostatic stabilisation, by varying the zeta potential upon adjusting the pH.

The stability of the dispersion is highly influenced by the charge over the particle surface which is brought about by the repulsion of like charge. Higher the

charge density, higher is the repulsion and the dispersion will be consequently more stable. The thickness of the double layer is also another crucial factor influencing the stability. The stability can be well understood by measuring the zeta potential of the dispersion. Highly stable dispersions posses a zeta potential of absolute value between 25 and 30 mV.[89] As the thickness of the double layer proportionally increases the zeta potential and the consequent stability, addition of charged ions e.g., an acid or a base is expected to boost the stability of the dispersion. This is the basic principle of this approach, usually called as electrostatic stabilisation, in which the concentration of positive or negative ions in between the particles is increased by adjusting the pH. By doing so, the zeta potential is intensified, leading to the overall stability of the dispersion. From the graph depicted in Fig. 1.5, it could be assessed that at lower pH, due to the presence of high concentration of H^+ ions, the zeta potential attains a higher value, which goes on decreasing with increasing pH. At pH ~7, due to the scarcity of charged ions, the zeta potential drops to zero. Upon increasing the pH above 7, zeta potential value again increases, but to the negative side, due to the presence of OH^- ions.

Ceria in aqueous media preferably adsorbs hydroxyl ions and so it possesses a negative surface in the absence of any surface modification.[90] In order to stabilise ceria particle in aqueous media, it is desirable to increase the positive ion concentration in the phase, owing to its negative surface. Thus ceria is usually elctrostatically stabilised at lower pH. For example, Rane *et al.* prepared sol of ceria which was precipitated from cerium nitrate.[91] Ammonium hydroxide was the precipitant and the separated precipitate was employed for the preparation of sol. The sol was prepared by dispersing the washed precipitate in water followed by peptization using nitric acid at a pH range of 1.5-2.5.

(ii) Steric stabilisation

The stabilisation provided by the steric effects of bulky groups attached to the surface of nanoparticle is refereed as 'steric stabilisation'. This is achieved by the incorporation of a suitable surfactant molecule to the particle surface as a part of the synthetic pathway. The surfactant molecules in general are mutually unreactive as well as repulsive and have a long chain amphiphilic structure with a polar head group and non-polar tail.[92] It is able to get adsorbed over the particle surface by the polar head either physically or chemically. Such specific adsorption controls the crystal growth by sterically hindering the interaction between the particles and allows them to remain separated in dispersion. Eventually, the particles will be prevented from agglomeration, thus facilitating the stability of the dispersion and the principle is depicted in Fig. 1.6.

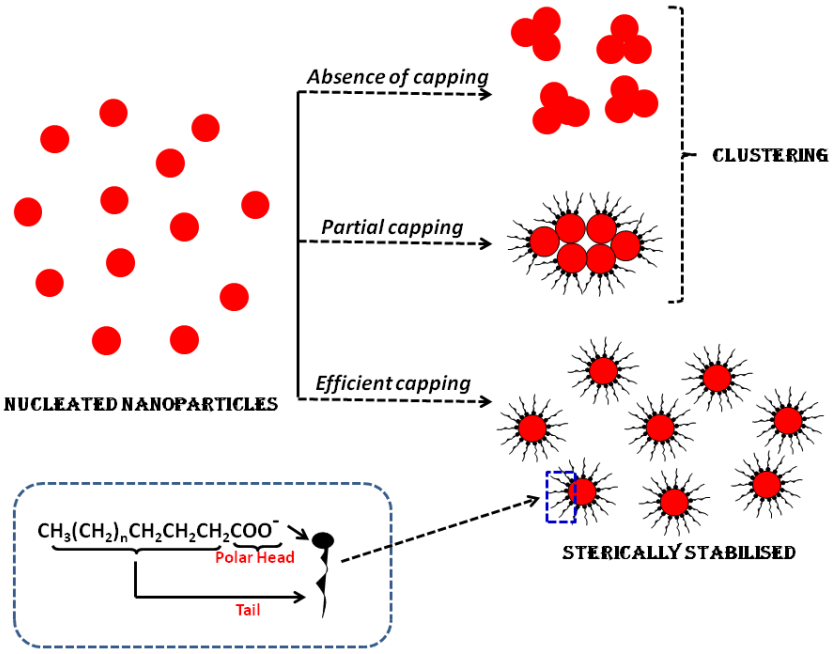

Fig. 1.6 Schematic representation of the steric stabilisation provided by surfactant over the nanoparticle surface.

Long chain fatty acids and polymers are variety of commonly used surfactants. Due to their particular manner of attachment, the non-polar tail will protrude out of

the particle surface, thus rendering it hydrophobic. Hence, along with steric stabilisation, the surface passivation also allows the particles to be dispersible in non-polar solvents like hexane, toluene etc.[93] Though surfactants possessing non-polar tails are efficient in producing monodisperse particles, the dispersibility of the particles are limited to non-polar solvents.[92] Hence the applications of the particles involving aqueous phase is adversely affected by surface coating involving these types of surfactants.[94] Sterically stabilised nanoparticles with hydrophilic surface can be engineered *via* two approaches. In the first method, the hydrophobic surface of the stabilised nanoparticles can be renovated to hydrophilic by chemical modifications.[95] Bilayer surface modification is one such approach in which a second layer of surfactant is grafted over the primary layer in a reversed fashion of attachment. This mode of surface passivation is initiated by Shimoiizaka *et al.* on iron oxide nanoparticles in the early 1980s. The particles, which were primarily coated with oleic acid is rendered hydrophilic by applying a second layer of sodium dodecylbenzene sulfonate, poly(oxyethylene) nonylphenyl ethers or di(2-ethylhexyl)-adipate.[96] Secondly, surfactants possessing polarity on both sides can be used as surface modifier. For example, poly ethylene glycol (PEG) is an amphiphilic molecule which is capable chelating the nanoparticle by the covalent bonding with oxygen. This particular manner of attachment lead to the outcrop of polar –OH groups over the nanoparticle surface, thus rendering it hydrophilic.[97]

The steric stabilisation of ceria nanoparticles is well documented in literature. Monodisperse ceria nanoparticles stabilised by oleic acid has been synthesised by Gu *et al.* by thermally decomposing oleate complex of cerium. They obtained fine and well separated particles with size preferably below 10 nm.[74] Kim *et al.* obtained ceria nanoparticle with size below 5 nm by the oxidation of cerium nitrate in a flow reactor

in the presence of decanoic acid as surface modifier.[98] Besides, a variety of modifying agents have been employed for the surface passivation of ceria particles including dextran, poly acrylic acid (PAA), polyethylene glycol (PEG), cetyl trimethyl ammonium bromide (CTAB), polyvinylpyrrolidone (PVP) and tetrabutylammonium bromide (TBAB).[79,99,100]

1.3.3 Ceria based dispersions

The propensity of nanoparticle to produce stable dispersion certainly adds merits to its functional significance as it boosts the liquid phase activity of the material. Stable dispersions of ceria consisting of nanoparticles stabilised by both steric and electrostatic means have been demonstrated by many researchers. Owing to the preferential adsorption of hydroxyl ions on surface, ceria can be elctrostatically stabilised at acidic pH. Preparation of stable ceria sol by peptization of precipitate using acids is well established. Due to the necessity of acidic conditions, this approach is less preferred for water based application. Instead, a variety of other methods have been employed. Non-aqueous dispersions of ceria could be successfully produced from nanoparticles modified with fatty acid like surfactants having non-polar tail. Accordingly, there have been numerous reports on stable non-polar dispersions of ceria. A brief literature review on the synthesis of stable ceria dispersions is provided in Table 1.2.

In summary, ceria dispersions could be successfully prepared by steric as well as electrostatic stabilisation. Whereas oleic acid was mostly adopted for the hydrophobic surface passivation of ceria, a variety of modifiers was employed for obtaining aqueous dispersions. Electrostatic stabilisation was also adopted for ceria dispersions but less frequently compared to steric approach, which may be due to the specificity of the acidic pH for the elctrostatically stabilised ceria sol. It could also be

observed that the studies related to ceria dispersion are scarce in number, perhaps because most of the renowned applications of ceria is carried out in solid phase.

Table 1.2 Literature review of ceria based dispersions

Stabilisation Approach	**Method of preparation**	**Surfactant**	**Particle Size & Morphology**	**Dispersion Medium**	**Reference No.**
Steric	Thermal decomposition	Oleic acid	5 to 10 nm, Spherical	Hydrocarbon solvents	[83]
Steric	Thermal decomposition	Oleic acid	3 nm, Spherical	Chloroform, THF, Toluene	[79]
Steric	Thermal decomposition	Oleic acid	2 nm, Rods	Toluene	[33]
Steric	Aqueous Precipitation	Oleic acid	2.2 nm, Spherical	Benzene, cyclohexane	[101]
Steric	Solvothermal	Oleic acid	5 nm, Polyhedra	Toluene	[50]
Steric	Thermal decomposition	Oleic acid	12-15 nm, Plate	Hexane	[56]
Steric	Bi layer coating	Co-polymer of PAA and Octyl amine	5.2 nm, Spherical	Water	[79]
Steric	Aqueous precipitation	Dextran	10 nm, Spherical	Water	[71]
Steric	Aqueous precipitation	PAA	2 nm, Spherical	Water	[102]
Steric	Sonochemical	PEG	10 nm, Rods	Water	[103]
Steric	Aqueous Precipitation	Glucose & Dextran	3-5 nm, Spherical	Water	[104]
Steric	Bilayer modification	Oleyl amine & Phospholipid-PEG	3 nm, Spherical	Water	[98]
Electrostatic	Precipitation/ Redispersion	-	10 nm, Spherical	Water	[105]
Electrostatic	Sol-gel technique	-	5 nm, Spherical	Water	[91]
Electrostatic	Sol-gel technique	-	30 nm, Spherical	Water	[51]

1.3.4 Overview of size reduction and related properties of ceria

The smallest ceria particles synthesised so far with the advent of nanotechnology is 1.8 nm by Yu *et al*. Monodisperse particles were synthesised by a hydrothermal hydrolysis reaction at 120°C using ammonium ceric nitrate as precursor in the presence of a double hydrophilic block copolymer.[106] Inoue *et al.* synthesised a colloidal solution of 2 nm sized ceria particles in 2-methoxyethanol directly from cerium metal by a solvothermal approach.[107] By aqueous precipitation, in the presence of oleic acid, oleophilic ceria particle of average size ~2.2 nm was fabricated by Tanigucchi *et al.* from cerium oleate complex.[101] Masui *et al.* successfully prepared 2.6 nm sized ceria nanoparticle by a reverse micellar method.[60] Briefly, the process involves the mixing of two microemulsions consisting of cerium nitrate and ammonium hydroxide in the presence of a surfactant, polyoxyethylene (10) octylphenyl ether. Uniform 3 nm sized ceria particles were obtained by Kim *et al.* from cerium acetate by a reverse micellar method.[98] Besides, there are numerous studies demonstrating the processing of ceria particles with size above 3 nm. With reference to literature, it could be assessed that even though ceria nanoparticles of dimension in the range of 3-10 nm could be easily fabricated by adopting common synthetic strategies, reports involving the achievement of size below 3 nm are limited.

Considering the size related properties of ceria, similar to other nanosystems, this oxide also displays enhancement in their bulk properties, owing to the high surface to volume ratio. Though the subsequent high surface area is one of the crucial factors in the overall activity, another significant parameter towards this view is the high Ce^{3+} -to- Ce^{4+} ratio of nanoceria. As mentioned in the previous sections, this could be better understood from a thermodynamical viewpoint. Accordingly, as the partial molar entropy of oxygen at the reduced surface is larger than that at the bulk,

Ce ions mostly exist in the +3 oxidation states at the surface.[38] Hence there will be subsequent increase in Ce^{3+}-to-Ce^{4+} ratio with reduction in size. This leads to the augmentation of the defect vacancy and oxygen storage capacity of ceria. As a result, the activity of ceria involving the effect of oxygen vacancy and Ce^{3+} concentration is highly enhanced. With reference to the studies by Soykal *et al.*, when the size of ceria was reduced from 120 nm to 3.5 nm, its catalytic performance towards the steam reforming of ethanol improved extremely.[108] Lee *et al.* observed that the antioxidant properties of ceria nanoparticles which in turn depend on the Ce^{3+}concentration were better for crystals with a diameter of 3.2 nm than those for crystals with a diameter of 8.2 nm.[79] Overall, the nanodimension of ceria is crucial in controlling its bulk properties, which allows the alteration of its physiochemical properties towards beneficial aspects.

While monitoring the size effects on the properties of ceria, a major gap which could be experienced is in terms of its optical behaviour. While, the vast application of semiconductor nanocrystals is relied on their novel optical properties associated with size reduction,[10] such an aspect is comparatively less explored in ceria system. In fact, the literature provides contrasting observations related to the optical behaviour of ceria. Ceria is reported to exhibit a lower fundamental gap than bulk, although the quantum-size effects are expected to induce a blue shift in absorbance due to the more localized bands.[42] Though short supplied, on the basis of studies detailing the optical properties of nanoceria, it could be assessed that the oxide displays a weak blue–green emission for particles with ultra fine dimension. Chunlin *et al.* initially reported visible blue photoluminescence from ceria thin films, the origin of which was attributed to the defects present in the crystal.[109] Morshed *et al.* observed a PL peak near 400 nm for ceria thin film deposited on silica substrate.[110] Choudhury *et al.*

demonstrated the photoluminescence with PL peaks at ~487 nm from 4 nm sized ceria particles.[111] Ceria nanoparticles of size ~3.7 nm prepared by Satyamurthy *et al.* through a reverse micellar approach displayed size induced optical properties leading to blue-emission.[112] Yu *et al.* reported a strong blue emission with an intense peak at 425 nm for ceria particles with size below 2 nm.[31] Similarly, Maensiri *et al.* also described PL peak in between 450 and 525 nm corresponding to blue green emission from platelet like ceria nanoparticle clusters with size below 10 nm.[113] The noteworthy fact is that majority of these studies includes only a mention of the visible emission of ceria nanoparticles. In general, it could be inferred that a detailed investigation of the size induced optical properties of ceria has not yet been established. It is also evident from literature that the exact mechanism behind the luminescent behaviour of undoped ceria particle is still a subject of dispute. This observation is based on the existence of contrasting reports referring to blue shift in optical properties of ceria with size reduction.[114]

1.3.5 Applications of cerium dioxide

Ceria is one of the essential rare earth oxides bestowed with unique properties and its superior potential has been widely exploited for a variety of applications in fields of electrochemistry, optics, catalysis, cosmetics and biotechnology. Apart from these customary uses, there are also certain outstanding footsteps towards the utility of ceria for distinct applications. Some of the conventional and non-conventional applications of ceria are detailed in the following sections.

1.4.1 Conventional Applications

One of the major technological applications of ceria is in three way catalysis involving the oxidation of toxic gases like carbon monoxide, hydrocarbons etc. as

well as reduction of nitrogen oxides. The role of ceria includes promoting the low temperature water-gas shift reaction. Because of its redox property, it can store and release oxygen under oxygen rich and lean conditions. Additionally, ceria can also stabilise precious metals like Pt, Rh, Pd, etc. against thermal damage and minimise the sintering of alumina washcoat which are various parts of the catalytic converter. The size as well as shape of ceria is the determining factor for the activity of ceria catalysts. While the high surface area and enhanced oxygen vacancies due to the high Ce^{3+}-to-Ce^{4+} ratio controls the size effects, the abundance of catalytically active crystallographic planes during the morphological evolution add up to the shape effects. Zhou and Huebner investigated the effect of ceria particle size and reported that the oxygen vacancies increased by 2 orders of magnitude when particle size was reduced from 60 to 4 nm.[115] Laachir *et al.* quantified reducing property of ceria with respect to particle size which was controlled by varying the calcination temperature.[116] Huang *et al.* observed strong morphology dependence of the ceria support in catalytic performance of Pt/CeO_2 in CO oxidation, and they correlated the activities with the exposed crystal planes and the surface structure/morphologies of ceria support.[117] Apart from water-gas shift reaction, there are numerous other chemical transformations in which ceria was found to impart efficient catalytic activity. The redox and acid–base properties of ceria allow this versatile oxide to activate complex organic molecules and to selectively orient their transformation. Mishra *et al.* have studied hydrogen transfer reaction of cyclohexanone with isopropanol over ceria-zirconia composite catalyst.[118] The catalyst showed 51.3 mol% conversion of cyclohexanone. Rose *et al.* demonstrated the catalytic activity of ceria towards the acetalisation of cyclohexanone with methanol producing dimethyl acetal.[119] Garcia *et al.* utilised nanocrystalline ceria as catalysts for the abatement of

polycyclic aromatic hydrocarbons.[120] Ceria has also been used as a catalyst for ketonization of small organic acids which is a valuable reaction for bio-renewable applications.[121] In the near future, the very rich chemistry of cerium oxide is expected to bring revolutionary impacts in the field of catalysis.

Another major application of ceria is as an oxygen ion conductor in solid oxide fuel cells (SOFC). SOFC is considered as one of the most promising power source of incoming decades because of its enhanced efficiency than well established fossil fuel combustion technologies and lower emissions.[122] A single SOFC unit consists of an anode, a cathode and a solid ceramic electrolyte that is sandwiched between the two. The charge transport in this fuel cell is facilitated by the migration of oxide ions from cathode to anode through the electrolyte membrane. For achieving efficient ion conductivity, SOFCs operates at temperatures as high as ~1000°C. The commonly adopted ceramic electrolytes strictly deliver efficient output only at elevated temperatures. In this aspect, ceria based solid oxide conducting electrolyte attracted more attention in the past two decades owing to its high oxide ionic conductivity at intermediate temperature in the range of 600–850°C. The main features of ceria based SOFC are low operating temperature, higher ionic conductivity, chemical inertness, high crystalline-phase and chemical purity.[123] Compared to pure phase of ceria, doped crystallites are usually preferred in SOFC on account of the enhanced ionic conductivity. Some of the common dopants are Gd, Sm, Zr, and Y.[122,124-126] Lin *et al.* fabricated fuel cell based on Sm-doped ceria (SDC) which performs well at intermediate temperatures.[122] Bellino *et al.* engineered SOFC based on nanostructured and heavily doped ceria electrolyte, which showed remarkable enhancement in the total ionic conductivity of about one order of magnitude compared with the conventional microcrystalline ceramics.[127] Gd-doped

ceria aerogels designed by Robert *et al*. exhibited efficient electrical transport at a moderate temperature of 600°C.[128] Simplicity in the cell fabrication and maintenance as well as attractive cell power output of ceria based SOFCs add merits to the utility of this technology towards energy production.

Cerium oxide has been conventionally explored as an efficient polishing agent for reducing surface roughness of various substrates. The principle of ceria based abrasive mainly involves chemical mechanical planarisation (CMP). CMP is a process that uses its slurry of an abrasive in a corrosive chemical to physically grind flat and chemically remove the microscopic topographic features on a wafer so that subsequent processes can begin from a flat surface.[129] The action of ceria includes both mechanical scraping as well as the chemical reactivity with substrate to weaken the material to be removed. In the case of glass substrate, the chemical reaction between the silica in glass and the cerium oxide particles causes the formation of Ce–O–Si linkage which weakens the Si–O–Si bonds. This eventually brings forth the rupturing of bonds in silica, leading to the efficient removal of material from substrate.[70] Cerium oxide powders are used in polishing spectacles, precision optics lenses for camera, CRT displays and they are also employed for removing scratched layers of glass to provide glossy surface.[130]

Considerable interest has been given to ceria based sunscreen materials on account of its UV blocking ability.[130] The characteristic features of ceria as an ingredient in sunscreen lotions are its absorbance in the UV region having band gap energy of ~4 eV along with appropriate refractive index of 2.1 as well as its poor photocatalytic activity.[42,131] Unlike other UV blocking materials like titania which oxidises sebum and degrade other ingredients in the sunscreen cosmetics owing to the higher photocatalytic activity, ceria remains inert and ensures better anti-damaging

effects to skin. Ceria has also been employed for the measurement of oxygen in many fields involving environment, industry, transportation, medicine and agriculture.[132] The possibility of using ceria as an oxygen sensor was first demonstrated by Beie and Gnorich.[133] The thin film of ceria prepared by screen printing technique followed $(PO_2)^{-1/6}$ behaviour within the oxygen partial pressure under study. Based on this report, numerous other studies have also been carried out later, which involve the design of ceria based sensors showing promising results for effective oxygen sensing.

1.4.2 Non - Conventional Applications

In the beginning of 21st century, the advance of science and technology has triggered the world-wide scientific community to explore materials that are proficient in bringing radical changes in the society. During this advent, ceria based research has presented a distinct perspective of this oxide as a functional material. One of such initial research was carried out by Corma *et al.* demonstrating its usability towards energy conservation.[41] Accordingly, the high surface area hierarchical mesoporous ceria structure exhibited linear photovoltaic response showing promise for fabrication of solar–cells based on this oxide. Later, many other researches have evolved which presents novel outlook of this versatile rare earth oxide. Inverse opal 3DOM ceria films engineered by Waterhouse *et al.* using a colloidal crystal template approach, exhibited photonic band gaps in the visible region, suggesting its application as an optical sensor.[131] Zhong *et al.* has showed the efficiency of ceria with 3D flower like morphology as a sorbent for the removal of pollutants in water treatment.[134] In 2006, the photovoltaic performance of this material was again explored by Krebs *et al.*, who devised a hybrid solar cell by incorporating a polymer with semiconductor oxide thin films including ceria.[135] Poly acrylic acid coated ceria nanoparticles synthesised by Wang *et al.* was proficient in inhibiting the growth of *Pseudomonas aeruginosa*, one

of the most significant bacteria infecting medical devices.[136] Some of the revolutionary reports on ceria in 2005 revealed the anti-oxidant property of ceria in cell culture media, which initiated the biological application of this rare earth oxide. Seal *et al.* exposed the protective action of ceria nanoparticles to normal human breast cell line from radiation induced cellular damage.[137] The studies carried out by Mcginnis *et al.* revealed the biological action of ceria in controlling retinal degeneration based on the efficiency of the particles to scavenge reactive oxygen intermediates.[138] Reports by Rzigalinski *et al.* in 2006 suggested the neuroprotective and anti-inflammatory properties of ceria nanoparticles.[139] Singh *et al.* illustrated the promising application of ceria nanoparticles for the treatment of neurodegenerative disorders like trauma, Alzheimer's and Parkinson's diseases, based on its anti-oxidant property.[140] These pioneer researches have ignited an area of ceria based research which persuaded a larger group of researchers to engage in the biomedical applications of ceria. This could be well established by giving a glance on the recent literatures on ceria, which mostly involves its biological applications. Hirst *et al.* revealed the anti-inflammatory properties of ceria nanoparticles by means of their ability to scavenge nitric oxide (NO) free radicals, the critical mediator of inflammation.[141] Suresh Babu *et al.* tuned ceria as a strong upconversion material capable of killing lung cancer cells and projected its versatility as an anti–cancer agent.[142] The medical and therapeutic application of ceria is also well established on account of its superoxide dismutase (SOD) mimetic activity.[143] More recently, Kim *et al.* presented the protective action of ceria against ischemic stroke.[98]

Besides, based on the redox property, ceria has also been explored as sensors for the determination of various chemical moieties which are tagged as either detrimental or indispensable stuffs.[132,144-148] Almar *et al.* developed a humidity

sensor based on Gd-doped mesoporous ceria which was thermally stable upto ~1000°C.[149] Hosseini *et al.* employed ceria as a part of electrode for the electroluminescent sensing a narcotic drug tramadol.[145] Gumpu *et al.* developed an electrochemical biosensor based on core-shell structure of ceria composite for the detection of histamine.[146] Singh *et al.* fabricated a ceria based biosensor with ceria for the detection of carbonic acid in blood.[147] Ceria nanostructure with a bowknot like morphology synthesised by Zhang *et al.* showed promise for sensing methyl orange.[148] Sen *et al.* demonstrated the applicability of ceria as a sensor for sulphur dioxide.[150] Abdelrahim *et al.* reported an electrocatalytic method involving ceria for the determination of ascorbic acid.[151] Sharpe *et al.* also demonstrated the sensing of ascorbic acid by a portable ceria nanoparticle-based assay which works on the principle of spectrophotometry.[152]

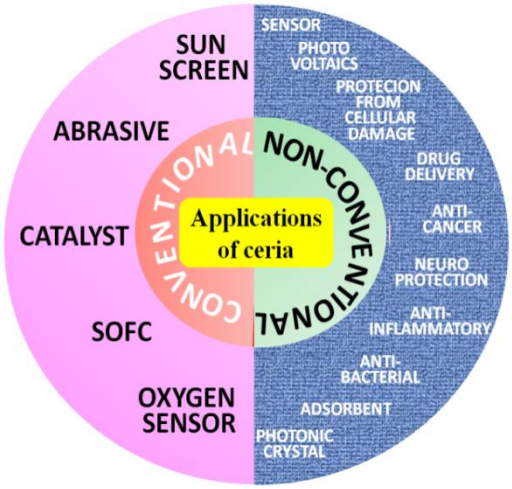

Fig. 1.7 Overview of the functional applications of ceria.

In summary, ceria is a multifunctional rare earth oxide employed for plentiful synchronized applications by virtue of their characteristic features as depicted in Fig.1.7. Ceria based research is still ongoing to extrude the maximum potential of this material for its safe and effective application.

1.5 Scope of the present thesis

Ceria is rare earth oxide having vast techno commercial significance which is relied on its redox activity and oxygen storage capacity. The impact of nanotechnology has radically boosted its efficiency and in the present era, nano ceria with size preferably below ~10 nm is employed for its conventional applications. Eventhough, nanoscaling has improved activity of its bulk property, in comparison with other semiconductor nanosystems, the optical properties of ceria during size reduction is relatively less explored. In fact, the optical properties of this material have been under the shadow of its other versatile properties. While other semiconductor nanocrystals find vast applications based on the novel optical properties derived from their ultra fine size, even fundamental stages of research from such a point of view is still not initiated for ceria. One of the major stumbling blocks towards this goal may be the difficulty in obtaining ultra fine and monodisperse ceria nanoparticles with size below 3nm. On such background, the present thesis aims at studying the size related properties of ceria and its functional applications. The primary stage of this target is the optimization of a suitable synthetic strategy for obtaining ultra fine ceria particles with size preferably below 3 nm. Secondly, the proper and detailed investigation of the size induced properties of this oxide has been carried out in comparison to crystals with varying particle size as well as with bulk. In the final section, attempts have been performed to modify the fine particles and tailor the novel properties for practical applications. Over all, the present thesis is an attempt to study the concealed aspect of ceria in order to broaden its importance so as to compete with other semiconductor nanocrystals of its own kind.

1.6 References

1 D. Bhattacharyya, S. Singh, N. Satnalika, A. Khandelwal and S. H. Jeon, *Nanotechnology*, 2009, **2**, 29-38.

2 A. Moscatelli, *Nat. Nanotechnol.*, 2013, **8**, 888-890.

3 E. Roduner, *Chem. Soc. Rev.*, 2006, **35**, 583-592.

4 L. Matija, *FME Trans.*, 2004, **32**, 1-14.

5 C. Noguez, *J. Phys. Chem. C*, 2007, **111**, 3806-3819.

6 M. Perez, *Scripta Mater.*, 2005, **52**, 709-712.

7 T. Takagahara and K. Takeda, *Phys. Rev. B*, 1992, **46**, 15578.

8 T. Inoshita and H. Sakaki, *Phys. Rev. B*, 1997, **56**, R4355.

9 W. K. Leutwyler, S. L. BÃrgi and H. Burgl, *Science*, 1996, **271**, 933-937.

10 X. Michalet, F. F. Pinaud, L. A. Bentolila, J. M. Tsay, S. Doose, J. J. Li, G. Sundaresan, A. M. Wu, S. S. Gambhir and S. Weiss, *Science*, 2005, **307**, 538-544.

11 X. Gao, Y. Cui, R. M. Levenson, L. W. K. Chung and S. Nie, *Nat. Biotechnol.*, 2004, **22**, 969-976.

12 D. Bimberg, N. N. Ledentsov, M. Grundmann, F. Heinrichsdorff, V. M. Ustinov, P. S. Kop'ev, M. V. Maximov, Z. I. Alferov and J. A. Lott, *Phys.E, 1998*, **3**, 129-136.

13 D. Loss and D. P. DiVincenzo, *Phys. Rev. A*, 1998, **57**, 120.

14 S. P. McGrew, *US6692031 B2*, 2004, **09/955**,808.

15 U. Kreibig and P. Zacharias, *Zeitschrift fÜr Physik*, 1970, **231**, 128-143.

16 R. A. Sperling, P. R. Gil, F. Zhang, M. Zanella and W. J. Parak, *Chem.Soc. Rev.*, 2008, **37**, 1896-1908.

17 A. Mueller, M. Hoffbauer and V. Klimov, *US20050230673 A1*, 2005, **11/089**,726.

18 G. Majeau-Bettez, T. R. Hawkins and A. H. Stramman, *Environ. Sci. & technol.*, 2011, **45**, 4548-4554.

19 R. V. Ramanujan, *Acad. Proc. eng. sci.*, 2003, **28**, 81-96.

20 V. Mahadevan and S. Sethuraman, *Nanomaterials and Nanosensors for Medical Applications,* in *Trends in Nanoscale Mechanics*. 2003, Springer. p. 207-228.

21 S. Wang, H. Sun, H.-M. Ang and M. O. Tade, *Chem. Eng. J*, 2013, **226**, 336-347.

22 R. H. Baughman, A. A. Zakhidov and W. A. de Heer, *Science*, 2002, **297**, 787-792.

23 H. Choi, S. R. Choi, R. Zhou, H. F. Kung and I. W. Chen, *Acad. Radiol.*, 2004, **11**, 996-1004.

24 K. Tomantschger, G. Palumbo and D. Facchini, *US20100076556 A1*, 2008, **12/232**,764.

25 T. G. Smijs and S. Pavel, *Nanotechnol. Sci. Appl.*, 2011, **4**, 95-112.

26 F. Gao, Q. Lu and S. Komarneni, *J. Nanosci. Nanotechnol.*, 2006, **6**, 3812-3819.

27 M. E. Weeks, *J. Chem. Educ.*, 1932, **9**, 1231-1235.

28 A. E. Williams-Jones, A. A. Migdisov and I. M. Samson, *Elements*, 2012, **8**, 355-360.

29 A. Trovarelli, *C.* de Leitenburg, M. Boaro and G. Dolcetti, *Catal. Today*, 1999, **50**, 353–367.

30 S. Tsunekawa, R. Sahara, Y. Kawazoe and A. Kasuya, *Mat. Trans. Jim*, 2000, **41**, 1104-1107.

31 X. J. Yu, P. B. Xie and Q. D. Su, *Phys. Chem. Chem. Phys.*, 2001, **3**, 5266-5269.

32 C. W. Sun, H. Li, H. R. Zhang, Z. X. Wang and L. Q. Chen, *Nanotechnology*, 2005, **16**, 1454-1463.

33 A. Ahniyaz, Y. Sakamoto and L. Bergstrom, *Cryst. Growth Des.*, 2008, **8**, 1798-1800.

34 S. Ghosh, D. Divya, K. C. Remani and T. S. Sreeremya, *J. Nanopart. Res.*, 2010, **12**, 1905-1911.

35 S. Deshpande, S. Patil, S. Kuchibhatla and S. Seal, *Appl. Phys. Lett.*, 2005, **87**, 133113.

36 C. Sun, H. Li and L. Chen, *Energ. Environ. Sci.*, 2012, **5**, 8475-8505.

37 A. Trovarelli, C. de Leitenburg, M. Boaro and G. Dolcetti, *Catal. Today*, 1999, **50**, 353-367.

38 W. C. Chueh, A. H. McDaniel, M. E. Grass, Y. Hao, N. Jabeen, Z. Liu, S. M. Haile, K. F. McCarty, H. Bluhm and F. El Gabaly, *Chem. Mater.*, 2012, **24**, 1876-1882.

39 H. X. Mai, L. D. Sun, Y. W. Zhang, R. Si, W. Feng, H. P. Zhang, H. C. Liu and C. H. Yan, *J. Phys. Chem. B*, 2005, **109**, 24380-24385.

40 M. Mogensen, N. M. Sammes and G. A. Tompsett, *Solid State Ionics*, 2000, **129**, 63-94.

41 A. Corma, P. Atienzar, H. Garcia and J. Y. Chane-Ching, *Nat. Mater.*, 2004, **3**, 394-397.

42 P. Patsalas, S. Logothetidis, L. Sygellou and S. Kennou, *Phys. Rev. B*, 2003, **68**, 035104.

43 D. P. Dutta, N. Manoj and A. K. Tyagi, *J. Lumin.*, 2011, **131**, 1807-1812.

44 J. Wu, S. Shi, X. Wang, J. Li, R. Zong and W. Chen, *J. Mater. Chem. C*, 2014, **2**, 2786-2792.

45 S. Fujihara and M. Oikawa, *J. Appl. Phys.*, 2004, **95**, 8002-8006.

46 G. Vimal, K. P. Mani, P. R. Biju, C. Joseph, N. V. Unnikrishnan and M. A. Ittyachen, *Appl. Nanosci.*, 2015, 1-10.

47 G. A. Kumar and N. V. Unnikrishnan, *J. Photochem. Photobiol., A*, 2001, **144**, 107-117.

48 A. V. Thorat, T. Ghoshal, P. Carolan, J. D. Holmes and M. A. Morris, *J. Phys. Chem. C*, 2014, **118**, 10700-10710.

49 A. A. Ansari, S. P. Singh and B. D. Malhotra, *J. Alloys Compd.*, 2011, **509**, 262-265.

50 F. Dang, K. Kato, H. Imai, S. Wada, H. Haneda and M. Kuwabara, *Cryst. Growth Des.*, 2010, **10**, 4537-4541.

51 W. P. Hsu, L. Ronnquist and E. Matijevic, *Langmuir*, 1988, **4**, 31-37.

52 Y. Yin and A. P. Alivisatos, *Nature*, 2005, **437**, 664-670.

53 X. D. Feng, D. C. Sayle, Z. L. Wang, M. S. Paras, B. Santora, A. C. Sutorik, T. X. T. Sayle, Y. Yang, Y. Ding, X. D. Wang and Y. S. Her, *Science*, 2006, **312**, 1504-1508.

54 M. Hirano and M. Inagaki, *J. Mater. Chem.*, 2000, **10**, 473-477.

55 T. S. Sreeremya, K. M. Thulasi, A. Krishnan and S. Ghosh, *Ind. Eng. Chem. Res.*, 2012, **51**, 318-326.

56 H. L. Lin, C. Y. Wu and R. K. Chiang, *J. Colloid Interf. Sci.*, 2010, **341**, 12-17.

57 R. D. Purohit, B. P. Sharma, K. T. Pillai and A. K. Tyagi, *Mater. Res. Bull.*, 2001, **36**, 2711-2721.

58 T. Y. Yu, J. Joo, Y. I. Park and T. Hyeon, *Angew. Chem. Int. Edit.*, 2005, **44**, 7411-7414.

59 C. Sun and L. Chen, *Eur. J. Inorg. Chem.*, 26, **2009**, 3883-3887.

60 T. Masui, K. Fujiwara, K. Machida, G. Adachi, T. Sakata and H. Mori, *Chem. Mater.*, 1997, **9**, 2197-2204.

61 L. MÃdler, W. J. Stark and S. E. Pratsinis, *J. Mater. Res.*, 2002, **17**, 1356-1362.

62 L. X. Yin, Y. Q. Wang, G. S. Pang, Y. Koltypin and A. Gedanken, *J.Colloid Interf. Sci.*, 2002, **246**, 78-84.

63 L. Arurault, P. Monsang, J. Salley and R. S. Bes, *Thin Solid Films*, 2004, **466**, 75-80.

64 H. Oh and S. Kim, *J. Aerosol Sci.*, 2007, **38**, 1185-1196.

65 H. Wang, J. J. Zhu, J. M. Zhu, X. H. Liao, S. Xu, T. Ding and H. Y. Chen, *Phys. Chem. Chem. Phys*, 2002, **4**, 3794-3799.

66 H. I. Chen and H. Y. Chang, *Ceram. Int.*, 2005, **31**, 795-802.

67 P. L. Chen and I. W. Chen, *J. Am. Ceram. Soc.*, 1993, **76**, 1577-1583.

68 H. I. Chen and H. Y. Chang, *Colloids Surf. A*, 2004, **242**, 61-69.

69 X. D. Zhou, W. Huebner and H. U. Anderson, *Appl. Phys. Lett.*, 2002, **80**, 3814.

70 M. Yamashita, K. Kameyama, S. Yabe, S. Yoshida, Y. Fujishiro, T. Kawai and T. Sato, *J. Mater. Sci.*, 2002, **37**, 683-687.

71 J. M. Perez, A. Asati, S. Nath and C. Kaittanis, *Small*, 2008, **4**, 552-556.

72 N. Uekawa, M. Ueta, Y. J. Wu and K. Kakegawa, *J. Mater. Res.*, 2004, **19**, 1087-1092.

73 C. Murray, D. J. Norris and M. G. Bawendi, *J. Am. Chem. Soc.*, 1993, **115**, 8706-8715.

74 H. Gu and M. D. Soucek, *Chem. Mater.*, 2007, **19**, 1103-1110.

75 Y. W. Jun, J. S. Choi and J. Cheon, *Angew. Chem. Int. Edit.*, 2006, **45**, 3414-3439.

76 L. Manna, E. C. Scher and A. P. Alivisatos, *J. Am. Chem. Soc.*, 2000, **122**, 12700-12706.

77 T. D. Schladt, T. Graf and W. Tremel, *Chem. Mater.*, 2009, **21**, 3183-3190.

78 T. S. Sreeremya, A. Krishnan, A. P. Mohamed, U. S. Hareesh and S. Ghosh, *Chem. Eng. J.*, 2014, **255**, 282-289.

79 S. S. Lee, W. Song, M. Cho, H. L. Puppala, N. Phuc, H. Zhu, L. Segatori and V. L. Colvin, *ACS Nano*, 2013, **7**, 9693-9703.

80 H. Imagawa, A. Suda, K. Yamamura and S. Sun, *J. Phys. Chem. C*, 2011, **115**, 1740-1745.

81 B. L. Cushing, V. L. Kolesnichenko and C. J. O'Connor, *Chem. Rev.*, 2004, **104**, 3893-3946.

82 L. Yan, R. B. Yu, J. Chen and X. R. Xing, *Cryst. Growth Des.*, 2008, **8**, 1474-1477.

83 J. X. Guo, X. Q. Xin, X. Zhang and S. S. Zhang, *J. Nanopart. Res.*, 2009, **11**, 737-741.

84 J. Kis-Csitari, Z. Kaniya and I. Kiricsi, *Sonochemical Synthesis of Inorganic Nanoparticles*, in *Functionalized Nanoscale Materials, Devices and Systems*. 2008, Springer. p. 369-372.

85 J. H. Park, P. Muralidharan and D. K. Kim, *Mat. Lett.*, 2009, **63**, 1019-1022.

86 C.-J. Chin, S. Yiacoumi and C. Tsouris, *Langmuir*, 2001, **17**, 6065-6071.

87 R. Tadmor, R. E. Rosensweig, J. Frey and J. Klein, *Langmuir*, 2000, **16**, 9117-9120.

88 K. B. Oldham, *J. Electroanal. Chem.*, 2008, **613**, 131-138.

89 M. Bloemen, W. Brullot, L. Tai Thien, N. Geukens, A. Gils and T. Verbiest, *J. Nanopart. Res.*, 2012, **14**.

90 M. Nabavi, O. Spalla and B. Cabane, *J. Colloid Interf. Sci.*, 1993, **160**, 459-471.

91 N. Rane, H. Zou, G. Buelna and J. Y. S. Lin, *J. Membrane Sci.*, 2005, **256**, 89-97.

92 R. De Palma, S. Peeters, M. J. Van Bael, H. Van den Rul, K. Bonroy, W. Laureyn, J. Mullens, G. Borghs and G. Maes, *Chem. Mater.*, 2007, **19**, 1821-1831.

93 L. Shen, A. Stachowiak, S.-E. K. Fateen, P. E. Laibinis and T. A. Hatton, *Langmuir*, 2001, **17**, 288-299.

94 A. Prakash, H. Zhu, C. J. Jones, D. N. Benoit, A. Z. Ellsworth, E. L. Bryant and V. L. Colvin, *ACS Nano*, 2009, **3**, 2139-2146.

95 D. Liu and P. T. Snee, *ACS Nano*, 2010, **5**, 546-550.

96 N. Jain, Y. J. Wang, S. K. Jones, B. S. Hawkett and G. G. Warr, *Langmuir*, 2009, **26**, 4465-4472.

97 A. S. Karakoti, S. Das, S. Thevuthasan and S. Seal, *Angew. Chem. Int. Edit.*, 2011, **50**, 1980-1994.

98 C. K. Kim, T. Kim, I. Y. Choi, M. Soh, D. Kim, Y. J. Kim, H. Jang, H. S. Yang, J. Y. Kim and H. K. Park, *Angew. Chem. Int. Edit.*, 2012, **124**, 11201-11205.

99 A. l. Vantomme, Z.-Y. Yuan, G. Du and B.-L. Su, *Langmuir*, 2005, **21**, 1132-1135.

100 C. Pan, D. Zhang and L. Shi, *J. Solid State Chem.*, 2008, **181**, 1298-1306.

101 T. Taniguchi, T. Watanabe, N. Sakamoto, N. Matsushita and M. Yoshimura, *Cryst. Growth Des.*, 2008, **8**, 3725-3730.

102 V. K. Ivanov, A. V. Usatenko and A. B. Shcherbakov, *Russ. J. Inorg. Chem.*, 2009, **54**, 1522-1527.

103 H. Wang, J. J. Zhu, J. M. Zhu, X. H. Liao, S. Xu, T. Ding and H. Y. Chen, *Phys. Chem. Chem. Phys*, 2002, **4**, 3794-3799.

66 H. I. Chen and H. Y. Chang, *Ceram. Int.*, 2005, **31**, 795-802.

67 P. L. Chen and I. W. Chen, *J. Am. Ceram. Soc.*, 1993, **76**, 1577-1583.

68 H. I. Chen and H. Y. Chang, *Colloids Surf. A*, 2004, **242**, 61-69.

69 X. D. Zhou, W. Huebner and H. U. Anderson, *Appl. Phys. Lett.*, 2002, **80**, 3814.

70 M. Yamashita, K. Kameyama, S. Yabe, S. Yoshida, Y. Fujishiro, T. Kawai and T. Sato, *J. Mater. Sci.*, 2002, **37**, 683-687.

71 J. M. Perez, A. Asati, S. Nath and C. Kaittanis, *Small*, 2008, **4**, 552-556.

72 N. Uekawa, M. Ueta, Y. J. Wu and K. Kakegawa, *J. Mater. Res.*, 2004, **19**, 1087-1092.

73 C. Murray, D. J. Norris and M. G. Bawendi, *J. Am. Chem. Soc.*, 1993, **115**, 8706-8715.

74 H. Gu and M. D. Soucek, *Chem. Mater.*, 2007, **19**, 1103-1110.

75 Y. W. Jun, J. S. Choi and J. Cheon, *Angew. Chem. Int. Edit.*, 2006, **45**, 3414-3439.

76 L. Manna, E. C. Scher and A. P. Alivisatos, *J. Am. Chem. Soc.*, 2000, **122**, 12700-12706.

77 T. D. Schladt, T. Graf and W. Tremel, *Chem. Mater.*, 2009, **21**, 3183-3190.

78 T. S. Sreeremya, A. Krishnan, A. P. Mohamed, U. S. Hareesh and S. Ghosh, *Chem. Eng. J.*, 2014, **255**, 282-289.

79 S. S. Lee, W. Song, M. Cho, H. L. Puppala, N. Phuc, H. Zhu, L. Segatori and V. L. Colvin, *ACS Nano*, 2013, **7**, 9693-9703.

80 H. Imagawa, A. Suda, K. Yamamura and S. Sun, *J. Phys. Chem. C*, 2011, **115**, 1740-1745.

81 B. L. Cushing, V. L. Kolesnichenko and C. J. O'Connor, *Chem. Rev.*, 2004, **104**, 3893-3946.

82 L. Yan, R. B. Yu, J. Chen and X. R. Xing, *Cryst. Growth Des.*, 2008, **8**, 1474-1477.

83 J. X. Guo, X. Q. Xin, X. Zhang and S. S. Zhang, *J. Nanopart. Res.*, 2009, **11**, 737-741.

84 J. Kis-Csitari, Z. Kaniya and I. Kiricsi, *Sonochemical Synthesis of Inorganic Nanoparticles*, in *Functionalized Nanoscale Materials, Devices and Systems*. 2008, Springer.

85 J. H. Park, P. Muralidharan and D. K. Kim, *Mat. Lett.*, 2009, **63**, 1019-1022.

86 C.-J. Chin, S. Yiacoumi and C. Tsouris, *Langmuir*, 2001, **17**, 6065-6071.

87 R. Tadmor, R. E. Rosensweig, J. Frey and J. Klein, *Langmuir*, 2000, **16**, 9117-9120.

88 K. B. Oldham, *J. Electroanal. Chem.*, 2008, **613**, 131-138.

89 M. Bloemen, W. Brullot, L. Tai Thien, N. Geukens, A. Gils and T. Verbiest, *J. Nanopart. Res.*, 2012, **14**.

90 M. Nabavi, O. Spalla and B. Cabane, *J. Colloid Interf. Sci.*, 1993, **160**, 459-471.

91 N. Rane, H. Zou, G. Buelna and J. Y. S. Lin, *J. Membrane Sci.*, 2005, **256**, 89-97.

92 R. De Palma, S. Peeters, M. J. Van Bael, H. Van den Rul, K. Bonroy, W. Laureyn, J. Mullens, G. Borghs and G. Maes, *Chem. Mater.*, 2007, **19**, 1821-1831.

93 L. Shen, A. Stachowiak, S.-E. K. Fateen, P. E. Laibinis and T. A. Hatton, *Langmuir*, 2001, **17**, 288-299.

94 A. Prakash, H. Zhu, C. J. Jones, D. N. Benoit, A. Z. Ellsworth, E. L. Bryant and V. L. Colvin, *ACS Nano*, 2009, **3**, 2139-2146.

95 D. Liu and P. T. Snee, *ACS Nano*, 2010, **5**, 546-550.

96 N. Jain, Y. J. Wang, S. K. Jones, B. S. Hawkett and G. G. Warr, *Langmuir*, 2009, **26**, 4465-4472.

97 A. S. Karakoti, S. Das, S. Thevuthasan and S. Seal, *Angew. Chem. Int. Edit.*, 2011, **50**, 1980-1994.

98 C. K. Kim, T. Kim, I. Y. Choi, M. Soh, D. Kim, Y. J. Kim, H. Jang, H. S. Yang, J. Y. Kim and H. K. Park, *Angew. Chem. Int. Edit.*, 2012, **124**, 11201-11205.

99 A. l. Vantomme, Z.-Y. Yuan, G. Du and B.-L. Su, *Langmuir*, 2005, **21**, 1132-1135.

100 C. Pan, D. Zhang and L. Shi, *J. Solid State Chem.*, 2008, **181**, 1298-1306.

101 T. Taniguchi, T. Watanabe, N. Sakamoto, N. Matsushita and M. Yoshimura, *Cryst. Growth Des.*, 2008, **8**, 3725-3730.

108 I. I. Soykal, H. Sohn, D. Singh, J. T. Miller and U. S. Ozkan, *ACS Catal.*, 2014, **4**, 585-592.

109 C. L. Chai, S. Y. Yang, Z. K. Liu, M. Y. Liao and N. F. Chen, *Chinese Sci. Bull.*, 2003, **48**, 1198-1200.

110 A. H. Morshed, M. E. Moussa, S. M. Bedair, R. Leonard, S. X. Liu and N. ElMasry, *Appl. Phys. Lett.*, 1997, **70**, 1647-1649.

111 B. Choudhury, P. Chetri and A. Choudhury, *RSC Advances*, 2014, **4**, 4663-4671.

112 S. Sathyamurthy, K. J. Leonard, R. T. Dabestani and M. P. Paranthaman, *Nanotechnology*, 2005, **16**, 1960-1964.

113 S. Maensiri, C. Masingboon, P. Laokul, W. Jareonboon, V. Promarak, P. L. Anderson and S. Seraphin, *Cryst. Growth Des.*, 2007, **7**, 950-955.

114 P. Patsalas, S. Logothetidis and C. Metaxa, *Appl. Phys. Lett.*, 2002, **81**, 466-468.

115 X. D. Zhou and W. Huebner, *Appl. Phys. Lett.*, 2001, **79**, 3512.

116 A. Laachir, V. Perrichon, A. Badri, J. Lamotte, E. Catherine, J. C. Lavalley, J. f. El Fallah, L. Hilaire, F. l. Le Normand and E. Quamar, *J. Chem. Soc., Faraday Trans.*, 1991, **87**, 1601-1609.

117 W. Huang, *Top. Catal.*, 2013, **56**, 1363-1376.

118 B. G. Mishra, G. R. Rao and B. Poongodi, *J. Chem. Sci.*, 2003, **115**, 561-571.

119 K. J. P. Rose and S. Sugunan, *IOSRJAC*, 2012, **1**, 24-29.

120 T. Garcia, B. Solsona and S. H. Taylor, *Catal. Lett.*, 2005, **105**, 183-189.

121 R. W. Snell and B. H. Shanks, *ACS Catalysis*, 2013, **3**, 783-789.

122 Y. Lin, C. Su, C. Huang, J. S. Kim, C. Kwak and Z. Shao, *J. Power Sources*, 2012, **197**, 57-64.

123 W. Sun and W. Liu, *J. Power Sources*, 2012, **217**, 114-119.

124 S.-Y. Park, C. W. Na, J. H. Ahn, U.-J. Yun, T.-H. Lim, R.-H. Song, D.-R. Shin and J.-H. Lee, *J. Power Sources*, 2012, **218**, 119-127.

125 G. Zhang, Z. Shen, M. Liu, C. Guo, P. Sun, Z. Yuan, B. Li, D. Ding and T. Chen, *J. Phys. Chem. B*, 2006, **110**, 25782-25790.

126 Z. Fan, C.-C. Chao, F. Hossein-Babaei and F. B. Prinz, *J..Mater. Chem.*, 2011, **21**, 10903-10906.

127 M. G. Bellino, D. G. Lamas and N. E. W. de Reca, *Adv. Funct. Mater.*, 2006, **16**, 107-113.

128 C. Labertyâ€Robert, J. W. Long, K. A. Pettigrew, R. M. Stroud and D. R. Rolison, *Adv. Mater.*, 2007, **19**, 1734-1739.

129 Q. Luo, D. R. Campbell and S. V. Babu, *Langmuir*, 1996, **12**, 3563-3566.

130 G. Adachi, N. Imanaka and Z. C. Kang, *Kluwer Academic Publishers*, 2004.

131 G. I. N. Waterhouse, J. B. Metson, H. Idriss and D. Sun-Waterhouse, *Chem. Mater.*, 2008, **20**, 1183-1190.

132 P. Jasinski, T. Suzuki and H. U. Anderson, *Sensor Actuat. B*, 2003, **95**, 73-77.

133 H. J. Beie and A. Gnarich, *Sensor Actuat. B*, 1991, **4**, 393-399.

134 L.-S. Zhong, J.S. Hu, A.-M. Cao, Q. Liu, W.-G. Song and L.-J. Wan, *Chem. Mater.*, 2007, **19**, 1648-1655.

135 M. Lira-Cantu and F. C. Krebs, *Sol. Energy. Mater. Sol. C*, 2006, **90**, 2076-2086.

136 Q. Wang, J. M. Perez and T. J. Webster, *Int. J. Nanomed.*, 2013, **8**, 3395.

137 R. W. Tarnuzzer, J. Colon, S. Patil and S. Seal, *Nano Lett.*, 2005, **5**, 2573-2577.

138 J. P. Chen, S. Patil, S. Seal and J. F. McGinnis, *Nature Nanotechnol.*, 2006, **1**, 142-150.

139 B. A. Rzigalinski, K. Meehan, R. M. Davis, Y. Xu, W. C. Miles and C. A. Cohen, *Nanomedicine*, 2006.

140 N. Singh, C. A. Cohen and B. A. Rzigalinski, *Ann. NY Acad. Sci.*, 2007, **1122**, 219-230.

141 S. M. Hirst, A. S. Karakoti, R. D. Tyler, N. Sriranganathan, S. Seal and C. M. Reilly, *Small*, 2009, **5**, 2848-2856.

142 S. Babu, J. H. Cho, J. M. Dowding, E. Heckert, C. Komanski, S. Das, J. Colon, C. H. Baker, M. Bass, W. T. Self and S. Seal, *Chem.Commun.*, 2010, **46**, 6915-6917.

143 I. Celardo, J. Z. Pedersen, E. Traversa and L. Ghibelli, *Nanoscale*, 2011, **3**, 1411-1420.

144 S. Chakraborthy and A. Sen, *Sensor Lett.*, 2009, **7**, 91-96.

145 M. Hosseini, M. R. K. Pur, P. Norouzi, M. R. Moghaddam, F. Faridbod, M. R. Ganjali and J. Shamsi, *Anal. Method*, 2015, **7**, 1936-1942.

146 M. B. Gumpu, N. Nesakumar, S. Sethuraman, U. M. Krishnan and J. B. B. Rayappan, *Sensor Actuat. B*, 2014, **199**, 330-338.

147 M. Singh, N. Nesakumar, S. Sethuraman, U. M. Krishnan and J. B. B. Rayappan, *J. Colloid Interf. Sci.*, 2014, **425**, 52-58.

148 D. Zhang, W. Wu, X. Ni, X. Cao, X. Zhang, X. Xu, S. Li, G. Han, A. Ying and Z. Tong, *J. Mater. Sci.*, 2009, **44**, 3344-3348.

149 L. Almar, A. Tarancon, T. Andreu, M. Torrell, Y. Hu, G. Dezanneau and A. Morata, *Sensor Actuat. B*, 2015, **216**, 41-48.

150 M. Das, S. Patil, N. Bhargava, J. F. Kang, L. M. Riedel, S. Seal and J. J. Hickman, *Biomaterials*, 2007, **28**, 1918-1925.

151 M. Y. M. Abdelrahim, S. R. Benjamin, L. M. Cubillana-Aguilera, I. Naranjo-RodrÃguez, J. L. de Cisneros, J. J. Delgado and J. M. Palacios-Santander, *Sensors*, 2013, **13**, 4979-5007.

152 E. Sharpe, T. Frasco, D. Andreescu and S. Andreescu, *Analyst*, 2013, **138**, 249-262.

Definition of the present problem

Cerium dioxide is one of the most imperative rare earth oxides which have been utilized for decades on account of its multifunctional applications based on the inherent and superior physiochemical features. With the onset of the revolutionary impacts of nanotechnology, nano ceria below has replaced its bulk counterpart in most of its renowned applications, which circuitously improved the performance of ceria based devices. Even though nanotechnology has indisputably bestowed beneficial features to this oxide system, the complete facets of the effect of size reduction on its properties are yet to be explored satisfactorily. As pointed out earlier, it is well established on the basis of literature that semiconductor nanocrystal exhibits novel size dependent properties during the nanoscaling process, which are proficient in pertaining them for numerous versatile application. Ceria based research is poorly developed on that regard, even though there are certain reports mentioning the size related photoluminescence of this material. Surprisingly, ceria has been well exploited as a luminescence material by doping with other rare earth ions which are highly expensive. Under such situation, a proper understanding of the size related properties can certainly improve the performance and broaden the techno-commercial significance of this oxide. Based on this observation, this thesis envisages the unexplored aspects of nanoceria which could enhance the utilization of this commercially valuable oxide for promising applications.

Briefly, the work under taken in this thesis can be divided as follows.

1. Synthesis of ceria nanoparticles with size as small as possible, preferably below 3 nm by adopting simple synthetic strategies.

2. Investigation on the effect of size on the properties of ceria by carrying out detailed spectroscopic investigation in comparison with the bulk as well as nano sized particles.

3. Preparation of stable aqueous and non- aqueous dispersions based on the synthesised nanoparticles so that they can interact effectively with other components of nano devices which are aimed for practical applications.

4. Tailoring the novel optical properties of ceria derived from its nanodimension for functional applications including a FRET probe for the identification of fatty acids and an efficient sensor for vitamin C.

The thesis has been designed on the above objectives. The results obtained are discussed which have been correlated to the experimental parameters and properties.

CHAPTER 2

Dimension tuned cerium oxide nanoparticles engineered via surface modification and investigation of their size induced properties

2.1 Abstract

The size controlled synthesis of ceria nanoparticles has been accomplished by adopting different aqueous and non-aqueous strategies so as to fabricate particles with ultra fine dimension, which could be transformed into stable dispersions. The protocol was based on the principle of steric stabilisation rendered by surfactants on the nanoparticle surfaces during nucleation. Long chain fatty acids and polymers were experimented as surfactants and was assessed that parameters like characteristics of surfactant and their molar ratio to the precursor was crucial in controlling size as well as surface passivation of the nucleated nanoparticles.

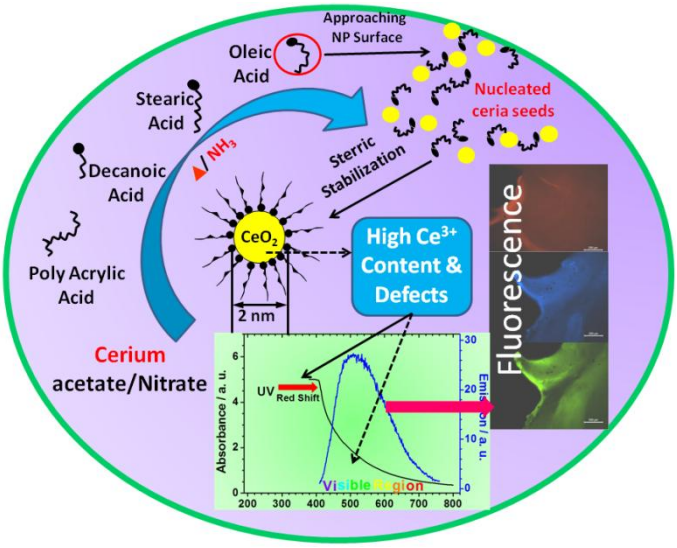

Out of these adopted synthetic methods, ceria nanodots of size as fine as 2 nm could be obtained by the thermolysis of cerium acetate in diphenyl ether in the presence of oleic acid as surfactant. At a glance, among the surfactants employed for steric stabilisation, oleic acid rendered effective surface modification and size control to the nanoparticles and a mechanism based on its kinked structure was proposed to explain

its efficiency. The surfactant coating enabled them to be easily dispersible in nonpolar solvents which were stable over months. Detailed spectroscopic investigations have been carried out to understand the effect of reduction in size on the properties of the particles. It could be inferred that the nanodots exhibited novel size dependant optical properties such as red shift in the absorption and the band gap. As a result of its ultra fine size, oleic acid coated nanodots emit photons in the visible region with broad photoluminescence spectra resulting in multi-coloured fluorescence corresponding to blue, green and red. A mechanism is proposed based on the higher concentration of Ce^{3+} and the associated defects originated in the nanocrystals while it approaches molecular dimensions which were justified by the XPS and Raman analyses. In short, it could be summarised that ceria nanoparticles exhibit many interesting optical properties owing to the miniaturisation of crystal size which show promise for adaptation to useful optical applications.

2.2 Introduction

The fascination with nanotechnology emerges from the unique physiochemical properties bestowed by them to the materials owing to the reduction in size.[1] The technology has acquired enormous attention in the recent era on account of the enhancement in their bulk properties imparted by their nano-dimensions. It has also succeeded in moulding these distinct properties into commercial applications involving the fabrication of many versatile devices. Thus, the advances in nanotechnology have boosted the efficiency of many functionally significant materials like cerium dioxide, which belongs to the class of semiconductors. Semiconductor nanocrystals, usually called 'quantum dots (QD)' are fluorescent, on account of the quantum confinement effects and they possess properties like narrow emission, colour tuning etc. Consequently, they have great scientific and technological potentials in fields like bioimaging,[2] solar cells,[3] colour display units[4] etc. Such materials are also being used as an alternative for the conventional organic chromophores which are prone to photo bleaching.[5] However, most of the quantum dots are based on the elements ca. Cd, In and As, which possess intrinsic limitations such as chemical instability and toxicity. In fact, they are carcinogenic and hazardous for the environment.[6] On this background, rare-earth oxide based fluorescent nanoparticles grasped special attentions due to their negligible toxicity and long term stability on exposure to heat or light. Among these oxides, ceria triggered more interest and charm on the grounds of its higher biocompatibility and ease of surface functionalisation.[7]

Nanoceria is an extensively studied system implemented for a variety of applications in solid oxide fuel cells,[8] cosmetics,[9] chemical mechanical polishing,[10] catalysis,[11] gas sensing,[12] oxygen permeation membrane systems[13]

etc. Though the luminescence of ceria has already been revealed to the scientific community, it is the most unexplored property of this oxide material. In fact, the optical properties of ceria are under the shadow of its other prominent properties like redox nature, oxygen storage capacity, ionic conductivity etc. A single look at the research articles published on ceria readily admits this fact because majority of them involves catalysis. But the recent advances of this material in biomedical applications motivates researchers to improve its luminescent properties as it can add merit to its bioactivity by facilitating the easy tracing of these nanoparticles in their biological pathway.

Though ceria absorbs in the UV region, it can be tailored into a luminescent material by adding dopants to its crystal structure. This is achieved by the energy transfer from the O^{2-} state of ceria to that of the dopant energy level. Fujihara *et al.* fabricated ceria thin films in which Eu^{3+} and Sm^{3+} was incorporated as activators.[14] Both the dopants induced a reddish orange coloured emission in ceria, owing to the intra configurational *f-f* transitions. Besides, there are also numerous studies on the onset of photoluminescence in ceria upon doping with rare earth ions like Eu^{3+}, Sm^{3+}, Tb^{3+}, Dy^{3+}. The major oddity of this adopted method is that whereas ceria is one of the cheap rare earth oxides which could be fabricated inexpensively, the precursors of all the dopants are very expensive. Although the dopant concentration is very less, even its less quantity costs almost same as that of the bulk amount of the parent matrix which subsequently doubles the total expenditure.

The studies by Morshed *et al.* in 1997, presenting a blue emission from ceria thin films deposited on a Silica substrate by pulsed laser ablation, opened up new possibilities of inducing luminescence in bare ceria.[15] Later there have also been certain other reports on green coloured emission of ceria owing to the reduction in

size. More recently in 2007, Maenisiri *et al.* observed a blue-green emission for platelet like ceria nanoparticles with size ~6 nm.[16] However, there is a lack of detailed scientific investigation of this size related property of ceria which could trigger the techno-commercial value of this material. The present chapter aims at analysing the size induced properties of ceria and unveiling the mystery associated with its nanodimension.

In the view of size controlled synthesis of ceria, a large number of techniques have been reported to synthesise nanosized ceria with good control of its dimension and properties. As mentioned in the first chapter, the smallest ceria crystals reported thus far is 1.8 nm by Yu *et al. via* a hydrothermal method in the presence of a double hydrophilic block co-polymer.[17] In other reports, Inoue *et al.* adopted a solvothermal method to synthesise colloidal dispersion of 2 nm ceria nanoparticles.[18] The synthesis of 2.2 nm lipophilic ceria nanoparticles has been reported by Taniguchi *et al.*[19] and Ahinyaz *et al.*[20] produced ceria nano rods with diameter 2 nm; both involving oleic acid as surfactant. Numerous methods such as hydrothermal,[21] alcothermal,[18] thermal decomposition,[22] reverse micellar[23] and aqueous precipitation[24] have previously been adopted for the synthesis of ceria nanoparticles with smaller size. Among these, hydrothermal and alcothermal methods demand high pressure and/or temperature equipment which invites additional costs and processing time. Herein, we have adopted simple, time- saving and inexpensive synthetic strategies based on aqueous precipitation as well as thermal decomposition which aims at producing well stabilised ceria nanoparticles with size as fine as possible.

A surfactant assisted steric stabilisation process was also incorporated in the synthetic strategy, in order to control the size of the crystals. Surfactants, as explained in the first chapter, are bulkier groups used as capping agents for the particles. They

selectively bind to the different crystallographic facets of the nucleated particles, which prevents the further crystal growth on account of the steric hindrance provided by them over the particle surface.[25] Thus the nucleated particles will be of fine size and depending on the nature of the surfactants; the particles will be dispersible in suitable solvents. The most commonly adopted surfactant molecule for colloidal syntheses include alkyl- thiols, long chain amines, carboxylic and phosphonic acids, phosphine oxides, phosphine, phosphates, phosphonates etc.[26] In the present study, the choice of the surfactants is on account of the common solubility of the surfactant and the nanoparticle precursor in the reaction media.

In short, the present chapter emphasises on the size controlled synthesis of cerium oxide to obtain particles with size as fine as possible. The synthetic conditions and parameters have been optimised for acquiring well stabilised and monodisperse nanoparticles. The success in the protocol has been assessed by spectroscopic analysis involving XRD, PCS and TEM. The change in properties of the nanoparticles with the achievement of molecular dimension has been explored *via* UV and PL spectroscopy and the study of chemistry behind their behaviour has also been carried out.

2.3 Experimental Section

All the chemicals were used as received without further purification. Cerium nitrate hexahydrate (99.9%) was procured from Indian Rare Earths, India, cerium acetate (99.9%) and stearic acid (90%) were purchased from Merck, India, decanoic acid (90%), poly acrylic acid (45 Wt. % solution, Mol. Wt. 1200), diphenyl ether (99%) and oleyl amine (70%) from Sigma Aldrich, ammonium hydroxide (25%, analytical grade) was brought from Qualigens Fine Chemicals, India, oleic acid (90%), from

Alfa Aesar, UK. Common solvents of analytical grade such as ethyl alcohol, acetone, cyclohexane and toluene were procured from Merck, India.

Different fatty acid based surfactants as well as a polymer; polyacrylic acid (PAA) was employed as surfactants. For fatty acids, as they are miscible in only organic solvents, a non-aqueous thermal decomposition strategy has been adopted. Long chain fatty acids, specifically stearic acid (SA, $C_{18}H_{36}O_2$), oleic acid (OA, $C_{18}H_{34}O_2$) and decanoic acid (DA, $C_{10}H_{20}O_2$) have been used and the samples are named as SANP, OANP and DANP corresponding to the surfactants mentioned respectively. As PAA is hydrophilic; a synthetic strategy based on precipitation in aqueous media has been adopted. The sample prepared so has been named as PANP. The precursor-to-surfactant molar ratio were varied in a set of experiments to optimise the reaction conditions for obtaining the finest particles with efficient surface capping which can yield stable dispersions. The ratio was varied from 1:1 to 1:5 and the minimum amount of surfactant required for efficient capping has been optimised. For getting the fine sized nuclei, a lower precursor concentration of 0.05 M in the solvent was employed. Also as a control, particles has been synthesised without any surface modification by thermal decomposition in the absence of surfactants, which is labelled as UCNP. Bulk ceria has also been produced by calcining cerium nitrate at 1000°C.

2.3.1 Synthesis of ceria nanoparticles by non-aqueous thermal decomposition route

The precursor employed in the present synthetic strategy was cerium acetate which could be easily decomposed upon the supply of heat. In a typical synthesis, cerium acetate (0.005 moles) was dissolved in diphenyl ether (100 ml) in a round-bottom flask. To this, appropriate amounts of surfactants (added volume of surfactant is

depending on the employed precursor-to-surfactant ratio, which was varied from 1:1 to 1:5) and co-surfactant (the surfactant to co-surfactant ratio was 1:1.5) were added and the reaction mixture was refluxed (at ~265 °C) for 1 h. As the reaction proceeded, the solution turned brown, indicating the formation of ceria nanocrystals. After the reaction time, the mixture was allowed to cool to room temperature. Subsequently, acetone was added to the reaction mixture to precipitate the surfactant-coated nanoparticles. The precipitate obtained was separated by centrifugation and washed thoroughly with acetone several times to get rid of excess surfactants. Finally, after washing, the precipitate was dried in an air oven to get slightly brownish powder.

2.3.2 Synthesis of ceria nanoparticle by aqueous precipitation method

The precursor used was cerium nitrate which could be precipitated to hydroxide and finally to oxide upon addition of a base. Typically, to 100 ml of an aqueous solution of cerium nitrate (0.05M), adequate amount of PAA (volume being varied from 0.5 to 2 ml depending on the precursor-to-surfactant ratio, which was same as the above method) was added under strong mechanical agitation using a 1/8 hp overhead stirrer. After 10 minutes, as the solution becomes a uniform mixture of the precursor and polymer, adequate amount of ammonium hydroxide solution was added (volume varied from 10 ml to 20 ml depending on the volume of added PAA). The fresh suspension turned blackish purple immediately after the ammonia addition and finally to slight yellow after about 1 h stirring. Subsequently, the particles were precipitated by the addition of acetone which was isolated from the reaction media by centrifugation. The precipitate was washed several times with ethyl alcohol followed by acetone which was finally dried to get the ceria particles.

The volume of ammonium hydroxide solution added was based on the theoretical calculation of the amount of hydroxyl group needed to precipitate cerium hydroxide

as well as to deprotonate the carboxylic group in the polymer surfactant. Slight excess of the theoretical amount of required base has been taken.

2.4 Results and discussions

2.4.1 Mechanism of nanoparticle formation

2.4.1.1 Thermolysis of cerium acetate

The thermal decomposition of a metal precursor in a high boiling organic solvent in presence of a suitable surfactant is an efficient one pot method for the synthesis of monodisperse nanoparticles. The non-hydrolytic approach of this procedure has several advantages over other routes like better crystallinity and monodispersity of the nucleated particles.[27] In this method, all the components of the reaction mixture are heated simultaneously and therefore nucleation of all the particles occurs simultaneously. As these particles emerge virtually at the same time, their growth histories will also be identical and thus they will be almost of same size.[28] Also this method permits the facile separation of nucleation stage from that of growth, which results in the narrow size distribution of particles according to the 'separation of nucleation and growth mechanism.[29] In the presence of surfactants, the crystal growth can be yet again prevented by the surface modification immediately after nucleation which ensures better size reduction of the particles.

During the process, upon acquiring the heat generated by the solvent, the precursor decomposes in the oxygen atmosphere to its corresponding oxide. The right choice of the precursor, especially the match between its thermal stability and the boiling point of the solvent, is a key factor determining the success of the scheme.[26] Considering the boiling point of diphenyl ether solvent, which is ~265°C, the thermogravimetric analysis of cerium acetate as shown in Fig. 2.1 substantiates its

candidature as a precursor for the suggested experimental design. Cerium acetate starts decomposing at ~150°C which ends within 260°C as implied by TGA.

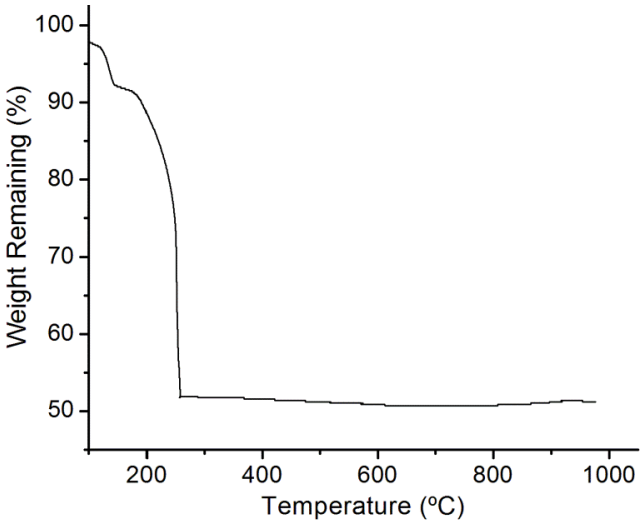

Fig. 2.1 Thermogravimetric profile of cerium acetate.

According to earlier reports, thermally activated decomposition of the acetate precursor in organic media proceeds *via* free radical intermediates which can undergo various reactions such as recombination, decay into smaller fragments, or propagation and as a consequence, a Ce–O–Ce bond is formed as shown below[28,30]

$$Ce–OOCR \rightarrow Ce^{\bullet} + R– COO^{\bullet} \quad (1)$$

$$Ce–OOCR \rightarrow CeO^{\bullet} + R – CO^{\bullet} \quad (2)$$

$$Ce^{\bullet} + MO^{\bullet} \rightarrow Ce– O– Ce \quad (3)$$

In the mean time, the fatty acids in the presence of oleylamine undergo dissociation in the reaction media and the formed negatively charged carboxylate ions chemisorb onto the positively charged nanoparticle surface.[31,32] It is known that long chain fatty acids are excellent contenders for the stabilisation of nanoparticles due to the steric effect rendered by their alkyl chain.[33] They prevent the crystal growth as well as aggregation of the particles thus imparting their fine dimension.

2.4.1.2 Precipitation of cerium nitrate

Precipitation of ceria from the nitrate salts is associated with several reaction steps involving intermediates. During the addition of the base to the reaction media, $Ce(OH)_3$ is generated from the nitrate and as the hydroxide has an extremely low solubility constant ($K_{sp} = 6.3 \times 10^{-24}$ at 25ºC) it will be easily precipitated out of the solution.[34] Later, the precipitate is oxidised to its +4 oxidation state as $Ce(OH)_4$, which finally, gets dehydrated to $CeO_2.nH_2O$.[35] The overall chemical change involving the precipitation process is expressed as below[36,37]

$$2CeNO_3 + ½\ O_2 + 6OH^- \rightarrow 2\ CeO_2.\ nH_2O + 6NO_3^- + (3\text{-}2n)\ H_2O \qquad (4)$$

Meanwhile, the PAA which has been dissociated in the prevailed pH gets chemisorbs on to the particle surface by the $–COO^-$ bond as a capping agent which prevents further crystal growth and stabilise them. Here, the attachment is such that while one of the carboxylate groups in the individual acrylic acid molecule is attaching to the particle surface, the other one will protrude out of the surface.[38]

The manner in which surfactants gets linked over the nanoparticle has been depicted in Scheme 2.1. Due to the projection of the non-polar alkyl chain over the surface, the fatty acid stabilised nano particles are expected to be hydrophobic. Therefore, they are assumed to be dispersible in non-polar solvents. In the case of PAA, due to the second carboxylate group over the surface which is freely available, PANP surface are expected to be polar in nature. This conveys an impression that they will be compatible in aqueous media. It could be observed that a lower concentration of surfactants failed to disperse the formed particles in the respective solvent. The dispersity of all the samples synthesised with various precursor-to-surfactant ratio was examined which implied that the ratio between the Ce containing

moiety to a single –COOH group in the surfactant should be at least 1:4 to acquire efficient surface coating. Therefore, the experimental conditions have been optimised and all the samples discussed in later part of this chapter are those synthesised at a precursor-to-surfactant ratio of 1:4.

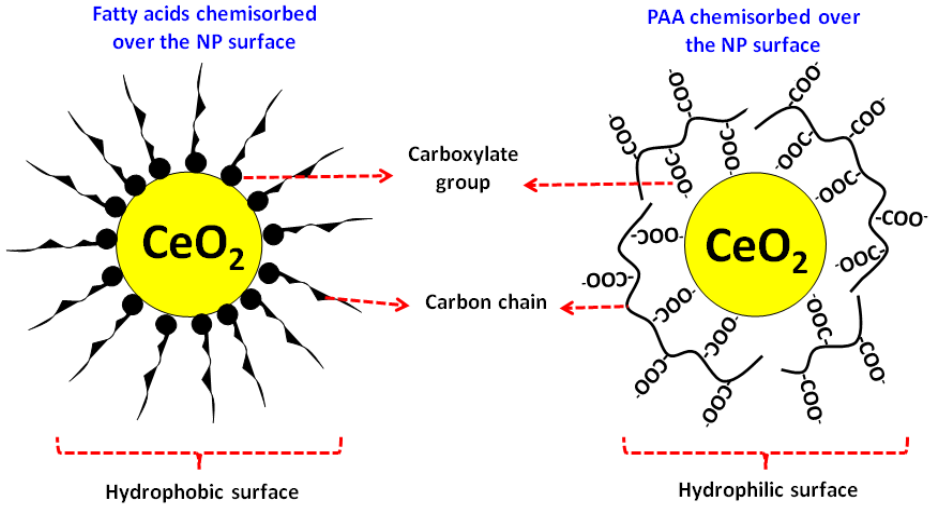

Scheme 2.1 Conceptual representation of the mode of attachment of the surfactants over the nanoparticle surface.

The efficiency of the surfactants in steric stabilisation and the extent of success in the controlling the size of the nucleated particles have been explained in detail in the later parts of this chapter.

2.4.2 Preliminary characterisations of the nanoparticles

The powder X-ray diffraction (XRD) patterns of the synthesised nanoparticles are illustrated in Fig. 2.2. The detectable peaks of all the samples can be readily indexed to the pure face-centred cubic fluorite phase of ceria with the space group, $Fm\bar{3}m$ (according to JCPDS card No. 34-0394).[39] The characteristic peaks at ~ 28.3º, 47º, 56.3º and 76.7º with corresponding *d*-values 3.12, 1.91, 1.632 and 1.24 nm could be assigned to the diffractions from (111), (220), (311) and (331) planes of ceria respectively.[40] Thus, the XRD analysis circuitously indicates that pure and

crystalline ceria nanoparticles could be fabricated by means of both the adopted synthetic strategies. It is noticed that the width of the peaks are obviously broadened for all the samples, which is a typical feature of nanostructured materials.[41]

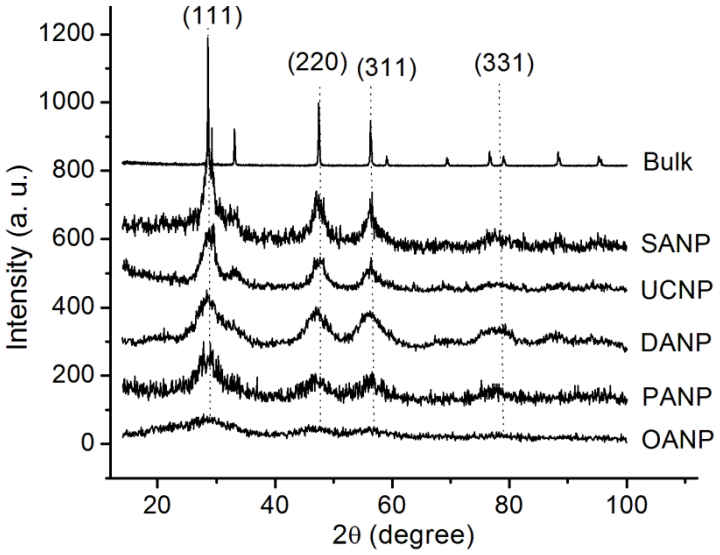

Fig. 2.2 X-ray diffractograms of ceria nanoparticles synthesised by aqueous and non-aqueous routes.

The nanocrystalline nature of the particles was further investigated by deriving their crystal dimensions (D_{XRD}) from the XRD broadening using the Debye–Scherrer formula which gives 0.7, 1.2, 2.1, 2.4 and 3.2 nm for OANP, PANP, DANP, UCNP and SANP respectively. It was observed that though the adopted synthetic procedure was successful in producing ceria nanoparticles of size in the nano range, the crystallite size of nucleated particles varied with the surfactant employed. Also the authenticity of the ultra low crystal size of OANP which is below 1 nm insists the careful analysis of other data before a conclusive statement on the particle size being arrived.

In order to unveil the nature of interaction between the surfactants and the particle surface, FT-IR analysis of OANP, SANP, PANP and DANP has been carried out and the results are presented in Fig. 2.3. The bands observed at 1350 cm^{-1} corresponds to

the $\nu_{(CeOCe)}$ vibrations and that at 475 cm^{-1} arised from the –Ce–O stretching.[42] This confirms the formation of ceria by the surfactant assisted synthetic methods adopted in the present chapter. The peaks at 2845 and 2927 cm^{-1} are due the characteristic –C–H vibrations of groups present in the surfactants[43] and that at 715 cm^{-1} are due to the rocking vibrations of $(CH_2)_n$ chains with n > 3.[44] The bands at 1433 and 1515 cm^{-1} are attributed to the carbonyl bonds of the carboxylate ions present in the surfactants[21,44] and require special attention because they provide vital information regarding the linkage of the surfactant with the nanoparticle. According to previous literatures, the presence of these two bonds with a separation of ~100 cm^{-1} conveys that the COO^- group has been covalently bonded

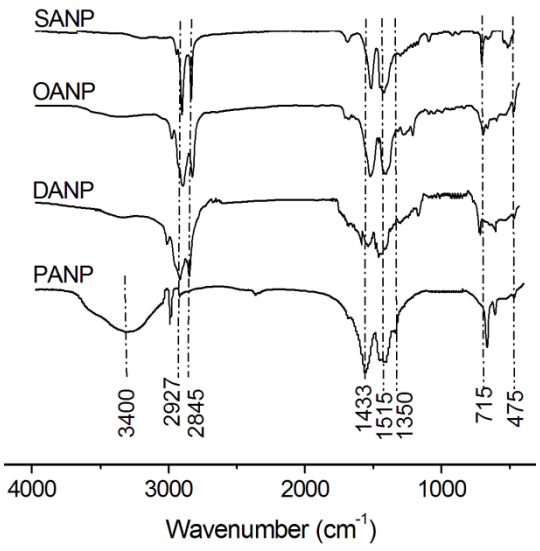

Fig. 2.3 FT-IR spectra of the nanoparticles with surface modification using different surfactants.

to the Ce atoms of ceria in a bidentate fashion.[45] Thus, on the basis of FT-IR analysis and information from available literature, it is assumed that the surface modification of the particles has been brought about by the chemisorption of the carboxylate ions of the surfactants over the nanoparticle surface. The broad peak of PANP appearing

around 3440 cm^{-1} is due to the –OH stretching frequency probably from the moisture absorbed over the particles which is coated with a hydrophilic group like PAA.[46]

2.4.3 Size analysis of the nanoparticles

Bright-field transmission electron microscopy was employed to explore the physical size and morphology of the nanoparticles under investigation. Fig. 2.4, 2.5 and 2.6 supplies the TEM images of all the samples under consideration.

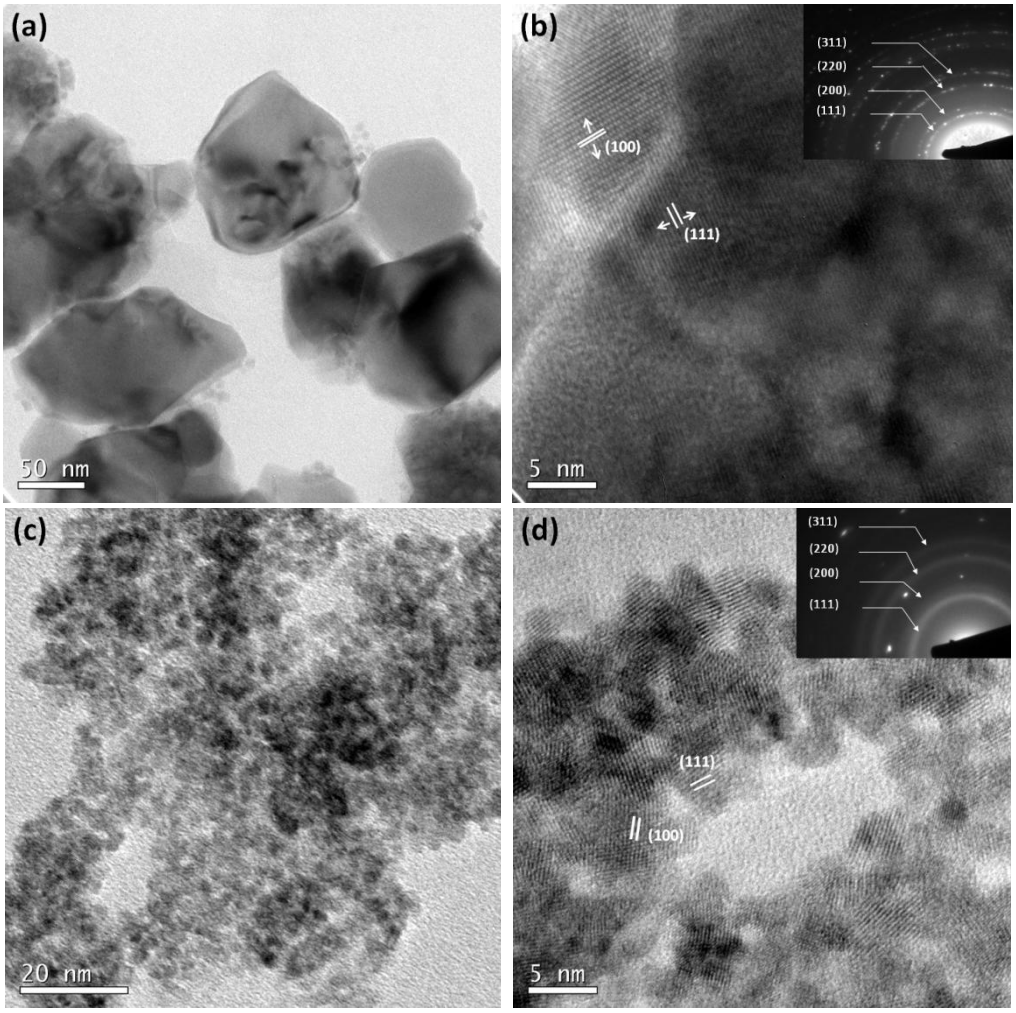

Fig. 2.4 High resolution and low magnification TEM images of (a), (b) Bulk ceria and (c), (d) UCNP respectively; the SAED patterns are being provided as inset.

The images showed exposed and predominant (111) and (100) lattice fringes of ceria with the corresponding interplanar spacings of 0.31 and 0.27 nm. The SAED and

FFT patterns of the corresponding reflections have also been provided with the images. It was obvious from the TEM analysis that spherical ceria nanocrystals of size typically below 10 nm have been formed by the adopted synthetic procedure involving different surfactants. An exception is for bulk which consisted of large crystals in the order of ~100 nm as indicated in Fig. 2.4(a). The images of UCNP as shown Fig. 2.4(c) and (d) show that smaller crystals of size in the range 4–6.5 nm could be synthesised even without surface modification. The calculated average size (D_{TEM}) on 100 particles of UCNP was ~4.3 ± 1.2 nm. It is supposed that even in the absence of a capping agent, the reduction in size might has been brought about by the lower precursor concentration employed during the synthesis which allowed the nucleation of smaller particles. But it could be noted that due to the high surface energy and absence of any surface modification, the particles were highly agglomerated. Another noteworthy piece of information is that the large crystals present in the bulk remained as individual particles without any agglomeration; the possible reason may be its lower surface energy compared to that of the nanosized particle.

The TEM images of surface modified samples as shown in Fig. 2.5 and 2.6 convey that the size of the formed particles as well as their surface stabilisation markedly varies in accordance with the surfactant employed. From Fig. 2.5 (a) and (b), it could be assessed that PANP was poorly stabilised and the formed particles were highly agglomerated. But the high-resolution image shows that yet the size of the particles was very low with a D_{TEM} of 2.3 ± 0.2 nm. This indicates that PAA attached on the surface could successfully control the crystal growth but the stabilisation rendered by them over the surface was not very effective which eventually led to agglomeration. The surface stability provided by the surfactant, DA

to the nanoparticles was even better than that of PAA as shown in panels (c) and (d). But the size of the particles was higher than that of PANP with a D_{TEM} of 4 ± 0.5 nm. Compared to other surfactants discussed later, the surface passivation by DA was not very efficient and as a result particle could not be visually well separated in the TEM images as SANP and OANP whose TEM images is also provided.

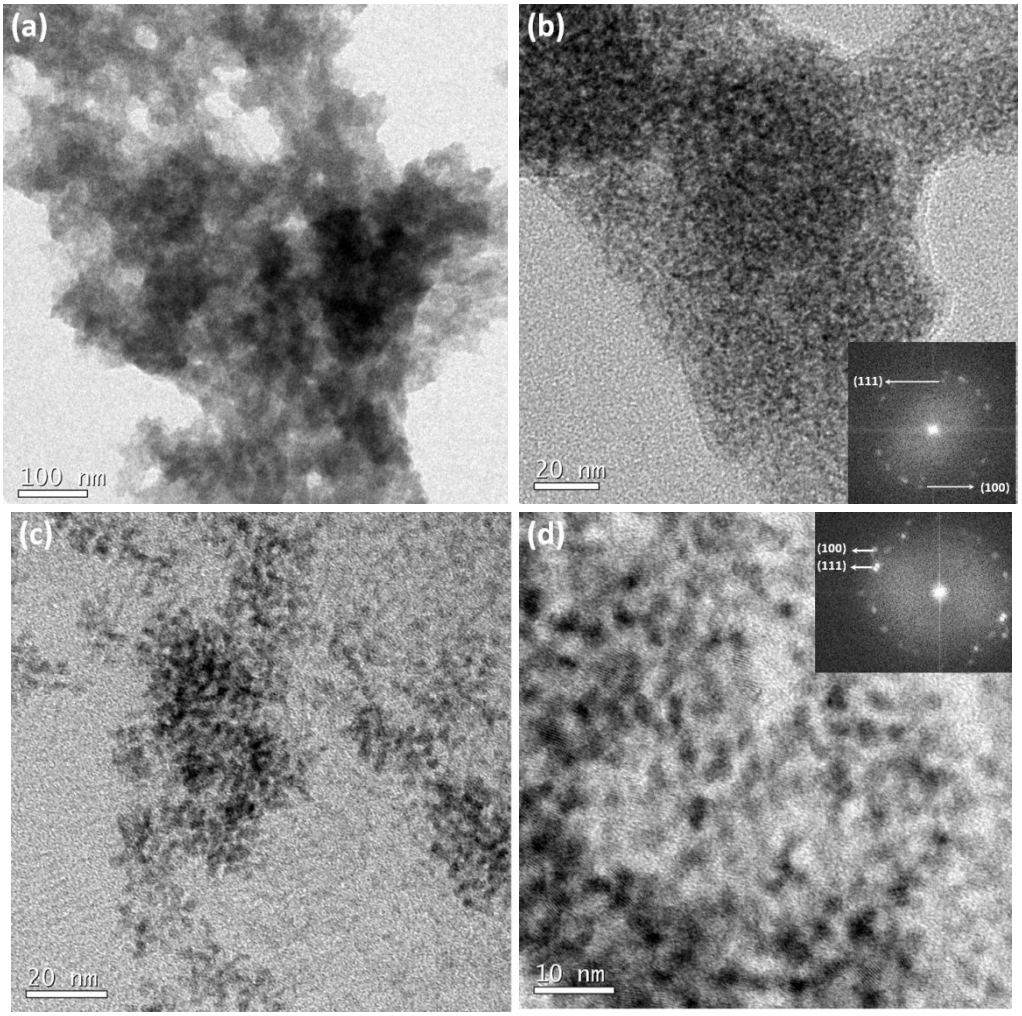

Fig. 2.5 TEM images along with the FFT patterns of the surface modified nanoparticles (a), (b) PANP and (c), (d) DANP.

The TEM images of SANP and OANP in Fig. 2.6 presents well separated spherical particles without evidence of the presence of agglomerates. The visualisation of particles as individual monodisperse grain indicates the effective surface functionalisation by OA and SA on the particles. But an observed distinction

between the interaction of the two surfactants with the nanoparticles is that OA facilitated the formation smaller crystals, and that produced by SA was larger ones. The D_{TEM} of OANP and SANP was ~2 ± 0.2 nm and 5.02 ± 0.4 nm respectively. Though both the samples were synthesised through the same experimental pathways, the difference of ~3 nm between the size of SANP and OANP undeniably implies the role of the surfactants in controlling the crystal growth. After the detailed structural investigation of the surfactants, the factor which differentiates both the surfactants during the course of crystal growth has been considered and a mechanism based on this has been included in the later part of this chapter.

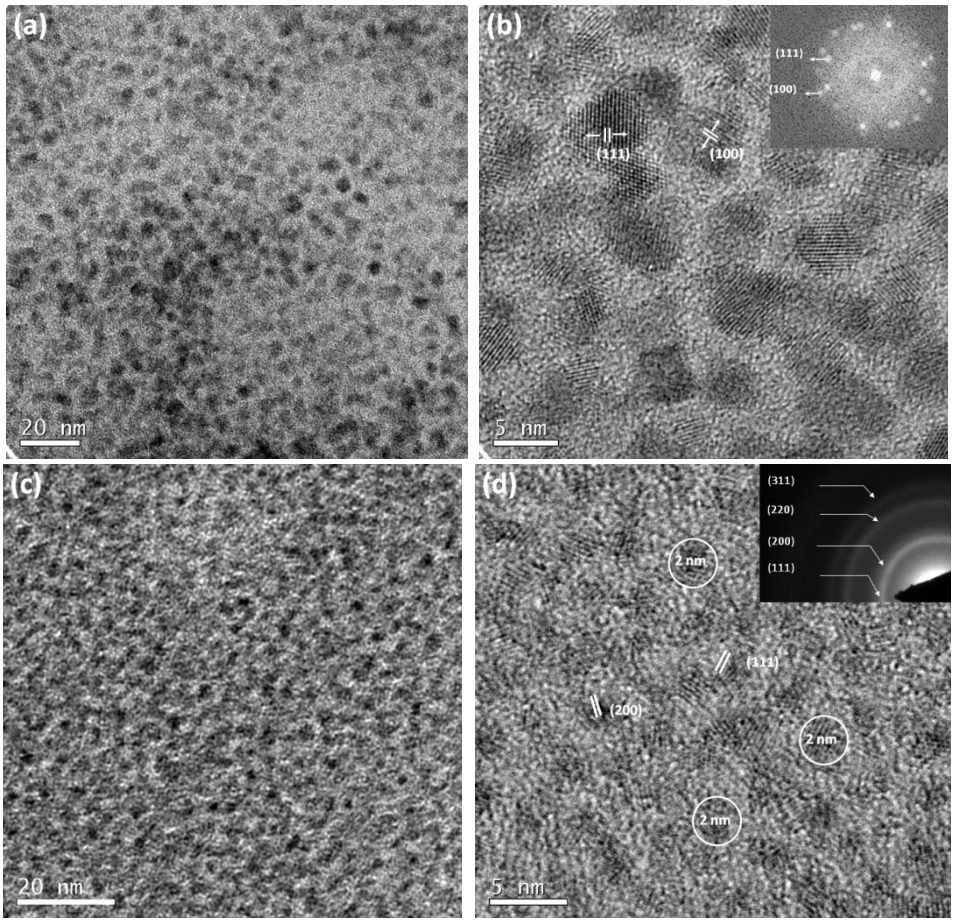

Fig. 2.6 TEM images of (a), (b) SANP and (c), (d) OANP showing spherical and well separated ceria nanoparticles.

In brief, it could be assessed that the process of surface passivation has crucial role in controlling the crystal growth of the particles after its nucleation and

depending upon the surfactant, particle with a range of D_{TEM} values was obtained under the considered experimental conditions. It was also observed that while PAA and DA failed to stabilise the nanoparticle surface, OA and SA was found to be excellent candidates for the same.

The behaviour and size of the synthesised nanoparticles in their dispersion has been analysed using photon correlation spectroscopy (PCS). OANP and SANP exhibited a mono modal size distribution with narrow peaks. This reveals the monodisperse nature of the particles and the hydrodynamic size (D_{PCS}) observed for SANP and DANP are 13.1 and 4.2 nm respectively. The observed value was higher than that obtained from TEM. As TEM is more sensitive to the heavier elements (cerium), the D_{TEM} gives only the size of the ceria core.[24] Whereas, PCS measures the hydrodynamic diameter, the diameter of the hydrated sphere scattering photons

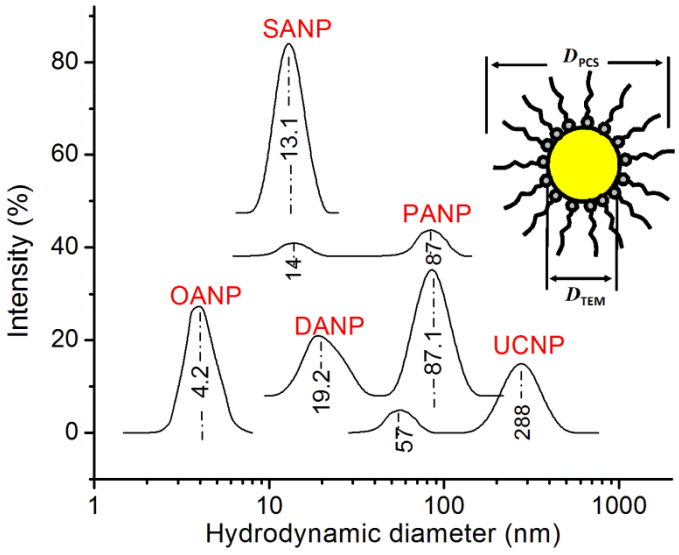

Fig. 2.7 PCS spectra of the samples conveying their particle size distribution in the respective dispersions.

(undergoing translational diffusion), which includes the core along with the surfactants. Therefore D_{PCS} includes the length of the surfactant chain protruding out of the particle surface along with the core size. The effective chain length of OA is

close to the 0.9 nm.[47] Therefore the D_{PCS} for OANP can be calculated by considering the chain length of surfactant on both sides of the particle along with the core size (D_{TEM}) which came out to be ~4 nm {(0.9 nm × 2) + 2}. For SA, the chain length is 2.4 nm and the theoretical hydrodynamic diameter is deducted to be ~10 nm. It could be concluded from Fig. 2.7 that the experimental D_{PCS} matches well with that of the theoretical value for both OANP and SANP. This implies that the scattering of photons was brought about by individual grains, indicating the non-existence of particle clustering in solvent. Thus, PCS data revealed that both SA and OA could effectively protect the surface of the particles from agglomeration and stabilise them in their dispersions.

For the other samples, a bi-modal distribution of size was observed. The behaviour of UCNP is obviously due to the lack of any surface modification which might have triggered the nanosized particles to agglomerate in the solvent under the influence of their high surface energy. This might have eventually led to the formation of big as well as small clusters, ending up with the appearance of more than one peak in the photon correlation spectra. The inability of the other two surfactants, DA and PAA to effectively stabilise the particles may be the reason behind the formation of agglomerates in the corresponding dispersions as indicated by the PCS data.

Table 2.1 Comparison of size of nanoparticles deducted using different measurement methods

Sample	D_{XRD} (nm)	D_{TEM} (nm)	D_{PCS} (nm)
SANP	3.2	5	13
UCNP	2.4	4.2	57 & 288
DANP	2.1	4	19 & 87
PANP	1.2	2.2	14 & 82
OANP	0.7	2	4.6

The size calculated from the PCS and TEM data and its comparison with the crystallite size estimated from the XRD broadening has been summarised in Table 2.1. Although the order of size as visualised in the TEM is in the same order as that of their crystallite sizes, the D_{TEM} values are slightly higher. This is because D_{XRD} implies the size of single crystals whereas D_{TEM} evaluates the size of the particle which might be a combination of crystallites.[48] While the D_{PCS} is in good agreement with that of D_{TEM} in the case of OANP and SANP, more than one peak were obtained for other suspensions due to the inefficient surface stabilisation.

2.4.4 Stability studies of the nanoparticles in their dispersion

For studying the stability of dispersions based on the synthesised nanoparticles, 0.1% nanoparticle (by wt.%, excluding the surfactant weight) dispersion has been prepared. For PANP, the dispersion was aqueous based and for the rest, toluene was used as the dispersion media. The optical images of the same are demonstrated in Fig. 2.8.

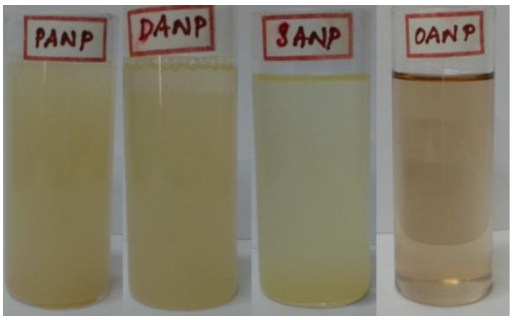

Fig. 2.8 Optical photographs showing the dispersions of surfactant coated nanoparticles.

It could be observed that OANP produced the most transparent dispersion which was stable over months. SANP also produced stable dispersion which was slightly more turbid than OANP probably due to the scattering of light owing to its higher hydrodynamic diameter compared to OANP. Suspensions produced from PANP and DANP were fairly turbid and exhibited a tendency to settle after few hours of

preparation and underwent complete sedimentation within two days. This may be because of the presence of large aggregates in the suspension owing to their active surfaces, eventually settled under the influence of gravity.

Table 2.2 Turbidity of the surfactant coated nanoparticles in dispersion measured for a period of one week

	Turbidity (NTU)						
Sample	**Day 1**	**Day 2**	**Day 3**	**Day 4**	**Day 5**	**Day 6**	**Day 7**
OANP	2	2	2	2	2	2	2
SANP	28	27	23	19	19	21	20
DANP	206	153	87	21	1	1	1
PANP	247	134	17	1	1	1	1
Toluene	1						
Water	0.5						

In order to study the stability of the dispersions more scientifically, the turbidity measurements has been carried out and the results are given in Table 2.2. OANP displayed very low turbidity values, almost close to that of the solvent indicating their ultra fine size and complete absence of agglomeration in dispersion. In fact the values were highly consistent over the period of study pointing towards the stability of the dispersion. The turbidity measured for SANP was consistent to some extent, even though they presented slight variation which could be related to instrumental fluctuations. Fairly high turbidity values were obtained for the PANP and DANP dispersions which showed gradual decrease over days and subsequently reached the value of water after ~3 days indicating complete sedimentation. Thus the turbidity data performed is a clear indication of aggregation in PANP and DANP based dispersions.

2.4.5 Mechanism of steric stabilisation by the surfactants

On the basis of all the scientific findings demonstrated so far in this chapter, it could be concluded that the extent of surface stabilisation as well as the size of the nucleated nanoparticles is circuitously linked to the type of surfactant employed. The present section inspects the possible chemistry behind the steric stabilisation of the nanoparticles by the surfactants. For understanding the same, model of a nanoparticle in a dispersion media has been projected. As explained in the first chapter, the overall energy of interaction between two particles can be expressed as[33]

$$E = E_{vdW} + E_s \quad (5)$$

where E_{vdW} and E_s correspond to the contributions from van der Waals force of attraction and steric repulsion respectively. Due to the influence of van der Waals attractive forces, nanoparticles usually have the tendency to come closer and aggregate. But when the surface is modified using a capping agent, the fate of the particle is decided by the combined effect of attractive and repulsive force. The repulsive force is usually exerted by the steric effect produced by the surfactants which prevents the particle to approach closer. Surfactants are usually bulkier groups like long chain fatty acid, polymers etc. and an effective stabilisation is induced over the particle surface when the steric repulsion is strong enough to overcome the effect of the attractive forces. PANP and DANP failed to provide effective steric stabilisation which could be attributed to their respective structure and mode of linkage with the nanoparticle surface. Even though the basic skeleton of PAA consists of long alkyl chain, the molecule is attached to the particle *via* the carboxylate group. The particular fashion of its attachment with nanoparticle as depicted in Scheme 2.1 can be compared to a rope winding a play ball. Instead of existing linearly, the

polymer has been twisted over the nanoparticles surface, thus minimising the steric effect which extends to the length of only a single C–H bond in the PAA. Thus despite the long alkyl chain, the steric effect provided by PAA was not strong enough to overcome the attractive forces which pursued the particles to agglomerate. But the attachment of the polymer could prevent the crystal growth to bestow ultra fine crystals in the order of 2 nm which is considerably smaller compared to that produced without any surface modification (UCNP).

For the fatty acids, the stabilisation was more effective than that of PANP. The mode of attachment of fatty acids over the particle (Scheme 2.1) is such that the whole alkyl chain will be protruding out of the particle surface inducing high steric crowdiness depending on their chain length. In fact, the steric effects will be function of their chain length and longer chain fatty acids are more efficient in stabilising the particles sterically. This fact could be correlated with our observed results which displayed that SA and OA with chain length corresponding to 18 carbons were more effectual in producing well separated particles than DA which consists of only 10 carbons in their alkyl back bone. This presumption could be reflected in the TEM images which displayed well separated spherical SANP and OANP whereas slightly agglomerated DANP.

In short, both SA and OA performed as effective stabilisers for the nanoparticles as inferred from TEM images. However, TEM analysis indicated a prominent difference in the size of particles stabilised by the two surfactants. While D_{TEM} of SANP was ~5 nm, OANP consists of fine particles with dimension ~2 nm. This irregular demeanour of the two fatty acids could be attributed to their structural diversity. The conceptual path way of the proposed mechanism has been portrayed in Scheme 2.2. Even though the number of carbons in both the molecules is same, OA

has a kink at C9 position owing to the unsaturated bond present in it. At the same time, SA is a straight chain fatty acid with no unsaturation.

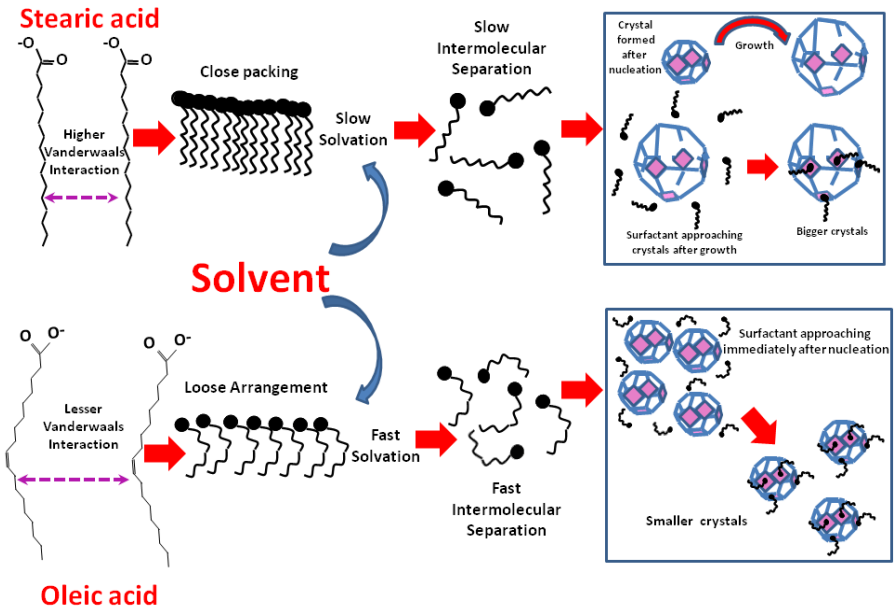

Scheme 2.2 Proposed mechanism showing the effective size reduction of nanoparticles brought about by OA compared to SA, on account of its kinked structure.

Due to the linear structure, each atom in individual SA molecule could readily mingle with that of their adjacent chain, thus enhancing the van der Waals interaction between them.[49] In the case of OA, due to its bent structure, the molecules are restricted to interact substantially with each other. Consequently, SA molecules remains more closely packed when compared with OA, owing to the higher van der Waals interaction. In the reaction medium, the separation of each molecule by the solvent will be, in turn, affected by this intermolecular attraction. While OA could be solvated easily by diphenyl ether, there will be a delay for the solvent to separate each SA molecule.[33] During this delay time, the nucleated ceria crystal might have undergone slight growth to form larger particles and later the separated SA molecule will stabilise these large grains. In the case of OA, due to the easier intermolecular

separation, the moiety could approach the particles immediately after nucleation and protect them from growth so that the stabilised particles are smaller in size.

2.4.6 Size related optical properties of the nanoparticles

The optical properties of the nanoparticles have been explored by analysing their absorption and emission spectra. Fig. 2.9(a) represents the UV spectra of all the synthesised samples, which revealed the size dependent absorption properties of the nanoparticles. The optical band gap 'E_g' of the samples was also calculated graphically from the equation[50]

$$(\alpha h\upsilon)^n = B\,(h\upsilon - Eg) \qquad (6)$$

where '$h\upsilon$' is the photon energy, 'α' the absorption coefficient, 'B' a constant for the material and 'n' is ½. From the plot of $(\alpha h\upsilon)^{1/2}$ versus photon energy, the band gap of the particles can be deducted, which is shown as Fig. 2.9(b).

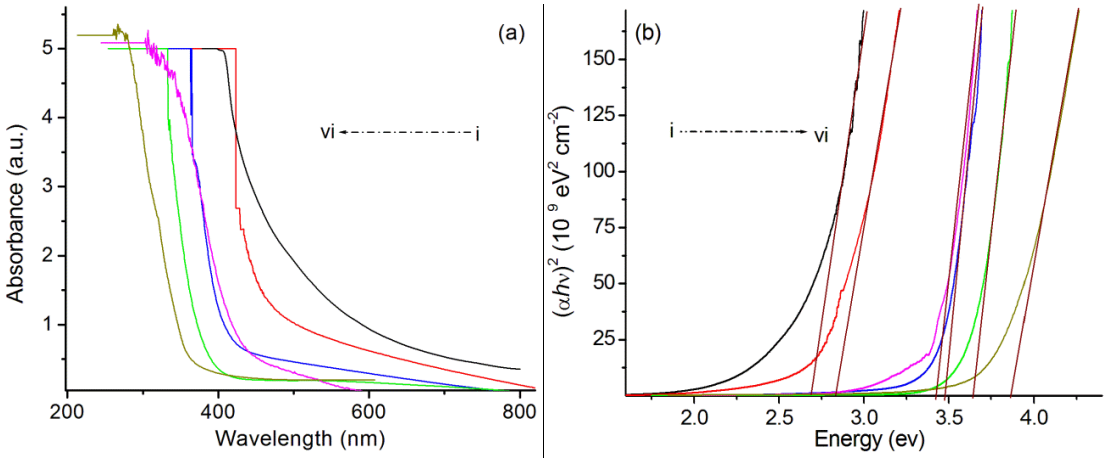

Fig. 2.9 (a) UV–visible spectra, and **(b)** graphical deduction of band gap correspond to (i) OANP (ii) PANP (iii) DANP (iv) UCNP (v) SANP and (vi) bulk ceria.

The band gap calculated so, matches well with the maximum absorption wavelength (λ_{max}) of the particles from its UV spectra. Bulk ceria usually absorbs light in the UV region with a band gap of ~4 eV owing to O_{2p} to Ce_{4f} transition and is commonly used as a UV blocker.[51] In the present study, bulk ceria possess

absorption at ~320 nm with a band gap close to 3.8 eV. All the other samples showed a size dependent shift in absorbance with respect to the bulk. As the shift is towards the lower energy region, it could be generalised that in comparison to bulk, a red shift in absorbance is observed for the ceria nanoparticles with respect to reduction in size. The order of the band gap was also in accordance with the λ_{max}. It is noteworthy that when the size is reduced from bulk to the order of 2 nm, its absorption exhibited a red shift of ~100 nm and the smallest particle synthesised in the present study, OANP, showed its absorption edge at ~415 nm.

The PL spectra of the samples as shown in Fig. 2.10 proved to be an imitation of its absorption spectra with the particles showing a shift in emission toward the visible region depending on their respective size. As emission wavelength is mostly the absorbed energy emitted by the molecule after undergoing some vibrational changes, the PL peaks usually appears at a slightly lower energy than its absorption. So the trend in the emission behaviour of the present samples as a replication of its UV spectra is no way an unanticipated phenomenon.

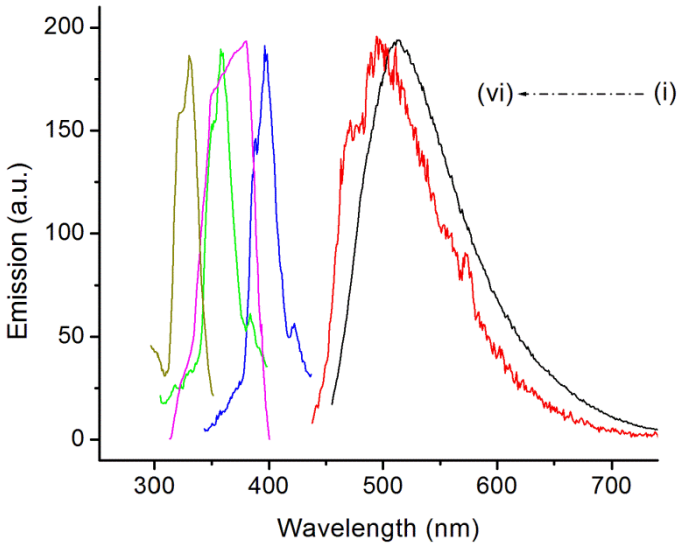

Fig. 2.10 PL spectra of the specimens (i) OANP (ii) PANP (iii) DANP (iv) UCNP (v) SANP and (vi) bulk ceria.

The most remarkable impact of the reduction in size could be visualised in the PL spectra, as OANP having the highest shift exhibits its emission peak in the visible region corresponds to a wavelength of 515 nm. Usually, semiconductor nanocrystals displays blue shift in absorbance during the nanoscaling process, due to the existence of a phenomenon called quantum confinement in association with the miniaturisation of the crystal dimension.[52] Under such situation, their zero dimensions restrict the number of electrons, causing the quantisation of energy levels in their optical bands leading to the widening of band gap. As a result, their absorption will be reallocated and the subsequent emission will be usually in the visible region, the displayed colour being dependent on the size of the particles. In fact, the design of devices based on these materials generally called as 'quantum dots' is relied on this size dependent property. In contrast to this, the presently investigating system exhibited a reverse effect of red shift in its optical properties as implied by their absorption and emission spectra. Even though, the optical comportment of the nanoparticles was in contradiction to the existing theory of semiconductor nanocrystals, as the absorption of bulk ceria is in the UV region, the overall outcome of the red shift in absorbance infact ultimately shuffled the emission of the finest nanoparticle to the visible region, which is indubitably a beneficial aspect.

Among the specimens under study, OANP and PANP showed emission in the green region owing to their fine size. Compared to PANP, OANP yielded stable suspension due to the efficient surface stabilisation. The fabrication of practical devices generally demands dispersion of the corresponding nanoparticle in suitable solvents with the intention that they can be interact effectively with other components. The ability of OANP to produce stable dispersion along with green emission opened up the possibility of tailoring it for many practical applications which distinguishes it

from other samples under study. So in the present study, OANP has been optimised as the suitable specimen for carrying out further investigation and most of the later sections of this chapter mainly focus OANP. The luminescence quantum yield of OANP dispersion in toluene has also been measured relative to a reference solution of quinine sulphate in 1N sulphuric acid (ϕ = 54.6%), the principle being explained in the section involving instrumental methods of analysis. Accordingly, the internal quantum yield of OANP was derived to be a fairly good value of ~42%, indicating its futuristic scope as a luminescent material.

For the further investigation of the optical properties, OANP was examined under a fluorescent microscope and was excited with three different wavelengths, 350, 405 and 532 nm. The observed fluorescent microscopy images are shown in Fig. 2.11.

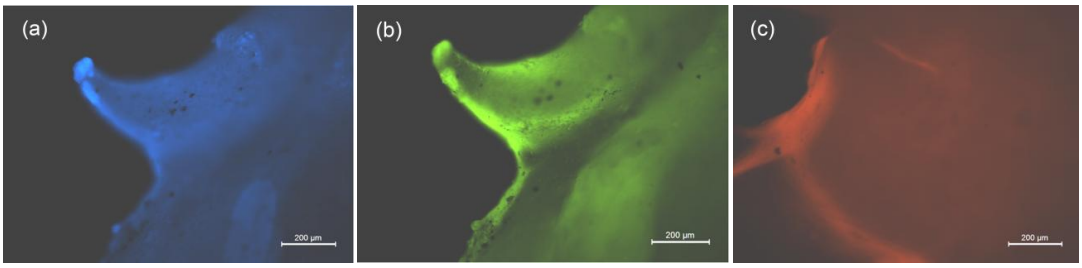

Fig. 2.11 Fluorescent microscope images of OANP at excitation wavelengths (a) 350 nm (b) 405 nm and (c) 532 nm.

It could be inferred that a number of distinct colours could be visualised at variable excitation wave lengths; blue, green and red with excitation at (λ_{ex}) 350 , 405 and 532 nm respectively. Among these, the green colour emission at λ_{ex} = 405 nm was more intense compared to others and the respective PL spectra is already included in Fig. 2.10. For confirmation of the two other emissions, PL spectra of OANP were taken with excitations at 350 and 532 nm which are shown as Fig. 2.12.

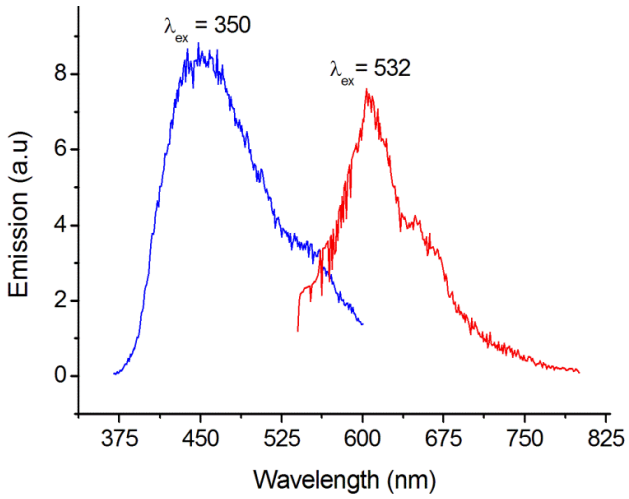

Fig. 2.12 PL of OANP at excitation wavelengths 350 and 532 nm, showing emission peaks at 450 and 604 nm.

The spectra show peaks at 450 nm (blue region) and 604 nm (red region) corresponding to the excitations, thus agreeing with the observations of fluorescent microscopy. As similar to the images, the PL peaks for blue and red emission were less intense compared to that of green. In fact, the multi-coloured emission indicates that optical bands of the particles allow its simultaneous excitations to various energy levels.

2.4.7 Mechanism of red shift and multi-coloured emission

The quantum confinement concept could be applied to explain variations in band gap of nanocrystals and its consequent influence in optical properties, when there is no change in their chemical structure, while approaching the nano dimension. But in ceria, due to the lower energy requirement for the interconversion between two oxidation states (1.72 eV), the +3 state exists to some extent, along with the +4 oxidation state, which is capable of influencing the electronic properties. In accordance with previous studies, the shape as well as the size of ceria nanostructures is pivotal in determining the stoichiometric concentration of Ce^{3+} -to- Ce^{4+} ratio of the domain.[53,54] The surface entropy of Ce^{3+} ions is higher than that of the bulk which

causes most of the surface atoms to exist in the +3 oxidation state.[55] Therefore, as surface area increases in relation to size and shape, the Ce^{3+} : Ce^{4+} ratio will subsequently increase. In that case, optical performance of the structure will be the resultant function of interaction between different factors like oxygen vacancies, defect distribution, structural composition etc.[56] So it is necessary to explore the microstructural features of ceria in association with size reduction before proposing a mechanism for the optical behaviour.

As known, in the crystal lattice of ceria, each Ce^{4+} is surrounded by eight equivalent O^{2-} ions to form a perfect cubic fluorite structure.[53] The introduction of Ce^{3+} in the lattice due to the reduction in particle size and associated increase in grain boundary perturb the whole situation, by inducing lattice distortion and creating oxygen vacancies.[57] The understanding is that, compared to a pure ceria surface with 100% Ce^{4+} ions, the presence of Ce^{3+} in the crystal lattice induces localisation of charge over the cerium sites, as the introduction of one electron to the Ce*4f* state rearranges the electronic configuration to Ce$4f^1$.[56] As oxygen vacancies are formed in the neighbouring oxygen sites of these reduced Ce^{3+} ions, it could be assumed that the charge is localised near the oxygen vacancy sites. Subsequently, the localised charge density will influence the electronic structure of the crystal to create an intermediate band (IB) in between the valence band (VB) and conduction band (CB) which would be reflected in its optical performance with a red shift in absorbance.[57-59] The width of this gap state in turn depends on certain factors like the nature of the reduced surface, the number of surface atoms as well as the abundance of the reduced sites. According to the theoretical studies conducted by Nolan *et al.* a difference of 0.5 eV was deducted for the IB bands created over (111) and (110) surfaces.[57] For particles with different size, depending upon the surface area, Ce^{3+} content and the

nature of the reduced surface, there will be consequent variation in the width of IB which in turn affects the resultant optical band gap, consistent with the results of the present study.

Another aspect to be considered is that the formation of the oxygen vacancies will considerably affect the lattice symmetry. This is brought about by the difference in the ionic radii of Ce^{3+} and Ce^{4+} which are 1.034 and 0.92 Å respectively.[53] So, when Ce^{3+} replaces Ce^{4+} in a perfectly symmetric cubic fluorite crystal lattice, the Ce–O bond length will be subsequently altered. There is a small lengthening of around 0.03 Å in the Ce–O bonds involving the Ce^{3+} ions, while the two neighbouring Ce–O distances involving the Ce^{4+} ion are shortened by 0.1 Å, due to the moving away of oxygen atoms linked to the Ce^{3+} ions towards Ce^{4+} as shown in Fig. 2.13. Also due to the disappearance of the negatively charged oxygen ions in the vacancy site, the two adjacent Ce^{3+} ions will be moved farther to each other, due to electrostatic repulsion.

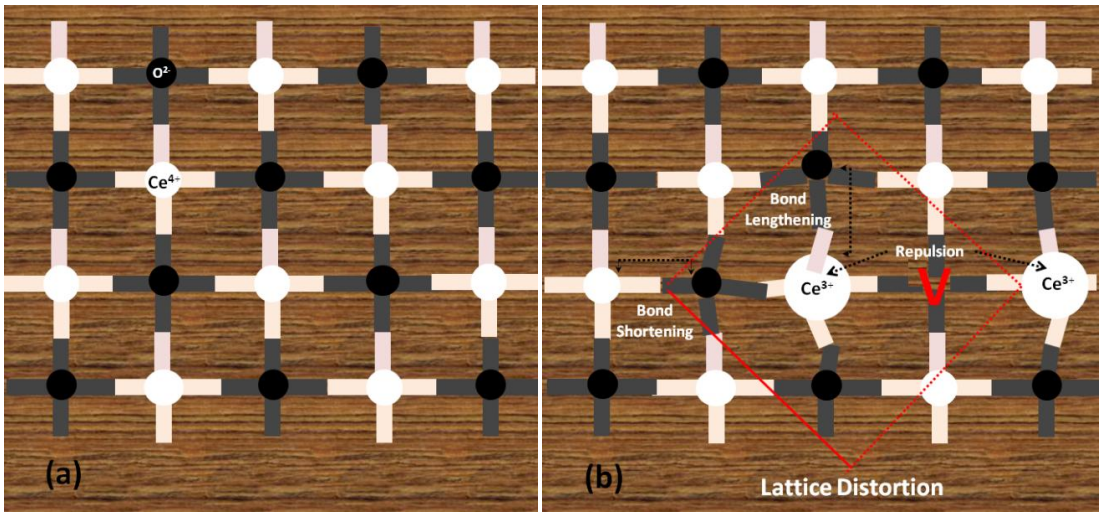

Fig. 2.13 Cartoon diagram showing the surface of ceria (a) with intact crystal structure, and (b) distorted structure due to the presence of Ce^{3+}.

The overall distortion in the symmetry and change in bond length happening around the vacancy site further influence the coulombic interaction among individual ions

and electronic states which could be reflected in the band gap of the crystals with the creation of a large number of energy levels called 'defect levels'.

The red-shift in the optical properties and multi-colour emission of OANP could be explained based on the facts stated above and accordingly a mechanism has been proposed which is schematically represented as Scheme 2.3. The IB formed in OANP due to the size induced high Ce^{3+} content is ~2.6 eV above the VB and the photon absorption at 405 nm (λ_{max}) is most probably due to the excitation of electron to the newly formed IB. As a result a red shift of ~100 nm corresponding to 1.5 eV (4−2.6 eV) with respect to bulk ceria could be observed. The other two emissions could be attributed to the excitation of electron to various defect energy levels present in the band gap. The electron gets excited to these levels by absorbing energy corresponding to the difference between the particular level to that of VB.

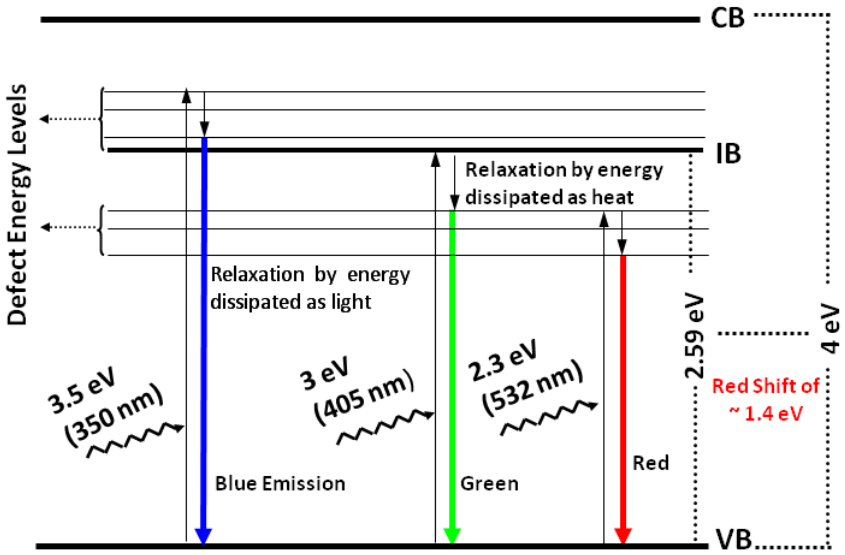

Scheme 2.3 Mechanistic presentation showing red shift in the absorbance and multi-coloured emission of OANP.

Subsequently, when it relaxes back to the VB, the emission wavelengths corresponds to different regions of visible spectrum, thus displaying multi-colour discharge. Upon excitation with 350 nm (3.5 eV), the electrons are excited to a high defect energy

level and the resultant emission is in the blue region. When excited with 405 nm (3 eV) the electrons are excited to the IB resulting in green emission. Electrons are excited to a low energy defect level on excitation with 532 nm (2.3 eV) resulted in red emission.

2.4.8 Spectroscopic validation of the proposed mechanism

For correlating the proposed mechanism with experimental observations, the spectroscopic data of the samples have been analysed carefully. If we look back at the XRD patterns of the samples, it could be observed that the patterns were exceptionally broad for OANP and the D_{XRD} was calculated as 0.7 nm. If we consider the lattice constant of ceria which is ~0.5 nm, the D_{XRD} of 0.7 nm obviously indicates that an individual crystallite is comprised of only a single crystal lattice which is highly unfeasible. This discrepancy is due to the fact that the Scherrer formula employed for calculating D_{XRD} ignores broadening of the diffraction peaks due to the microstrain in the lattice. If this formula is employed in systems with a possibility of microstrain in the crystals, the D_{XRD} value will be usually under estimated. Therefore the unusually low crystallite size and the broad XRD patterns indicate that OANP is highly strained in their crystal lattice. As mentioned earlier, replacement of Ce^{4+} by the bigger Ce^{3+} ion leads to the distortion of local symmetry and as a result the lattice will be under strain. In order to afford the bigger Ce^{3+} in the lattice comfortably and thus balance the strain, the lattice will undergo slight expansion which may be reflected in its XRD patterns.[52,53] The lattice strain and expansion of the investigated samples, calculated from the XRD patterns with bulk ceria as control along with their optical band gap has been presented in Table 2.3.

Table 2.3 Compilation of spectroscopic data of the nanoparticles from the XRD and absorbance profiles

Sample	D_{XRD} (nm)	Lattice constant '*a*' (nm)	Lattice expansion (%)	Lattice strain (%)	Band gap (eV)
OANP	0.7	0.5457	86	11	2.6
PANP	1.2	0.5449	70	8	2.8
DANP	2.1	0.5442	57	4	3.3
UCNP	2.4	0.5436	46	4	3.4
SANP	3.2	0.5418	13	2	3.6
Bulk	0.5	0.5411			

It could be interpreted that as size of the crystal decreases, there is a subsequent increase in lattice strain and associated expansion. As this trend is presumed to be an outcome of the variation in Ce^{3+} with enhanced particle surface, the subsequent decrease in band gap can be considered as elementary experimental evidence to support the projected conjecture.

The nature of the optical spectra could also serve as a benchmark to rationalise the proposed mechanism. While considering the absorbance profile, it could be noted that the decrease in particle size is followed by the appearance of an extended tail in the spectra, which broadens with reduced size. With reference to literature, this extended low energy tails are associated with the defects present in the crystal.[24] The broad PL spectra of synthesised nanoparticles of fine size preferably in the order of ~2 nm also implies the defect crystal lattice of the particles. The broadness was more prominent for OANP and PANP and it spreads over the range of 410 to 750 nm; the characteristic emission bands for typical defective ceria nanocrystals according to previous literatures.[20] Thus it could be summarised that the optical behaviour of the

particles, especially the broad peaks is pointing towards the presence of large scale defects and higher Ce^{3+}, which again supports the mechanism.

According to the mechanistic assumption, the role of Ce^{3+} in the crystal structure is critical in controlling the behaviour of the nanoparticles. Therefore, XPS spectroscopy has been adopted to estimate the Ce^{3+} content in selected samples, OANP, UCNP and bulk.

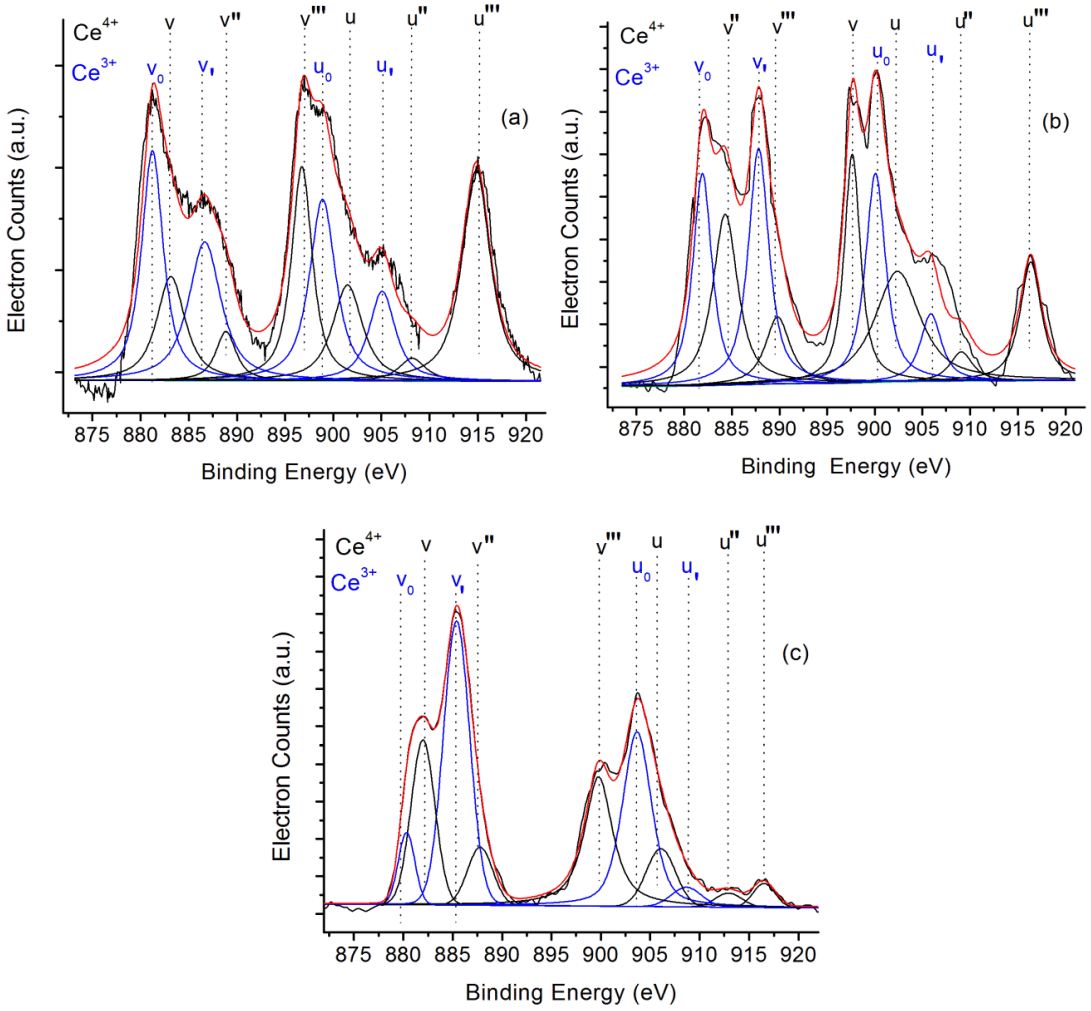

Fig. 2.14 Deconvoluted XPS spectra representing the Ce 3d core level of (a) Bulk (b) UCNP and (c) OANP.

Fig. 2.14 shows the XPS spectra corresponding to the Ce 3d core levels of the samples. For the calculation of Ce^{3+} content, the spectra have been deconvoluted to differentiate individual peak. The spectra display Ce 3d electron core level which is

characterised by $3d_{5/2}$ and $3d_{3/2}$ series peaks, assigned as v_0, v_1, u_0, and u_1 peaks attributed to Ce^{3+}; while v, v'' , v''', u, u'' and u''' are due to Ce^{4+}.[60] The concentrations of Ce^{3+} in the samples were calculated from the integrated area of individual deconvoluted peaks in the spectra obtained using the deconvolution software, the details being given in the section involving instrumental methods of analysis. The total Ce^{3+} concentration is derived as the ratio of the sum of the area all Ce^{3+} peaks to the total area. Accordingly, the Ce^{3+} content was estimated to be ~7, 24 and 42% for bulk, UCNP and OANP respectively. In fact, the variable Ce^{3+} content of the specimens could be easily understood by comparing the intensities of the various peaks in the deconvoluted spectra itself. The estimation revealed that the Ce^{3+} content varies inversely with particle size, which is obviously due to the stability of Ce^{3+} at the enhanced surface during the process of size reduction. Fig. 2.15 showing the O1s levels of the samples displays two major peaks at ~ 528.2 corresponding to oxygen coordinated with Ce ions in the lattice and 530.5 eV attributed to the oxygen absorbed over the vacancy site.[61] It could be implicated that there is a successive increase in intensity of the oxygen vacancy peak with decrease in particle size, inferring the enhanced defects associated with miniaturisation of crystals.

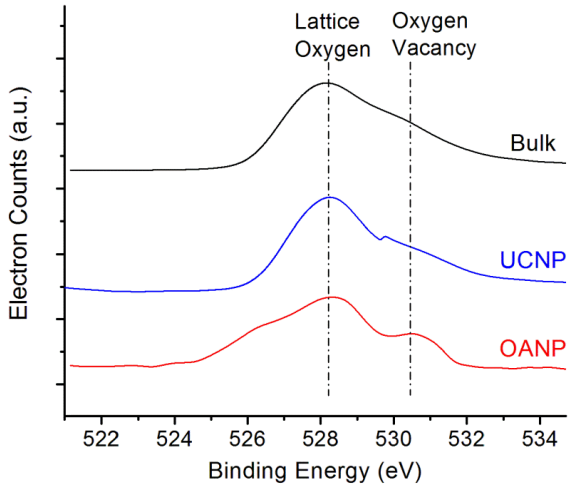

Fig. 2.15 XPS spectra of the specimens displaying the O 1s energy level.

In short, it is observed that when the dimension of the particle is diminished, the Ce^{3+}-to-Ce^{4+} ratio is augmented, which might have influenced its electronic structure causing variation in optical properties. Thus the XPS analysis proved to be a strong evidence for the verification of the proposed mechanism based on Ce^{3+} content and defects.

Raman spectroscopy profiles of the above cited samples are shown in Fig. 2.16. Bulk ceria displayed a Raman peak at 469 cm^{-1} which is assigned to the vibrational mode of the F_{2g} symmetry in a cubic fluorite lattice.[62] The same peak was slightly shifted to 464 and 452 cm^{-1} respectively for UCNP and OANP, which was broader than that of the bulk. The broadening and shift of Raman bands towards lower energies is assigned to be due to the nanosize of the crystal and the results are consistent with earlier reports.[24]

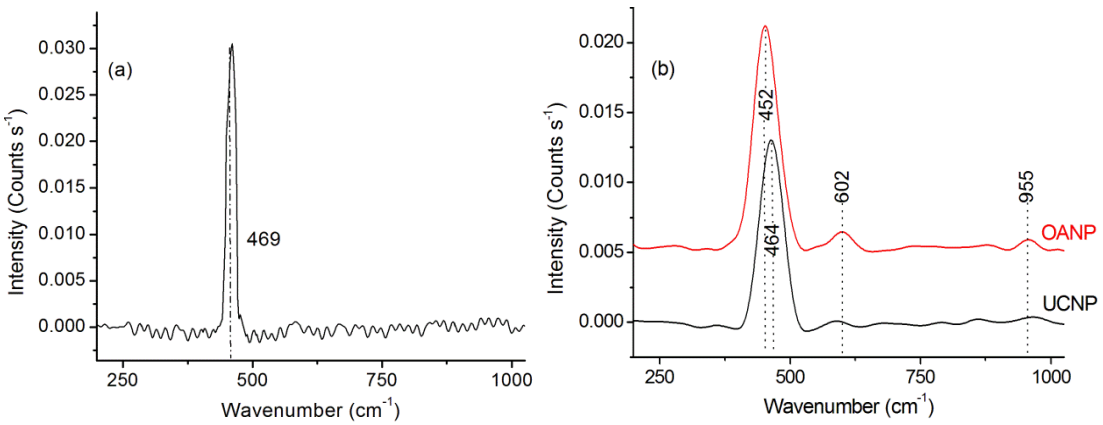

Fig. 2.16 Raman spectra of the specimens (a) bulk, and (b) OANP and UCNP taken at room temperature with an excitation wavelength of 1064 nm.

The Raman spectra of OANP and UCNP also contain weak bands at about 602 and 955 cm^{-1} which are related to the defects in the system. The peak at 602 cm^{-1} is attributed to the formation of defect species with octahedral symmetry that included a cation in 8-fold coordination of O^{2-}.[63] The evolution of this type of detects could be related to the presence Ce^{3+} with a different radius than the Ce^{4+} ions. Therefore, the

peaks at 602 cm^{-1} definitely indicates the presence of Ce^{3+} in the system. The peak at 955 cm^{-1} is assigned to peroxide species adsorbed at the one-electron defect site created by the oxygen vacancies.[62,64] These two peaks corresponding to the defects were fairly intense in OANP when compared with UCNP, whereas completely absent in the bulk. This fact again indicates the increased Ce^{3+}concentration of ceria with reduction in size.

The red shift in the optical properties of ceria has already been mentioned in some of the research articles based on ceria. Devaraju *et al.* observed a red shift in absorbance properties of rod like ceria nanoparticles which was correlated to the presence of oxygen vacancies in the crystal owing to the particular morphology.[65] Sun *et al.* reported a red shift of ~50 nm for ceria nanorods and they also explained

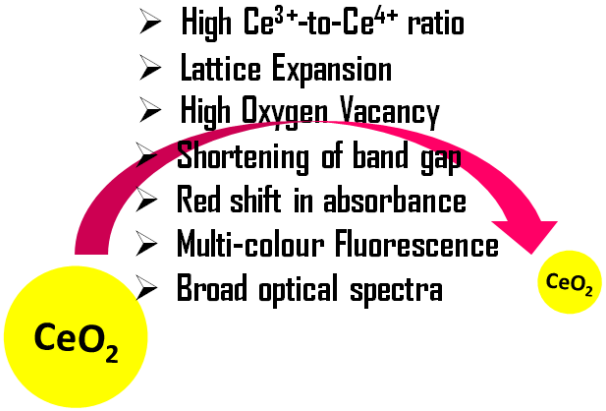

Fig. 2.17 Summary of the novel properties associated with nanoscaling of ceria on the basis of the present study.

the phenomenon based on the defects in the crystals.[66] In the present study, after detailed spectroscopic investigation, it is concluded that when the dimension of ceria is reduced, a subsequent amount of Ce^{3+} will be introduced in the lattice, causing distortion to the crystal symmetry. As a result, the electronic structure of the crystal will be affected causing a red shift in the optical band gap. The phenomenon is accompanied by a series of novel properties which is summarised in Fig. 2.17.

2.5 Conclusions

Ceria nanoparticles with size, typically below ~10 nm could be engineered by adopting facile synthetic strategies based on precipitation and thermal decomposition, with the aid of surfactants. XRD and TEM analysis implied the formation of cerium oxide crystals and FT-IR studies revealed that the surfactants were successfully chemisorbed on the nanoparticle surface, thus justifying the adopted protocol. Among the specimens, ceria nanodots of finest size ~2 nm could be fabricated by thermally decomposing cerium acetate in diphenyl ether in the presence of oleic acid as the surfactant. Compared to other surfactants, oleic acid was more efficient in forming smaller crystals as evidenced from TEM images, which was attributed to its particular kinked structure and a mechanism was proposed to rationalise this inference. The particle exhibited a size dependence on their optical behaviour as revealed by UV-Visible and PL spectra, with a subsequent decrease in band gap during the miniaturisation of the crystal. The detailed spectroscopic investigation carried out on the particles exposed that role of Ce^{3+} is pivotal in influencing the electronic structure of ceria by distorting the lattice symmetry and inducing defects in the crystals. On the basis of the present study, a mechanism was proposed to justify the effect of size which was verified using XRD, XPS and Raman spectroscopy. Careful observation of the spectroscopic data also revealed that the reduction in size of ceria crystal is followed by a series of novel properties which are capable of bringing radical changes in the techno-commercial aspects of ceria.

2.6 References

1 M. Thomas, S. K. Ghosh and K. C. George, *Mater. Lett.*, 2002, **56**, 386-392.

2 X. Michalet, F. F. Pinaud, L. A. Bentolila, J. M. Tsay, S. Doose, J. J. Li, G. Sundaresan, A. M. Wu, S. S. Gambhir and S. Weiss, *Science*, 2005, **307**, 538-544.

3 J. M. Luther, J. Gao, M. T. Lloyd, O. E. Semonin, M. C. Beard and A. J. Nozik, *Adv. Mater.*, 2010, **22**, 3704-3080.

4 E. Jang, S. Jun, H. Jang, J. Llim, B. Kim and Y. Kim, *Adv. Mater.*, 2010, **22**, 3076-3080.

5 E. Beaurepaire, V. Buissette, M. P. Sauviat, D. Giaume, K. Lahlil, A. Mercuri, D. Casanova, A. Huignard, J. L. Martin, T. Gacoin, J. P. Boilot and A. Alexandrou, *Nano Lett.*, 2004, **4**, 2079-2083.

6 S. Arora, J. M. Rajwade and K. M. Paknikar, *Toxicol. Appl. Pharm.*, 2012, **258**, 151-165.

7 I. Celardo, J. Z. Pedersen, E. Traversa and L. Ghibelli, *Nanoscale*, 2011, **3**, 1411-1420.

8 W. Sun and W. Liu, *J. Power Sources*, 2012, **217**, 114-119.

9 S. Yabe and T. Sato, *J. Solid State Chem.*, 2003, **171**, 7-11.

10 S. H. Lee, Z. Y. Lu, S. V. Babu and E. Matijevic, *J. Mater. Res.*, 2002, **17**, 2744-2749.

11 E. Bekyarova, P. Fornasiero, J. Kaspar and M. Graziani, *Catal. Today*, 1998, **45**, 179-183.

12 H. J. Beie and A. GnÃrich, *Sensor Actuat. B*, 1991, **4**, 393-399.

13 N. Rane, H. Zou, G. Buelna and J. Y. S. Lin, *J. Membrane Sci.*, 2005, **256**, 89-97.

14 S. Fujihara and M. Oikawa, *J. Appl. Phys.*, 2004, **95**, 8002-8006.

15 A. H. Morshed, M. E. Moussa, S. M. Bedair, R. Leonard, S. X. Liu and N. ElMasry, *Appl. Phys. Lett.*, 1997, **70**, 1647-1649.

16 S. Maensiri, C. Masingboon, P. Laokul, W. Jareonboon, V. Promarak, P. L. Anderson and S. Seraphin, *Cryst. Growth Des.*, 2007, **7**, 950-955.

17 S. H. Yu, H. Colfen and A. Fischer, *Colloids Surf. A*, 2004, **243**, 49-52.

18 M. Inoue, M. Kimura and T. Inui, *Chem. Commun.*, 1999, 957-958.

19 T. Taniguchi, T. Watanabe, N. Sakamoto, N. Matsushita and M. Yoshimura, *Cryst. Growth Des.*, 2008, **8**, 3725-3730.

20 A. Ahniyaz, Y. Sakamoto and L. Bergstrom, *Cryst. Growth Des.*, 2008, **8**, 1798-1800.

21 F. Dang, K. Kato, H. Imai, S. Wada, H. Haneda and M. Kuwabara, *Cryst. Growth Des.*, 2010, **10**, 4537-4541.

22 H. L. Lin, C. Y. Wu and R. K. Chiang, *J. Colloid Interf. Sci.*, 2010, **341**, 12-17.

23 T. Masui, K. Fujiwara, K. Machida, G. Adachi, T. Sakata and H. Mori, *Chem. Mater.*, 1997, **9**, 2197-2204.

24 T. S. Sreeremya, K. M. Thulasi, A. Krishnan and S. Ghosh, *Ind. Eng. Chem. Res.*, 2012, **51**, 318-326.

25 L. Manna, E. C. Scher and A. P. Alivisatos, *J. Am. Chem. Soc.*, 2000, **122**, 12700-12706.

26 Y. Yin and A. P. Alivisatos, *Nature*, 2005, **437**, 664-670.

27 Y. W. Jun, J. S. Choi and J. Cheon, *Angew. Chem. Int. Edit.*, 2006, **45**, 3414-3439.

28 T. D. Schladt, T. Graf and W. Tremel, *Chem. Mater.*, 2009, **21**, 3183-3190.

29 Z. A. Peng and X. G. Peng, *J. Am. Ceram. Soc.*, 2001, **123**, 1389-1395.

30 T. S. Sreeremya, A. Krishnan, A. P. Mohamed, U. S. Hareesh and S. Ghosh, *Chem. Eng. J.*, 2014, **255**, 282-289.

31 T. S. Sreeremya, A. Krishnan, L. N. Satapathy and S. Ghosh, *RSC Adv.*, 2014, **4**, 28020-28028.

32 S. Y. Lee and M. T. Harris, *J. Colloid Interf. Sci.*, 2006, **293**, 401-408.

33 R. Tadmor, R. E. Rosensweig, J. Frey and J. Klein, *Langmuir*, 2000, **16**, 9117-9120.

34 H. I. Chen and H. Y. Chang, *Colloids Surf. A*, 2004, **242**, 61-69.

35 P. L. Chen and I. W. Chen, *J. Am. Ceram. Soc.*, 1993, **76**, 1577-1583.

36 X. D. Zhou, W. Huebner and H. U. Anderson, *Chem. Mater.*, 2003, **15**, 378-382.

37 M. L. Dos Santos, R. C. Lima, C. S. Riccardi, R. L. Tranquilin, P. R. Bueno, J. A. Varela and E. Longo, *Mat. Lett.*, 2008, **62**, 4509-4511.

38 V. K. Ivanov, A. V. Usatenko and A. B. Shcherbakov, *Russ. J. Inorg. Chem.*, 2009, **54**, 1522-1527.

39 S. Ghosh, D. Divya, K. C. Remani and T. S. Sreeremya, *J. Nanopart. Res.*, 2010, **12**, 1905-1911.

40 M. Taguchi, S. Takami, T. Adschiri, T. Nakane and T. Naka, *Crystengcomm*, 2011, **14**, 8736-8736.

41 L. Yan, X. Xing, R. Yu, J. Deng, J. Chen and G. Liu, *Physica B*, 2007, **390**, 59-64.

42 B. Yan and H. X. Zhu, *J. Nanopart. Res.*, 2008, **10**, 1279-1285.

43 D. Andreescu, E. Matijevic and D. V. Goia, *Colloids Surf. A*, 2006, **291**, 93-100.

44 N. Q. Wu, L. Fu, M. Su, M. Aslam, K. C. Wong and V. P. Dravid, *Nano Lett.*, 2004, **4**, 383-386.

45 N. C. Wu, E. W. Shi, Y. Q. Zheng and W. J. Li, *J. Am. Ceram. Soc.*, 2002, **85**, 2462-2468.

46 J. A. Wang, J. M. Dominguez, A. Montoya, S. Castillo, J. Navarrete, M. Moran-Pineda, J. Reyes-Gasga and X. Bokhimi, *Chem. Mater.*, 2002, **14**, 4676-4683.

47 I. Hrianca, C. Caizer and Z. Schlett, *J. Appl. Phys.*, 2002, **92**, 2125-2132.

48 C. G. Hu, Z. W. Zhang, H. Liu, P. X. Gao and Z. L. Wang, *Nanotechnology*, 2006, **17**, 5983-5987.

49 J. R. Kanicky and D. O. Shah, *J. Colloid Interf. Sci.*, 2002, **256**, 201-207.

50 H. P. Zhou, Y. W. Zhang, H. X. Mai, X. Sun, Q. Liu, W. G. Song and C. H. Yan, *Chem. Eur. J.*, 2008, **14**, 3380-3390.

51 A. Corma, P. Atienzar, H. Garcia and J. Y. Chane-Ching, *Nat. Mater.*, 2004, **3**, 394-397.

52 P. Patsalas, S. Logothetidis and C. Metaxa, *Appl. Phys. Lett.*, 2002, **81**, 466-468.

53 S. Deshpande, S. Patil, S. Kuchibhatla and S. Seal, *Appl. Phys. Lett.*, 2005, **87**, 133113.

54 H. X. Mai, L. D. Sun, Y. W. Zhang, R. Si, W. Feng, H. P. Zhang, H. C. Liu and C. H. Yan, *J. Phys. Chem. B*, 2005, **109**, 24380-24385.

55 W. C. Chueh, A. H. McDaniel, M. E. Grass, Y. Hao, N. Jabeen, Z. Liu, S. M. Haile, K. F. McCarty, H. Bluhm and F. El Gabaly, *Chem. Mater.*, 2012, **24**, 1876-1882.

56 P. Patsalas, S. Logothetidis, L. Sygellou and S. Kennou, *Phys. Rev. B*, 2003, **68**, 035104.

57 M. Nolan, S. C. Parker and G. W. Watson, *Surf. Sci.*, 2005, **595**, 223-232.

58 P. Wahnon, J. C. Conesa, P. Palacios, R. Lucena, I. Aguilera, Y. Seminovski and F. Fresno, *Phys. Chem. Chem. Phys.*, 2011, **13**, 20401-20407.

59 K. B. Jaimy, S. Ghosh, S. Sankar and K. G. K. Warrier, *Mater. Res. Bull.*, 2011, **46**, 914-921.

60 L. S. Zhong, J.-S. Hu, A.-M. Cao, Q. Liu, W.-G. Song and L. J. Wan, *Chem. Mater.*, 2007, **19**, 1648-1655.

61 Y. W. Zhang, R. Si, C. S. Liao and C. H. Yan, *J. Phys. Chem. B*, 2003, **107**, 10159-10167.

62 J. Guzman, S. Carrettin and A. Corma, *J. Am. Chem. Soc.*, 2005, **127**, 3286-3287.

63 L. Li, F. Chen, J. Q. Lu and M. F. Luo, *J. Phys. Chem. A*, 2011, **115**, 7972-7977.

64 M. Guo, J. Q. Lu, Y. N. Wu, Y. J. Wang and M. F. Luo, *Langmuir*, 2011, **27**, 3872-3877.

65 M. K. Devaraju, S. Yin and T. Sato, *ACS Appl. Mater. Interfaces*, 2009, **1**, 2694-2698.

66 C. W. Sun, H. Li, H. R. Zhang, Z. X. Wang and L. Q. Chen, *Nanotechnology*, 2005, **16**, 1454-1463.

CHAPTER 3

Design of Cerium oxide as a FRET probe for the identification of fatty acids by virtue of concentration quenching phenomenon

3.1 Abstract

This chapter presents a Förster resonance energy transfer (FRET) based quenching mechanism for the fluorescence exhibited by cerium dioxide based dispersions. The emission intensity of the size induced green fluorescence exhibited by the ultra fine cerium dioxide nanoparticles showed a dependence on the concentration of the dispersion and a detailed spectroscopic investigation has been carried out on the fluorescence quenching phenomenon prevailed in the system.

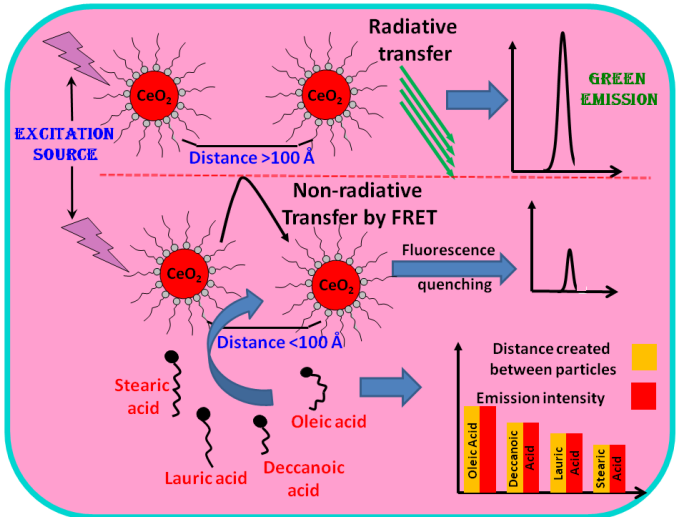

It was proposed that, a concentration dependent non-radiative pathway has been revealed to the particles due to the close proximity between them, which rendered the extinction of fluorescence. The calibration plot according to the Stern-Volmer equation showed a good linear relationship within the error limit and the value of Q denoting exchange interaction was close to 6 implying dipolar coupling between particles. Theoretical analysis of spectroscopic data exposed that Förster resonance energy transfer (FRET) is the dominant mechanism responsible for the interparticle

excitation transfer and the Förster radius (R_0) calculated was 68.6 Å. The distance dependence of FRET has been utilised to explicate the conformation and chain length of fatty acids by interrupting the energy transfer efficiency between particles and thus a simple analytical tool based on FRET for the qualitative assessment of fatty acids have been projected.

3.2 Introduction

The physical dimensions of semiconductor nanocrystals often serve as a resource of innovative photochemical properties owing to quantum confinement. Due to their nano scale, usually smaller than the exciton Bohr radius, these 'artificial atoms' are called as quantum dots and their zero dimension restricts the number of electrons which imparts the quantisation of energy levels in the density of states (DOS).[1] The most fascinating outcome of this phenomenon could be reflected in their band gap, which ends up with novel optical properties.[2] The influence of nano dimension on the band gap endorses the tunability of the optical properties of nanoparticles, thus rendering a wide range of applications.

Cerium dioxide is a distinguished semiconductor, capable of executing multifunctional tasks, owing to its versatile properties like oxygen storage capacity, redox nature, non toxicity, high refractive index, chemical and thermal stability etc.[3-7] In fact, while its Bohr radius has been taken into account, which is ~7 nm, ceria based nano structures with appropriate dimensions are proficient in exhibiting innovative optical propertie.[8] Certain ceria based research has revealed the ability of this nanoparticulate rare earth oxide to emit in the visible region with wavelength corresponding to green region, when they achieve very fine aspect ratio, usually below 3 nm. Morshed *et al.* observed an emission peak near 400 nm for ceria based thin film deposited on a Si(111) substrate by pulsed laser ablation, in 1997.[9] In 2007, Maensiri *et al.* reported green coloured photoluminescence for clusters of ceria nanoparticles synthesised from cerium(III) acetate hydrate and freshly extracted egg white in aqueous medium.[6] A strong blue emission was observed by Yu *et al.* for ceria nanoparticles with average particle size of 1.8 nm prepared by a hydrothermal method showing a photoluminescence peak at 425 nm.[10] In the light of the scarcity

of superlative luminescent materials, the control and improvement of the properties of existing nano phosphors have always been a major aspiration in the world of research.[11] While designing efficient phosphor materials, phenomena like luminescence enhancement, quenching, delay in emission, decay rate etc. deserves vital significance. Among these, quenching of luminescence is a prevailing phenomenon which is highly undesirable due to the resulting reduction in overall quantum yield, which in turn affect the luminescence efficiency. But it is a bit astonishing reality that even the adverse phenomenon can be probed for many functional applications like molecular sensing, imaging, drug release profiling, DNA detection etc. if the underlying quenching mechanism is thoroughly understood.[12,13]

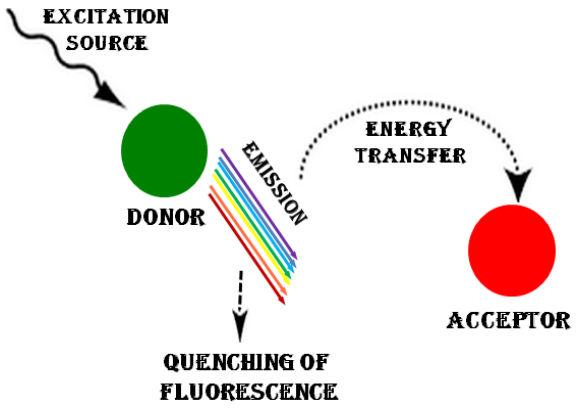

Scheme 3.1 Schematic representation demonstrating the principle of FRET

Different pathways has been proposed so far for clearing up the mystery behind fluorescence quenching, from simple collisional energy exchange to nanoparticle surface energy exchange (NSET).[12-15] In the present study, various spectroscopic tools has been employed to investigate the existence of a non-radiative energy transfer mechanism between ceria nanoparticles based on the principle of Förster Resonance Energy transfer (FRET). FRET is a distant energy transfer process making use of dipolar pairing between donor and acceptor molecules.[16] As the FRET based energy

transfer is affected by dipole-dipole coupling between the interacted molecules, the distance between them is stringently limited below 100 Å.[17] In this close proximity, the virtual photon emitted by the donor molecule is instantly absorbed by the acceptor, leading to the absence of visualising any coloured emission from the donor. The basic principle of FRET is schematically represented in Scheme 3.1. The occurrence of this non-radiative energy transfer phenomenon also stipulates the overlap between the emission and absorption spectra of donor and acceptor molecule respectively; or else the acceptor may not be excited in the expense of the donor.[18]

The discovery of the FRET phenomenon could be traced back to the beginning of the twentieth century, when Jean Perrin first proposed the mechanism of resonance energy transfer in 1918.[18] The renowned experiment by Cario and Franck in 1922 first demonstrated the energy transfer from mercury to thallium atomic vapour, when they were simultaneously excited with 254 nm.[19,20] Later, in 1928, H. Kallmann and F. London put forth theoretical explanation of this process and proposed that dipole interactions would be responsible for the energy transfer between neighbouring molecules under an intermolecular distance over 1000 Å.[21,22] In 1932, Francis Perrin, son of J. Perrin developed a quantum mechanical theory based on the studies by Kallmann and London's.[17] He mentioned the importance of the spectral overlap between the optical spectra of the interacting molecules and also estimated the average intermolecular distance to be ~250 Å for which the energy transfer might occur. Based on these initial studies, Theodor Förster in the 1940s developed a quantitative theory to describe the non-radiative energy transfer, depending on the spectral overlap and intermolecular distance.[23] He correlated the rate of energy transfer in terms of spectral overlap integral and also showed that R_0, the distance between donor and acceptor at which the energy transfer efficiency becomes 50%

could be between 10 and 100 Å. The mathematical equation proposed by him, connecting the energy transfer efficiency, distance between the molecule and R_0, which is illustrated in the later part of this chapter, paved way to the possibility of deriving the distance between donor and acceptor molecule.[17] As a tribute to his contribution towards moulding this energy transfer mechanism as one of the most sensitive tools for accessing molecular scale information, the phenomenon was named after him and the parameter 'R_0' has been termed as 'Förster radius'.

The paper "Energy Transfer: A Spectroscopic Ruler", authored by Stryer and Haughland in 1967, triggered the growing interest towards FRET based research and the last twenty years saw a huge increase in its scientific significance.[24] Due to the nanometric distance range of the participating molecules, FRET has now emerged as convenient technology at the single molecular detection limit and is found suitable for studying the distance between two molecules or two neighbouring sites on a specific macromolecule, during protein conformational change, protein interaction, enzyme activity.[25-31] Since FRET physically originates from the weak electromagnetic coupling of two dipoles, introducing additional dipole like metal nanoparticles provides more coupling interactions and thus FRET efficiency can be tuned accordingly. There have many recent efforts for the development of fluorescence assays based on this principle for applications like DNA detection,[32] imaging and sensing of molecular interactions etc.[24]

The impressive advances in FRET based research exposes that attempts are still ongoing to improve its efficiency and sensitivity, by executing novel and versatile materials as donors and acceptors. Nanoparticles including gold, silica, graphene based materials, rare-earth doped upconversion nanoparticles (UCNPs) etc. have been experimented as an alternative for traditional organic flourophores. Liu *et al.* designed

a FRET probe by incorporating graphene oxide (GO) on DNA, which revealed that GO based FRET efficiency is a function of the fourth inverse power of distance.[33] Studies by Piao *et al.* revealed the role of GO as an acceptor in the FRET system consisting of DNA.[34] Gold nanoparticles (AuNPs) are one of the most excellent metal nanoparticles suitable to be tuned as FRET substrate, owing to their remarkable properties like surface plasmon resonance phenomena, high fluorescence quenching capability etc. Tang *et al.* demonstrated a FRET based detection of glucose by fabricating a nanocomplex out of AuNPS.[35] Dubertret *et al.* developed a AuNP based FRET device for the sensitive detection of target DNA.[36] Due to the abudance and non-toxicity, silica is a commonly used matrix for FRET based bioanalysis.[18] Dye doped silica nanoparticles have been engineered as a FRET tool by Zhang *et al*. for the ultra sensitive detection of trinitrotoluene (TNT).[37] Recently silica nanoparticles, whose fluorescence can be switched reversibly between 'on' and 'off' state has also been constructed based on the principle of FRET.[38] UCNPs are another class of luminescent materials highly desirable for bio sensing applications due to its appealing feathers like no auto fluorescence from biological samples and a large penetration depth.[18] There has been some initial research works published on the studies of incorporating the principle of FRET on UCNPs. Studies by Wang *et al.* presented an immunoassay of goat antihuman immunoglobin based on a FRET substrate comprises of $NaYF_4$:Yb as UCNP and AuNPs.[39] Also the use of quantum dots as FRET pairs has also been fostered on account of its high photo stability, great emission intensity and photo bleaching resistance. Their broad absorption and narrow emission spectra allow single-wavelength excitation of multiple donors and can avoid crosstalk with acceptor fluorophores. They can also be coupled to multiple acceptor fluorophores for higher efficiency in energy transfer and can act as the support

structure for biomolecules for imaging purposes or to simplify assay design.[12] Leong *et al.* has developed a single-step quantum dot-mediated FRET system to investigate the structural composition and in vitro dynamic behaviour of plasmid DNA hybrid nanostructure.[40] Song *et al.* designed a positively-charged, compact QD–DNA complex for the detection of nucleic acids.[41]

Even though there are numerous FRET based nanoparticle assays mentioned above, aimed at different applications, there has been no attempt till date to incorporate this mechanism on ceria based system, perhaps due to the lack of adequate attention towards its optical properties. In the present chapter, the principle of FRET has been integrated with ceria nanoparticles based on the concentration dependent fluorescence quenching exhibited by the oleophilic ceria nanoparticles, OANP mentioned in the first chapter in their non-polar dispersions. The phenomenon could also be tuned as a facile analytic model which served as a method for the identification of fatty acids. .

Fatty acids are carboxylic acid with a long aliphatic chain, which can be either saturated or unsaturated. They appeared in the lime light of scientific community more than a century ago, when Chevreul first established that basic structure of fats composed of fatty acids and glycerol.[42] In the past two decades, there have been numerous research articles and books on fatty acids and a great majority of their properties have been recognised. Fatty acids differ by length and on that basis; they are categorised as Short- chain fatty acids (SCFA), Medium-chain fatty acids (MCFA), Long-chain fatty acids (LCFA) and Very Long-chain fatty acids (VLCFA). Fatty acids have many biological roles in human body. They serve as a fuel for muscular contraction and general metabolism. They are consumed by mitochondria in the cells to produce ATP through oxidation.[43] Some fatty acids are important

components of cell membranes and precursors to many biologically relevant substances involved in regulation of blood pressure and inflammatory responses.[44] Fatty acids have indispensible role in adding flavour to foodstuff as well as its preservation, during the tenure of processing.[45] Some recent researches have proved that fatty acids are capable of imparting efficient gustatory stimulus in humans, thus concreting its worth in food industry.[46] They are inevitable ingredient in the manufacture of soap; involving the saponification reaction.[47] Besides, there are plentiful other applications of fatty acids in the manufacture of a variety of resources like cosmetics, lubricants, rubber, pharmaceuticals, adhesives, waxes, insecticides, rust preventatives etc.[42]

The early adopted methods for the identification of fatty acids involve the elemental analysis of carbon, hydrogen and oxygen.[42] The presence of double bonds was estimated using certain parameters like iodine number, TITER etc. Iodine number is defined as the centigrams of iodine absorbed by 1 g of the fatty acid, whereas TITER is the temperature at which the fatty acid under goes solidification.[42] More recently, other accurate methods involving its identification based on their derivatisation to corresponding fatty acid methyl esters (FAME) has evolved. As these esters are chemically stable and volatile, they can be detected by various methods like gas chromatography, high performance liquid chromatography (HPLC), capillary electrophoresis, mass spectroscopy etc. Mjos *et al.* identified the structure of a variety of saturated and unsaturated fatty acids with number of carbons varying between 16 and 24 by electron impact mass spectroscopy (EIMS).[48] Yang *et al.* prepared a pyridine based derivative of fatty acids and analysed it *via* LC/MS.[45] Ayorinde *et al.* developed a method based on Matrix-assisted laser desorption/ionisation time-of-flight mass spectrometry (MALDI-TOF MS) with a porphyrin type molecule as

matrix for the analysis of fatty acids in commercial vegetable oils.[49] One of the drawbacks of these demonstrated methods is the laborious and time-consuming preparation of the derivative[48].

In the present chapter, focus has been given to develop a new nanoparticle based assay for the analysis of fatty acids, which is simple, cheap and time-saving compared to the existing protocols. Moreover, as mentioned earlier, despite the significant research activity in field of nano cerium dioxide and FRET in recent years, this present study is the first to report a FRET based energy transfer mechanism in ceria system. The method unanimously involves the optical behaviour of the nanoparticles in their dispersion, which has been moulded as an effective tool for the identification of fatty acids.

3.3 Experimental Section

All the chemicals were used as received without further purification. Stearic acid (90%) and lauric acid (90%) were purchased from Merck, India, decanoic acid (90%) from Sigma Aldrich and oleic acid (90%) from Alfa Aesar, UK. Common solvents of analytical grade were procured from Merck, India.

3.3.1 Preparation of samples for the investigation of concentration quenching

The sample under study is the oleophilic OANP, whose synthesis *via* thermal decomposition has been described in detail in the second chapter. The present chapter deals with the fluorescence quenching phenomenon of OANP in its non-aqueous dispersion. A parent dispersion of OANP in toluene has been prepared by suspending 0.01 g dried nanoparticles in 25 ml toluene (0.002 M) and sonicated for about 10 min. Ceria dispersions of different concentration have been prepared from this parent suspension upon dilution. Dispersions having concentrations in the range 0.0001-

0.0018 M have been prepared by dilution followed by sonication for 10 min. The quenching phenomenon has been studied by the acquisition of the photoluminescence spectra of the dispersions.

3.3.2 Preparation of samples for the structural elucidation of fatty acids

For the structural identification of different fatty acids, they have been used as spacers in the OANP dispersions. Fatty acids differing in chain length as well as structures such as decanoic acid ($C_{10}H_{20}O_2$), lauric acid ($C_{12}H_{24}O_2$), stearic acid ($C_{18}H_{36}O_2$) and oleic acid ($C_{18}H_{34}O_2$) have been used as spacers. To a fixed volume of concentrated OANP dispersion (0.0018 M), same volume of individual spacer was added. The volume of the spacer added was varied from 0.5 to 4.5 ml and the PL corresponding to the addition of each volume has been collected.

All the PL measurements have been done in triplicates to ensure the accuracy of the values.

3.4 Results and discussions

3.4.1 Optical properties of the OANP dispersions

The combined plot of the absorbance and emission spectra of OANP can be visualised in Fig. 3.1. As explained in the second chapter, due to the size induced red shift in optical properties, the particle absorbs and emits in the visible region. The shaded portion of the spectra indicates the overlapped region of the two spectra. It could be observed that there is considerable overlap between the two spectra, which is brought about by the wideness of the two peaks.

The broadness in the optical spectra has been attributed to the creation of defects in the system during the process of nanoscaling of the crystals as explained in the

previous chapter. The crucial role of this spectral overlap in the quenching phenomenon and the related benefits are explained later in this chapter. It could be primarily assessed that due to the nanodimension of the crystal and its associated structural defects, the particles are able to absorb their self emitted photons which may set off radical changes in its properties.

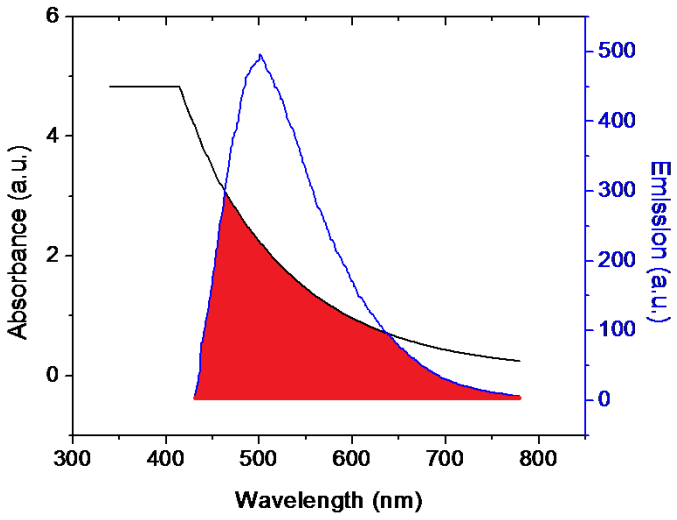

Fig. 3.1 Absorption and emission spectra of OANP plotted together; the shaded portion showing the spectral overlap.

The photoluminescence measurements of OANP dispersions at different concentrations have been provided in Fig. 3.2. It could be understood that the green emission of OANP shows a dependence on its concentration in the solvent. The nanoparticles show a normal trend of rise in PL intensity with increase in the amount of flourophores, up to a concentration ~0.6 mM, as implied in Fig. 3.2(a). But as the concentration exceeds this limiting value, the emission began to quench upon the addition of more amount OANP as shown in Fig. 3.2(b). The quenching effect was studied for concentration upto 0.0013 M.

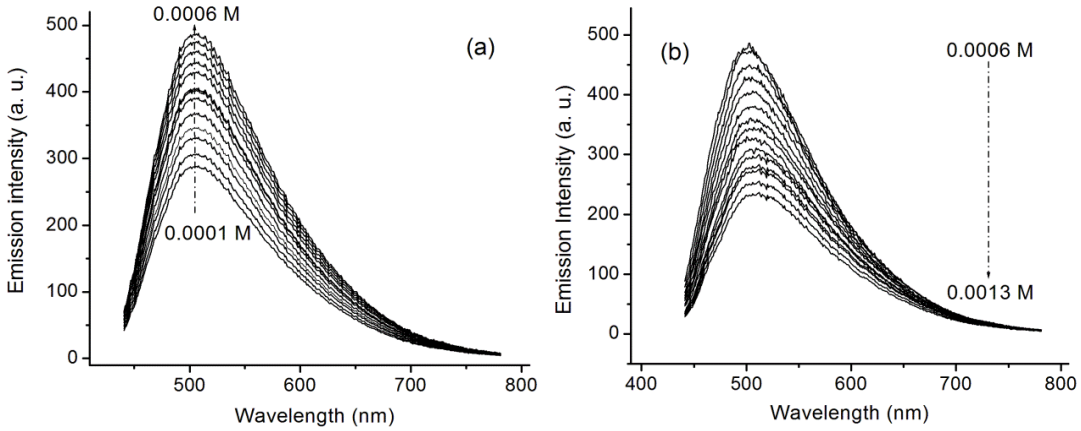

Fig. 3.2 PL spectra of the OANP dispersion at different concentrations (a) 0.0001–0.0006 M, and (b) 0.0006–0.0013 M.

The dependence of OANP concentration in the dispersion in general is shown in Fig. 3.3. It could be concluded from the figure that the size related green emission of OANP showed an initial rise in intensity with concentration which, after reaching a maximum intensity, seemed to decrease linearly, implying the possibility of an energy transfer triggered by the higher concentration of the dispersion which persuaded the particles to get rid of the absorbed photon *via* a mechanism other than radiative transfer.

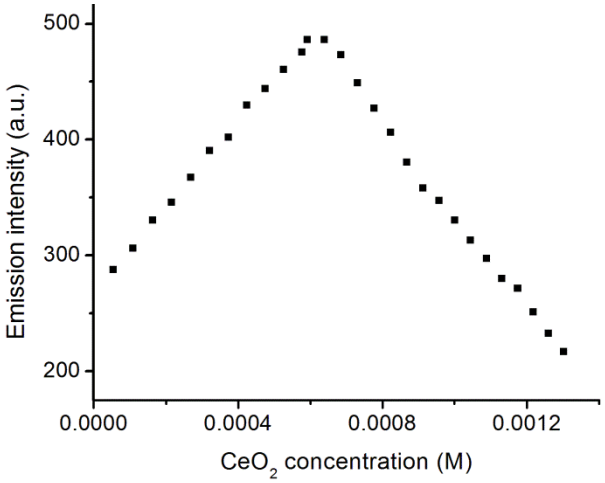

Fig. 3.3 Graph showing the variation of PL intensity with concentration of OANP.

3.4.2 Investigation of fluorescence quenching in OANP dispersions

As the PL spectra of the nanoparticle dispersion at variable concentration implies an initial hint towards the prevalence of fluorescence quenching at higher concentrations, a detailed investigation has been carried out on this regard. Fluorescence quenching is generally described by the Stern–Volmer equation (1)

$$\frac{I_0}{I} = 1 + K_{SV}[Q] \qquad (1)$$

where I_0 and I are the fluorescence intensity of fluorophore in the absence and presence of quencher respectively, [Q] indicates the concentration of quencher and K_{SV} is Stern-Volmer quenching constant.[50]

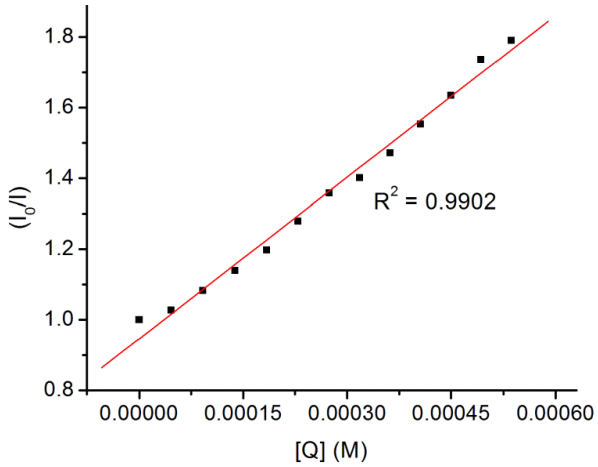

Fig. 3.4 Stern–Volmer plot for the concentration quenching of the dispersions.

As there is no external quencher in the present system, the Stern-Volmer equation has been modified and I_0/I has been plotted against [Q] as shown as Fig. 3.4. Here I_0 is the maximum emission intensity of the parent dispersion whose concentration does not fall in the quenching range (0.000639 M) and [Q] is the concentration of the dispersion added to a fixed volume of parent suspension. The variation in intensity against solid concentration is almost linear as indicated by near perfect linear regression with a R^2 value of 0.9902 which indicates effective quenching.

Also in order to understand the behaviour of the exciton in its higher energy state at variable concentrations, their life time has been measured by at two different concentration of the dispersion. The measured life time of the excited state in dispersion at concentrations 0.000868 and 0.0013 M yielded different values, 10 and 3 ns respectively as depicted by Fig. 3.5. The emission intensity can be related to

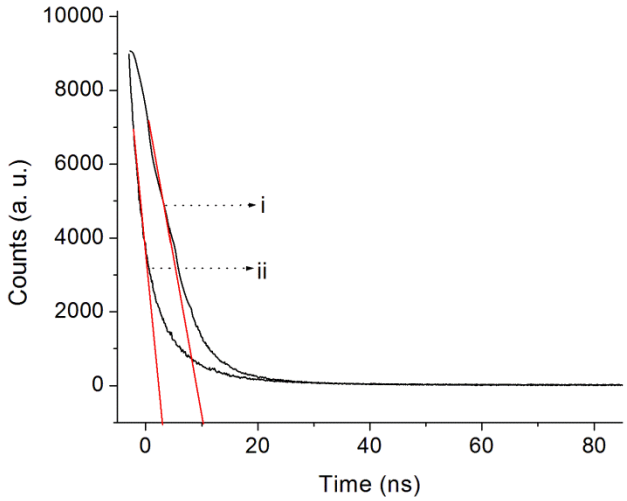

Fig. 3.5 Fluorescence lifetime measured for OANP dispersions at concentrations (i) 0.000868 M and (ii) 0.0013 M.

lifetime according to the equation $I = A\ e^{-(E/kt)}$, where A is a constant, k is the decay constant and t is the life time.[51] Accordingly, the life time of the exciton has an inverse relation with the emission intensity. The lesser span of the flourophore in the excited state, the lesser the emission intensity. The increased concentration of the particles might have paved way to the occurrence of an easy non-radiative energy relaxation path way for the particles and as a result they instantly disposes the energy within seconds leading to a lesser time of their stay in the excited state. Consequently, any observable radiative emission will be absent in the system causing the quenching of the fluorescence. As at higher concentrations, the particles are nearer to each other, any phenomenon related to their closeness has to be taken into account and further studied in detail.

3.4.3 Quenching mechanism based on FRET

Many mechanisms like complex formation, collisional processes and other energy transfer methods have been proposed so far for the quenching effects.[14,52] As in the present system, the nanoparticles are sterically well spaced by bulky oleic acid groups, the former two mechanisms can be ruled out. Moreover, the fast fluorescence decays for concentrated dispersions within the first 3 ns is a clear signature of non-radiative energy transfer.[53] The absorbance and emission spectra of the nanoparticles shows considerable spectral overlap indicated by the shaded region in Fig. 3.1 which index towards a mechanism based on FRET for the quenching effects. As FRET is a distance dependent energy transfer process in which energy is transferred from an excited donor to an acceptor molecule through a dipole-dipole interaction, an efficient energy transfer by FRET demands certain conditions to be satisfied like (i) the spectral overlap of donor emission and acceptor absorbance spectra, (ii) a desirable distance between the donor and acceptor, and (iii) possibility of dipole-dipole interaction.[12,13,16,54,55]

The significance of spectral overlap lies in the fact that a ground state acceptor could be energetically transferred to a higher level on the expense of an excited donor. This is because the absorption spectra of the acceptor extend to wavelengths corresponding to the emission spectra of the donor, which makes it capable of absorbing the emitted energy of the donor. Fig. 3.1 depicts that there is a considerable spectral overlap between absorption and emission of nanoparticles from about 450 to 750 nm. The absorption shoulder (λ_{max}) is at ~400 nm and the maximum emission peak is at ~510 nm. Both the spectra were fairly broad which extends over almost the whole visible range. It is noteworthy that the effective overlap of the spectra has been brought into reality by this extensive spreadness over the whole wavelength under

consideration. As the spectral broadening had originated from the defects associated with the miniaturisation of the crystals, the root of quenching effect lies on the nano dimension of the system.[56] So in the present system, the optical spectra of the nanoparticles entail that the particles are able absorb their own emitted photons thus favouring the energy transfer between themselves through a FRET mechanism.

As pointed out earlier, the energy transfer by FRET is accomplished through a dipole–dipole interaction between the transition dipole moments of the acceptor and donor.[16] Therefore, the detailed investigation of the interaction between nanoparticles during emission cannot be evicted.

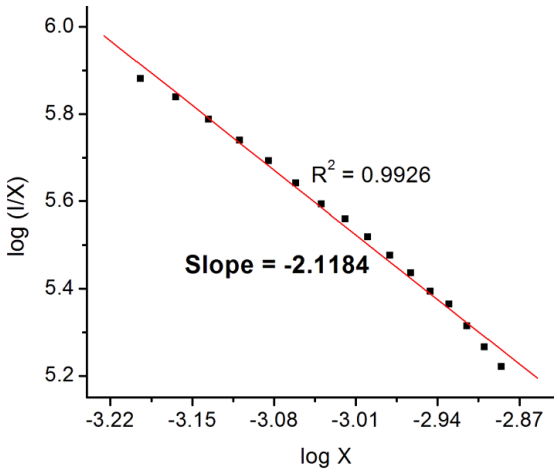

Fig. 3.6 Plot of log (I/X) against log X fitted linearly to show a dipole – dipole interaction among the particles.

The alignment of dipole moment in cerium dioxide is a prevailed phenomenon owing to the difference in electronegativity between cerium and oxygen. Therefore, the interaction of crystals on account of the dipole moment is highly probable in ceria. In fact, there are many reports which support the existence of dipole–dipole interaction in ceria during the course of investigation of crystal growth and morphology evolution.[57,58] The dipole-dipole interaction among molecules can be better evaluated on the basis of Dexter's theory on energy transfer. Accordingly, the

source of interaction between the flourophores, which resulted in concentration quenching, can be estimated using the equation (2)

$$\frac{I}{X} = \frac{K}{[1+\beta(X)^{Q/3}]} \quad (2)$$

in which I/*X* is the emission intensity per quencher concentration, *Q* is the exchange interaction whereas *K* and *β* are constants for a given lattice.[59] The value of *Q* is the significant factor which reveals the type of interaction. Q = 6, 8 or 10 for electric dipole–dipole (D–D), electric dipole–quadrupole (D–Q), or electric quadrupole–quadrupole (Q–Q) interactions respectively. The slope of the linear fit of the log (I/*X*) versus log *X* plot gives the value of *Q*. The *Q* value calculated for the present system from Fig. 3.6 is 6.36 (slope = -2.12, Q = -3 × slope) which is closer to 6 indicating a dipole-dipole interaction.[11,51] Thus in the present system, the interaction between the nanoparticles in the dispersion at higher concentrations *via* dipolar coupling has been well established using Dexter's theory.

The prerequisite of close proximity of the molecules in FRET limits the distance between donor and acceptor in the order of 100 Å owing to the dipole-dipole interaction.[55] Therefore, the calculation of distance between particles at variable concentrations of dispersion may provide vital information regarding the quenching mechanism. For distance estimation, we considered the Förster radius (R_0) which is the critical distance between the donor and acceptor at which the energy transfer rate is 50%. R_0 can be calculated according to the equation (3)

$$R_0 = \frac{7.35}{\left([A]_{1/2}\right)^{1/3}} \quad (3)$$

where $[A]_{1/2}$ is the half-quenching concentration, the concentration at which the maximum emission intensity is reduced to half.[60] Here the value of $[A]_{1/2}$ could be

estimated graphically by linear fitting the portion of the graph in Fig. 3.3, corresponding to the higher concentrations of dispersion (0.0001–0.0013 M) which shows quenching behaviour of photoluminescence.

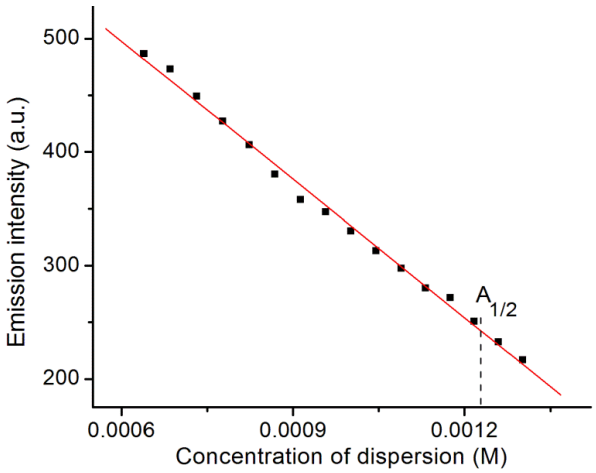

Fig. 3.7 The linear progression of PL intensity against concentration of OANP in the dispersion in the range 0.0006-0.0013, from which $[A]_{1/2}$ has been deducted.

The linear regression mentioned above has been supplied as Fig. 3.7 from which the value of $[A]_{1/2}$ has been estimated to be 0.001229 M. Using the calculated value of $[A]_{1/2}$, according to equation (3); R_0 was derived to be 68.6 Å.

According to Förster theory, the energy transfer rate at different distances can be calculated as

$$E = 1 - \frac{I}{I_0} \qquad (4)$$

using which the energy transfer rates of the dispersions at the concentrations under study can be deducted, provided the values of 'I and 'I_o' is known.[61] There is also another equation relating 'R_0' and 'E' which is given as equation (5)

$$E = \frac{R_0^6}{(R_0^6 + r^6)} \qquad (5)$$

where 'r' refers to the distance between the particles corresponding to the energy transfer rate.[61] Therefore, by knowing the PL intensity 'I' at a particular

concentration of dispersion and deducting the value of $[A]_{1/2}$ graphically, it is possible to theoretically estimate the distance between the particles corresponding to that concentration using equation (3), (4) and (5).

The values of '*r*' calculated at different concentrations by the above stated method were plotted against its corresponding concentration and is shown graphically in Fig.3.8. It could be observed from the figure that the distance calculated between particles for concentrations in the quenching range falls in the order of 100 Å which confirms the proposed quenching mechanism based on FRET.

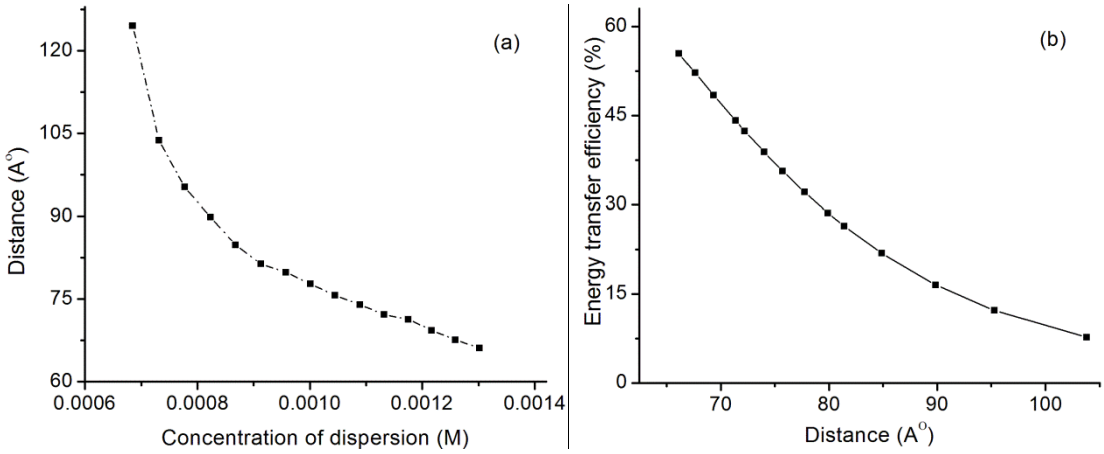

Fig. 3.8 (a) Variation of distance between particles with concentration of dispersion, and (b) the enhancement in energy transfer efficiency with a decrease in interparticle distance.

Also Fig. 3.8(b) shows the enhancement in energy transfer efficiency is deteriorating when the separation between particles increases. If energy transfer occurs *via* dipolar interaction, then the decreasing closeness of flourophores should depreciate the energy transfer rate. This is because dipole-dipole interaction has an inverse relation with distance between the dipoles and the similar effect was observed for OANP particles also. Thus, the information from Fig. 3.8(b) implies that the influence of distance between particles on energy transfer rate also index towards the

dipolar coupling between them, which underlines the existence of FRET based mechanism in the present system.

Overall, a mechanism based on FRET has been proposed which has been summarised in Scheme 3.2. Accordingly, in ceria dispersions at high nanoparticle concentrations, predominantly above 0.6 mM, the distance between the particles are confined in the order of Förster radius. Under such situation, the particles are able to communicate with each other *via* dipole-dipolar interaction leading to a non-radiative transfer of energy based on FRET.

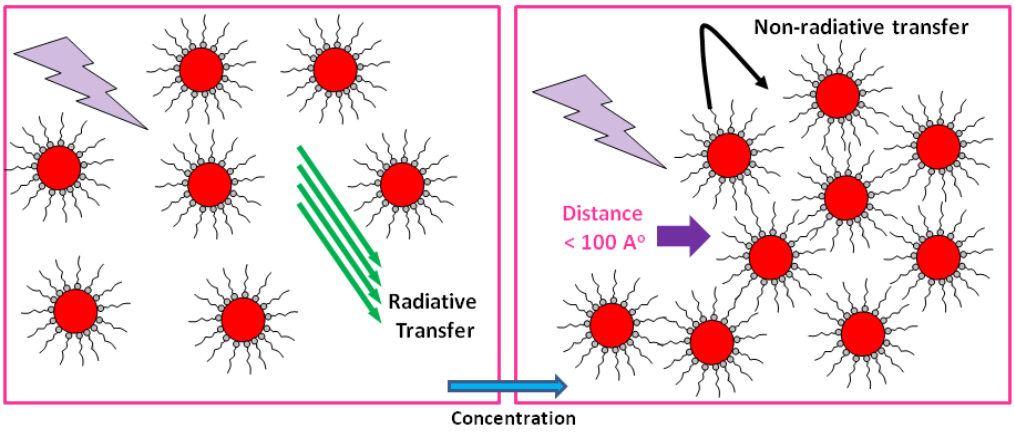

Scheme 3.2 Mechanism proposed based on FRET for the concentration quenching of ceria dispersions.

Considering the fact that the dipolar coupling is inversely proportional to the distance between the dipoles, as the particles becomes closer at higher concentrations, the dipoles are freed to interact more effectively. This leads to an amplified energy transfer rate between the particles, which eventually boosted the interparticle exciton transfer resulting in the absence of any radiative transfer from them. The quenching phenomenon was not observed for dilute dispersions probably because the distance between the particles under such dilute conditions may not be enough to couple with each other under the influence of dipolar force. Thus due to the absence of a proximal acceptor particle within the desired distance range of FRET, the particles are not able

to carry out the non-radiative transfer and ultimately they exhibit their normal property of emission in the visible region.

3.4.4 Effect of spacers on concentration quenching of OANP dispersion

As FRET is a quenching mechanism highly sensitive to distance between the flurophores, the presence of any moiety in the dispersion, capable of changing the distance between the particles can cause a divergence in quenching rate. The impact can be visualised in the emission spectra of the corresponding dispersion.

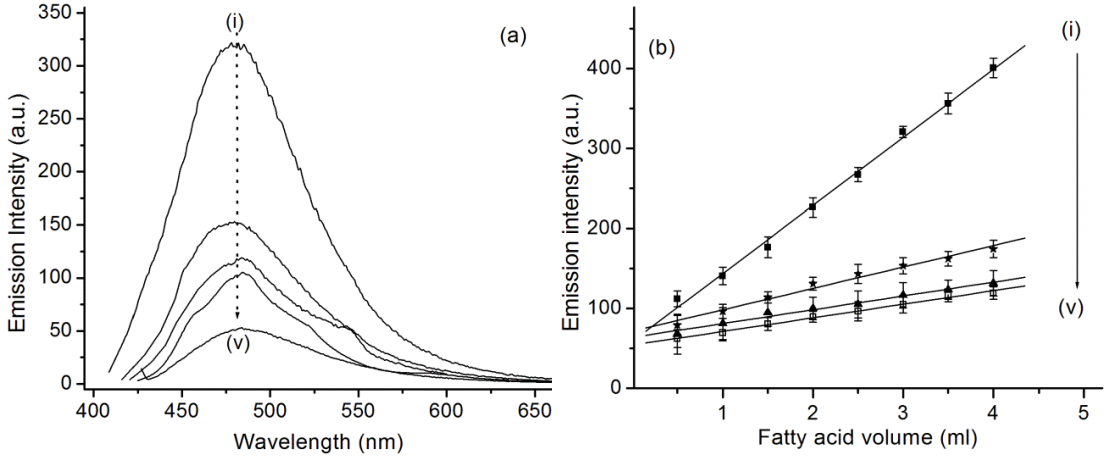

Fig. 3.9 (a) Emission spectra of OANP dispersion, after the addition 3.5 ml of different spacers: (i) oleic acid, (ii) decanoic acid, (iii) lauric acid, (iv) stearic acid and (v) parent dispersion without addition of spacer, and (b) the variation in emission intensity of parent dispersion with increase in the added volume of the spacers.

As the structure of the interfering moiety can influence the distance created by them between the particles, the study of PL intensity of the dispersion in their presence can perform as the source of structural identification of the moiety. In the present study, such a moiety which may come in between the particles other than solvent is denoted as a 'spacer'. Fatty acids differing in chain length as well as structure have been employed as spacers to vary the distance between the particles in the dispersions. The PL spectra of OANP dispersion after the addition of different fatty acids (3.5 ml) as illustrated in the experimental section is shown in Fig. 3.9(a). All the fatty acids

accomplished an enhanced emission with respect to the parent dispersion as shown in the figure. Also, whereas oleic acid gave the maximum intense spectra, the emission intensity showed an inverse relation with chain length for the rest. The trend in the PL enhancement by the spacers was consistent for their higher volumes of addition also. From Fig. 3.9(b), it could be inferred that even though there is an overall increase in PL intensity when the volume of spacers increased, the behaviour exhibited by the spacers in the dispersion was same. The surveillance implies that the presence of spacers somehow increases the FRET efficiency between the particles which has some dependence on the structure of the fatty acids.

Though the contribution of the spacer towards the overall dipole moment can enhance the energy transfer efficiency to a higher extent, it is least probable for the present system. This is because as electronic effects are not felt beyond three or four carbon, the difference in chain length alone is least expected to cause any marked influence on dipole moment.[62] Also the presence of double bond in the alkyl chain of oleic acid favours non-polar character in the chain which theoretically should in turn reduce dipolar coupling between particles, in contrast to the observed result.[63] Therefore, an improvement in emission bestowed by the spacers is likely due to the separation induced by them in between the particles.

The manner in which surfactant like molecules align in a medium strongly depends on certain parameters like chain length compatibility, chain cohesion, molecular interactions etc. which contributes to the intermolecular distance.[62] As chain length of fatty acid increases, the van der Waals interaction between the chains of adjacent molecules increases and *vice-versa* so that longer molecules are more attracted to each other.[62] In a medium, the extent of solvation solemnly depends on this attractive force and subsequently the intermolecular separation of the fatty acids

in the solvent is affected.[64] Longer fatty acids will be solvated less and subsequently they may be separated to each other to a less extent in the medium. For shorter fatty acids, as attractive interaction is weak, they will be solvated efficiently and so are farther to each other in the dispersion. So, long chain fatty acids create a shorter distance between the particles whereas shorter ones make the particles move far apart.

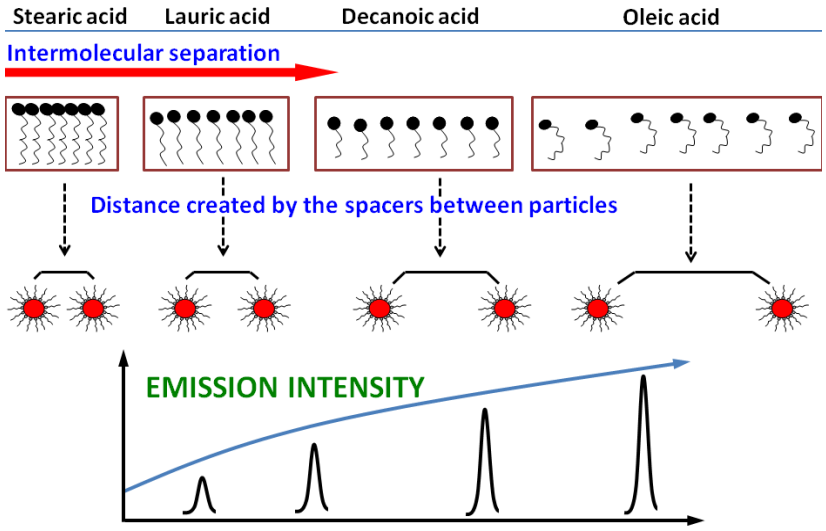

Scheme 3.3 Depiction of enhancement in emission intensity provided by the spacers by altering the distance between particles.

For oleic acid, this intermolecular attraction is again weak due to the kink induced by the cis-bond at the C9 position.[64] The bend in its structure prevents the closeness of the molecule with each other. Therefore, due to its inefficiency to remain closely packed as its straight chain colleagues, solvent could well separate these molecules. So due to their particular structure, oleic acid generated the highest separation between the particles among all the spacers under study.

Overall, the distance created by the spacers between the nanoparticles will be highly influenced by this intermolecular attraction in the dispersion which in turn depends on their structures. The order of enhancement provided by the spacers and the proposed mechanism has been depicted in Scheme 3.3.

The subsequent improvement in PL intensity with the volume of the spacers is obviously because particles are farther away on account of the additional spacer molecules present in between them. For validating the conjecture mentioned above, the distance created between the particles upon the addition of 3.5 ml of the spacers has been calculated using equation (3), (4) and (5) with the corresponding PL intensity rendered by each of them as input and is shown in Fig. 3.10.

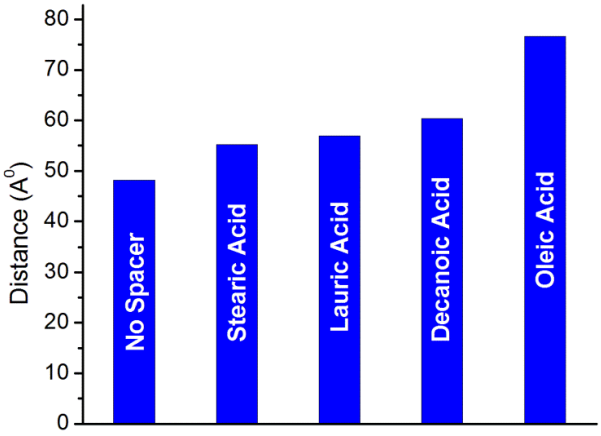

Fig. 3.10 The calculated distance between the OANP in its dispersion of concentration 0.0018 M, in the presence of different spacers.

The variation in the distance between the particles in the presence of spacers is in the order of the respective enhancement in PL intensity brought about by them, which substantiates the proposed rationale based on the structure of spacer. Thus it could be assessed that the structure of fatty acids indisputably influenced the separation induced by them between the particles which controlled the energy transfer efficiency and as a result the PL emission has become a function of their respective configuration. In short, each spacer will leave its own signature in the emission spectra depending upon its structure and chain length which may be useful as an analytical tool to identify the fatty acid.

Considering the importance of fatty acids in food industry as well as their major role in biological metabolic pathways, their analysis remains as a remarkable element of analytical chemistry.[46] The most commonly used method for their identification involves the analysis of their volatile and stable methyl ester derivatives using different techniques like Chromatography, Mass spectroscopy etc.[45,49] Also they have been identified by deducting the amount of carbon, hydrogen and oxygen atoms along with the number of double bonds present in them by chemical methods.[42] It could be noted that all these methods are time consuming as well as tedious involving complex chemical methods and sampling procedures. In that view, the proposed method is highly flexible for its practical adaptation as a simple and precise analytical tool for the identification of various fatty acids.

3.5 Conclusions

A spectroscopic investigation of the concentration quenching behaviour of ceria nanoparticles in dispersion have been carried out. The particles exhibited a linear Stern-Volmer characteristic and the inter particle dipole interaction has been established by graphical interrogation. The distance calculated between particles according to Förster theory falls within the FRET limits which along with other theoretical explorations projected a mechanism based on Förster resonance for the transfer of electronic excitations. The hypersensitivity of FRET to distance ultimately served as a yardstick to distinguish different fatty acids based on their structure and conformation. The present study supplies a model for the structural elucidation of molecules by means of a simple analytical approach.

3.6 References

1 D. Bera, L. Qian, T.-K. Tseng and P. H. Holloway, *Materials*, 2010, **3**, 2260-2345.

2 E. Jang, S. Jun, H. Jang, J. Llim, B. Kim and Y. Kim, *Adv. Mater.*, 2010, **22**, 3076-3080.

3 T. J. Brunner, P. Wick, M. Manser, P. Spohn, R. N. Grass, L. K. Limbach, A. Bruinink and W. J. Stark, *Environ. Sci. Technol.*, 2006, **40**, 4374-4381.

4 C. L. Chai, S. Y. Yang, Z. K. Liu, M. Y. Liao and N. F. Chen, *Chinese Sci. Bull.*, 2003, **48**, 1198-1200.

5 H. Gu and M. D. Soucek, *Chem. Mater.*, 2007, **19**, 1103-1110.

6 S. Maensiri, C. Masingboon, P. Laokul, W. Jareonboon, V. Promarak, P. L. Anderson and S. Seraphin, *Cryst. Growth Des.*, 2007, **7**, 950-955.

7 J. Zhang, S. Ohara, M. Umetsu, T. Naka, Y. Hatakeyama and T. Adschiri, *Adv. Mater.*, 2007, **19**, 203-306.

8 W. Shen, J. Jiang, C. Ni, Z. Voras, T. P. Beebe, Jr. and J. L. Hertz, *Solid State Ionics*, 2014, **255**, 13-20.

9 A. H. Morshed, M. E. Moussa, S. M. Bedair, R. Leonard, S. X. Liu and N. ElMasry, *Appl. Phys. Lett.*, 1997, **70**, 1647-1649.

10 S. H. Yu, H. Colfen and A. Fischer, *Colloid Surf. A*, 2004, **243**, 49-52.

11 W. Z. Lv, Y. C. Jia, Q. Zhao, M. M. Jiao, B. Q. Shao, W. Lu and H. P. You, *RSC Adv.*, 2014, **4**, 7588-7593.

12 N.T. Chen, S.-H. Cheng, C. P. Liu, J. S. Souris, C.-T. Chen, C.-Y. Mou and L.W. Lo, *Int. J. Mol. Sci.*, 2012, **13**, 16598-16623.

13 P. C. Ray, G. K. Darbha, A. Ray, J. Walker and W. Hardy, *Plasmonics*, 2007, **2**, 173-183.

14 M. Szabelski, D. Ilijev, P. Sarkar, R. Luchowski, Z. Gryczynski, P. Kapusta, R. Erdmann and I. Gryczynski, *Appl. Spectrosc.*, 2009, **63**, 363-368.

15 C. S. Yun, A. Javier, T. Jennings, M. Fisher, S. Hira, S. Peterson, B. Hopkins, N. O. Reich and G. F. Strouse, *J. Am. Chem. Soc*, 2005, **127**, 3115-3119.

16 Y. H. Park, Y. Kim, H. Sohn and K. S. An, *J. Phys. Org. Chem.*, 2011, **25**, 207-210.

17 J. Shi, F. Tian, J. Lyu and M. Yang, *J. Mater. Chem. B*, 2015, **3**, 6989-7005.

18 G. Chen, F. Song, X. Xiong and X. Peng, *Ind. Eng. Chem. Res.*, 2013, **52**, 11228-11245.

19 G. Cario and J. Franck, *ZPhys-e.A: Hadrons Nucl.*, 1922, **11**, 161-166.

20 J. Franck, *ZPhys-e.A: Hadrons Nucl.*, 1922, **9**, 259–266.

21 F. Perrin, *Ann. Phys. Paris*, 1932, **12**, 283-314.

22 H. Kallmann and F. London, *Z. Phys. Chem.*, 1928, **B2**, 207–243.

23 R. Hein and R. Y. Tsien, *Current Biol.*, 1996, **6**, 178-182.

24 D. Geissler, S. Linden, K. Liermann, K. D. Wegner, L. J. Charbonniere and N. Hildebrandt, *Inorg. Chem.*, 2014, **53**, 1824-1838.

25 K. Boeneman, B. C. Mei, A. M. Dennis, G. Bao, J. R. Deschamps, H. Mattoussi and I. L. Medintz, *J. Am. Chem. Soc.*, 2009, **131**, 3828-3835.

26 Y. Choi, J. Lee, K. Kim, H. Kim, P. Sommer and R. Song, *Chem. Commun.*, 2010, **46**, 9146-9148.

27 Y. P. Kim, Y. H. Oh, E. Oh, S. Ko, M. K. Han and H. S. Kim, *Anal. Chem.*, 2008, **80**, 4634-4641.

28 Y. P. Kim, Y.-H. Oh, E. Oh and H.-S. Kim, *Biochip J.*, 2007, **1**, 228-233.

29 R. H. Kimura, E. R. Steenblock and J. A. Camarero, *Anal. Biochem.*, 2007, **369**, 60-70.

30 K. A. Krukenberg, T. O. Street, L. A. Lavery and D. A. Agard, *Q. Rev. Biophys.*, 2011, **44**, 229-255.

31 T. Krusinski, A. Ozyhar and P. Dobryszycki, *Nucl. Acids Res.*, 2010, **38**, 11.

32 C. A. Mirkin, R. L. Letsinger, R. C. Mucic and J. J. Storhoff, *Nature*, 1996, **382**, 607-609.

33 C. Liu, Z. Wang, H. Jia and Z. Li, *Chem. Commun.*, 2011, **47**, 4661–4663.

34 Y. Piao, F. Liu, T. S. Seo and . *Chem. Commun.*, 2011, **47**, 12149–12151.

35 B. Tang, L. Cao, K. Xu, L. Zhuo, J. Ge, Q. Li and L. Yu, *Chem. Eur. J.*, 2008, **14**, 3637–3644.

36 B. Dubertret, M. Calame and A. J. Libchaber, *Nat. Biotechnol.*, 2001, **19**, 365–370.

37 D. Gao, Z. Wang, B. Liu, L. Ni and Z. Zhang, *Anal. Chem.*, 2006, **80**, 8545−8553.

38 F. May, M. Peter, A. Hutten, L. Prodi and J. Mattay, *Chemistry*, 2012, **18 (3)**, 814−821.

39 M. Wang, W. Hou, C. C. Mi, W. X. Wang, Z. R. Xu, H. H. Teng and S. K. Xu, *Anal. Chem.*, 2009, **81**, 8783−8789.

40 Y. P. Ho, H. H. Chen, K. W. Leong and T.-H. Wang, *J. Controlled Release*, 2006, **116**, 83-89.

41 J. Lee, Y. Choi, J. Kim, E. Park and R. Song, *Chemphyschem*, 2009, **10**, 806-811.

42 H. C. Black, *Fatty acids for chemical specialties*, 1955, The Bon Ami Company, Newyork.

43 G. D. Lopaschuk, J. R. Ussher, C. D. L. Folmes, J. S. Jaswal and W. C. Stanley, *Physiol. reviews*, 2010, **90**, 207-258.

44 P. M. Kris-Etherton, W. S. Harris and L. J. Appel, *Circulation*, 2002, **106**, 2747-2757.

45 W. Yang, J. Adamec and F. E. Regnier, *Anal. Chem.*, 2007, **79**, 5150-5157.

46 R. M. Tucker, R. D. Mattes and C. A. Running, *Int. Biochem. Mol. Bio.*, 2014, **40**, 313–326.

47 R. L. Glass, *Lipids*, 1971, **6**, 919-925.

48 S. A. Mjos, *Eur. J. Lipid Sci. Technol.*, 2004, **106**, 550–560.

49 S. Zhang, J. Liu, Y. Chen, S. Xiong, G. Wang, J. Chen and G. Yang, *J. Am. Soc. Mass. Spectrum* 2010, **21**, 154–160.

50 M. Amjadi and L. Farzampour, *Luminescence*, 2013, **29**, 689-694.

51 X. G. Zhang, J. L. Zhang, Z. Y. Dong, J. X. Shi and M. L. Gong, *J. Lumin.*, 2012, **132**, 914-918.

52 U. Anand, C. Jash, R. K. Boddepalli, A. Shrivastava and S. Mukherjee, *J. Phys. Chem. B*, 2011, **115**, 6312-6320.

53 R. Koole, P. Liljeroth, C. D. Donega, D. Vanmaekelbergh and A. Meijerink, *J. Am. Chem. Soc.*, 2007, **129**, 10613-10613.

54 S. Xu, S. Xu, Y. Zhu, W. Xu, P. Zhou, C. Zhou, B. Dong and H. Song, *Nanoscale*, 2014, **6**, 12573-12579.

55 J. Zhang, B. Li, L. Zhang and H. Jiang, *Chem. Commun.*, 2012, **48**, 4860-4862.

56 A. Ahniyaz, Y. Sakamoto and L. Bergstrom, *Cryst. Growth Des.*, 2008, **8**, 1798-1800.

57 N. Du, H. Zhang, B. Chen, X. Ma and D. Yang, *J. Phys. Chem. C*, 2007, **111**, 12677-12680.

58 Y. Li and W. Shen, *Chem. Soc. Rev.*, 2014, **43**, 1543-1574.

59 D. L. Monika, H. Nagabhushana, R. H. Krishna, B. M. Nagabhushana, S. C. Sharma and T. Thomas, *RSC Adv.*, 2014, **4**, 38655-38662.

60 G. A. Kumar and N. V. Unnikrishnan, *J. Photochem. Photobiol., A*, 2001, **144**, 107-117.

61 E. Gokoglu and E. Yilmaz, *J Fluoresc.*, 2014, **24**, 1439-1445.

62 J. R. Kanicky and D. O. Shah, *J. Colloid Interf. Sci.*, 2002, **256**, 201-207.

63 I. M. El-Anwar and S. A. El-Henawii, *J. Mater. Sci. Technol.*, 1998, **14**, 361-367.

64 R. Tadmor, R. E. Rosensweig, J. Frey and J. Klein, *Langmuir*, 2000, **16**, 9117-9120.

CHAPTER 4

Bilayer Surface Functionalisation of Cerium oxide nanoparticles and its realistic perspective as a 'turn–on' fluorescent sensor for Vitamin C

4.1 Abstract

The distinct overview of cerium dioxide as a fluorescent sensor has been demonstrated in the present chapter. The principle of the sensor is based on the redox property of ceria and its dependence on the fluorescence in association with its nano dimension.

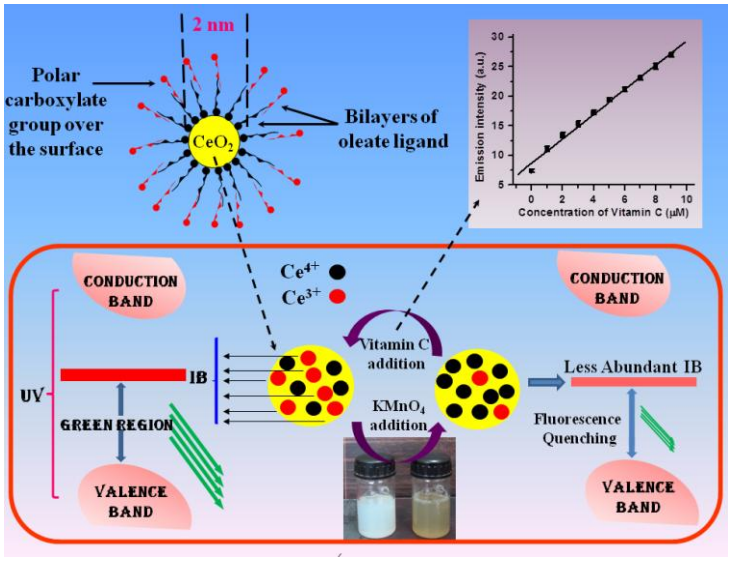

Monolayer surfactant coated ultra fine ceria nanoparticles of average size 2.2 nm have been fabricated by a surfactant assisted thermal decomposition strategy. The particular fashion of attachment of the surfactant, oleic acid with ceria resulted in the surface hydrophobicity of the nanoparticle which in turn prevents its interaction with a hydrophilic molecule like vitamin C in the reaction media. In order to tackle the incompatibility of the nanoparticles with water, a hydrophilic surfactant coating has been grafted over its surface *via* a technique based on bilayer surface functionalisation. The success in the accomplished scheme has been confirmed by

thermogravimetric analyses, zeta potential and contact angle measurements. Detailed spectroscopic investigation revealed that, while the addition of bilayer surfactant over the nanoparticle surface rendered it hydrophilic, it preserved all the properties of the inner nanoparticles core as such. The redox property of ceria and its influence on the optical properties served as a yardstick to quantify vitamin C in the concentration range 10^{-7}–10^{-4} M with a much lower value of the limit of detection (LoD) of 500 nM. The designed sensor exhibits a rapid 'turn on' fluorescence response within 30 s and the reversibility of fluorescence even after 5 cycles of vitamin C addition corroborates its reusability. The high selectivity of the method to detect vitamin C again point up its suitable candidature as an analytical tool. The realistic application of the sensor has also been displayed by the quantification of vitamin C in pharmaceutical formulations within agreeable error limits.

4.2 Introduction

In the light of recent advances in science and technology, there is an urge to discover innovative materials as well as to ameliorate existing functionalities capable of imparting a scientific revolution. In this aspect, exploring the obscured applications of current materials beyond their conventional uses is a hot topic of current research. As discussed in the first chapter, ceria has been traditionally exploited as an automobile exhaust catalyst, in solid oxide fuel cells (SOFC), as an oxygen gas sensor, in oxygen permeation membrane systems, as catalysts for reactions involving oxidation etc., owing to their unique redox property.[1-4] Also due to the strong absorption in the UV region, ceria has been used as an additive in sun screen lotions and the inherent hardness of ceria make it a good abrasive.[5]

In the 21st century, some of the researches based on ceria presented a different outlook of the material, which served as a footstep towards its uncustomary applications. In 2004, ceria based hierarchical mesoporous structure fabricated by Corma *et al.* exhibited linear photovoltaic response, offering its candidature as a photoactive semiconductor for the construction of solar–cells.[6] Ceria has been experimented as a sorbent material by Stephanopoulos *et al.* in 2006 for the regenerative adsorption and removal of H_2S from hot fuel gas streams.[7] The biological application of this rare-earth oxide sprouted around 2005 with some groundbreaking studies, which presented the antioxidant activity of nanoceria in cell culture models. In 2005, Seal *et al.* digged out the ability of vacancy engineered ceria nanoparticles to confer protection from radiation induced cellular damage selectively to normal human breast cell line.[8] Another pioneer work involving the biological application of ceria was carried out by Mcginnis *et al.* on the control of retinal

degeneration by the particles, on account of its ability to scavenge reactive oxygen intermediates, which was broadcasted by the 'Nature publishing group' in 'Nature Nanotechnology' in 2006.[9] In 2007, Patil *et al.* designed ceria as a drug delivery device for releasing Human carbonic anhydrase (hCAII) inhibitors which are capable of controlling glaucoma, a medical condition causing blindness.[10] Besides, ceria has also been explored as a humidity sensor[11] as well as a sensing tool for the determination of a variety of chemical moieties including tramadol, histamine, carbonic acid, methyl orange, sulphur dioxide etc.[12-16] With reference to recent literatures on ceria, it could be accounted that efforts are still in progress to unveil the concealed aspects of ceria so as to widen its technological and commercial importance.

In the present chapter, ceria had been designed as a fluorescent sensing probe for the detection of vitamin C, based on the size induced green emission and its dependence on the Ce^{3+} content.

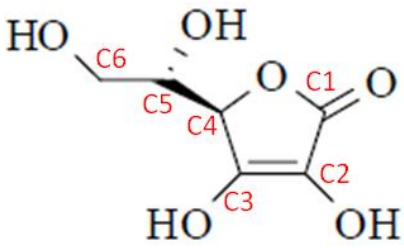

Scheme 4.1 Schematic representation of the structure of vitamin C.

Vitamin C or L-Ascorbic acid is a biologically imperative molecule assigned with multifunctional roles in human beings like metabolism, neurotransmission, nutrition, immunisation, electron transport, wound healing etc.[17-19] It is a weak sugar acid, structurally related to glucose, consisting of a five membered lactone ring as shown in Scheme 4.1. The presence of electron rich C2, C3-enediol moiety in the

molecule makes it a member of redox system having both electron donating and electron accepting properties. The other two hydroxyl groups attached to C5 and C6 behave as alcoholic groups.[20]

Vitamin C can easily be oxidised by several agents, especially in aqueous solutions, to form dehydroascorbic acid (DHAA) and this reversible reaction is the basis for most of its known biological functions.[21] Human body is not able to synthesis vitamin C and consequently it has to be provided externally through diet, unless, its deficiency causes serious disorders like scurvy, gingival bleeding etc.[18] The minimum amount of 10 mg/day is required for human beings to prevent scurvy. Due to its medical relevance, there have been plenty pharmaceutical supplements for vitamin C. The oxidation of ascorbic acid is greatly favoured by the presence of oxygen, heavy metals and alkaline pH and as it is prone to easy degradation[22] in the presence of heat and light, accurate quantification of these molecules in their supplements is vital to assure the quality. Many analytical techniques have been developed so far towards this goal, each of them having their own flaws and faults.[19,23,24]

One of the oldest and traditionally used methods for the quantification of vitamin C involves its titration with an oxidising agent.[25] In 1928, Tillmans *et al.* introduced oxidometric titration for the analysis of vitamin C by making use of 2,6-dichlorophenolindophenol (DCIP), whose characteristics seemed to be identical with that of the vitamin.[26] Later the method was modified by different research groups including that of Ray's and King's.[27,28] The oxidometric method of analysis of vitamin C commonly involves iodometric or DCIP titration, which was one of the official methods of analysis of vitamin C according to the Association of Official

Analytical Chemists (AOAC).[29] In 1935, Tauber and Kleiner proposed an enzymatic method for the determination of vitamin C involving the enzyme ascorbic acid oxidase, which could specifically bind with the vitamin.[30] In 1942, Roe and Kuether, developed a spectrophotometric method based on the colour reaction between 2,4-dinitrophenylhydrazixe derivative of dehydroascorbic acid with sulphuric acid.[31] Meanwhile, Mapson and Partridge in 1949 showed that ascorbic acid can be separated on a paper chromatogram using different mixtures of solvents like *n*-butanol, acetic acid, water and phenol, which marked the beginning of using chromatographic technique for the estimation of vitamin C.[32] In 1964, a fluorometric method was put forward by Deutsch and Weeks based on the condensation reaction between o-phenylenediamine and dehydroascorbic acid to form a fluorescent quinoxaline derivative.[33] Although all these methods are capable of providing a precise and accurate estimation of vitamin C, the related drawbacks cannot be disregarded when the ultimate goal of an ideal method is being considered. Due to the lack of specificity to vitamin C, some of these methods are inappropriate in the presence of other reducing agents.[34] Some methods display drawbacks in terms of cost effectiveness.[19] The crucial weakness of all these methods is the inability to quantify vitamin C at low analyte concentration[35], thus restricting its execution in pharmaceutical and food industry as well as its biological evaluation which entails trace analysis. In the early 1970s, a new technique based on electrochemical oxidation of vitamin C has emerged, which later flourished as an important method for its quantification. In 1972, Mason *et al.* estimated vitamin C in pharmaceutical formulations based on its oxidation on tubular carbon.[36] Domniguez *et al.* and Rizz *et al.* reported the electro chemical analysis of vitamin C using mercury drop electrodes in 1976 and 1977 respectively.[37,38] Since its implementation, great

attention has been paid to electrochemical method owing to the potential of sensing at low analyte concentration and wide dynamic range of detection offered by this method.[39] Due to its advantages and ability to sense vitamin C in ultra dilute conditions even in nanomolar range[40], electrochemical analysis is one of the prominent techniques in the present scenario. The technique is in its way of progress by experimenting different methods of detection like voltammetry, amperometry, coloumetry etc as well as by varying the electrode materials.[19,23,24] But similar to other methods, the electrochemical method is also not free of flaws. The major drawback of this method is the high overpotential which creates the fouling occurred by the adsorption of the oxidation products on the electrode surface and thus decreases the reproducibility and sensitivity of the electrode.[18] Additionally, the procedure demands expensive equipments and trained operators, inviting a second thought on its commercial implementation.

On the background of high industrial demand for an appropriate analytical system capable of fast, sensitive, selective, accurate, miniaturisable and low-cost assessment of vitamin C at analyte concentration as low as possible, research is still ongoing to meet the requirements for devising an ideal commercial sensor . The numerous research articles on vitamin C sensing in recent years rationalise the above statement. Some of the recent advances in vitamin C sensing have been tabulated in Table 4.1.

Table 4.1 Overview of recent advances in vitamin C sensing, presented in the ascending order of the limit of detection of the corresponding method

Method	Material	Dynamic Range of detection	Limit of detection (LoD)	Year	Ref. No.
Voltammetry	Melamine/ chlorani imprinted polymer	10^{-9} to 10^{-4}	1.4×10^{-9}	2009	[40]
Voltammetry	C nanotube/C electrode	10^{-8} to 10^{-5}	1.0×10^{-8}	2013	[41]
Voltammetry	Nano ZnO/poly(luminol) hybrid film	10^{-6} to 10^{-4}	1.0×10^{-6}	2009	[42]
Colorimetry	Au nanorods	10^{-7} to 10^{-4}	1.9×10^{-8}	2013	[43]
Voltammetry	C nanotubes	10^{-7} to 10^{-4}	8.0×10^{-8}	2015	[44]
Voltammetry	C paste / C nanotubes and 5-amino-2′-ethyl-biphenyl-2-ol electrode	10^{-7} to 10^{-4}	1.0×10^{-7}	2013	[23]
Flourimetry	Ag nanoparticles	10^{-6} to 10^{-4}	1.0×10^{-7}	2009	[45]
Flourimetry	$CePO_4$ nanorods	10^{-6} to 10^{-5}	1.1×10^{-7}	2010	[46]
Voltammetry	Poly(sulfonazo III)/glassy C electrode	10^{-7} to 10^{-3}	1.7×10^{-7}	2010	[47]
Voltammetry	TiO_2 nanoparticles/C electrode	10^{-6} to 10^{-3}	3.0×10^{-7}	2010	[48]
Amperometry	Polyaniline/glassy C electrode	10^{-7} to 10^{-3}	4.0×10^{-7}	2001	[34]
Spectro photometry	Prussian blue	10^{-6} to 10^{-5}	4.5×10^{-7}	2004	[49]
Spectro photometry	Polyaniline film	10^{-7} to 10^{-5}	6.0×10^{-7}	2005	[35]
Diffusion Layer Titration	Hypobromite	10^{-6} to 10^{-2}	1.0×10^{-6}	2001	[50]
Voltammetry	Au electrode	10^{-6} to 10^{-4}	1.7×10^{-6}	2010	[51]

Amperometry	C electrode /Au-Ag/chitosan matrix	10^{-6} to 10^{-3}	2.0×10^{-6}	2013	[52]
Potentiometry	PVC membrane	10^{-6} to 10^{-3}	2.0×10^{-6}	2004	[53]
Amperometry	Au/Ru nanoshells	10^{-6} to 10^{-3}	2.2×10^{-6}	2014	[54]
Potentiometry	Cu / poly(ethylene-co-vinyl acetate) matrix	10^{-6} to 10^{-4}	3.9×10^{-6}	1998	[55]
Voltammetry	Ni(II)complex / C nanotubes electrode	10^{-5} to 10^{-4}	4.0×10^{-6}	2013	[39]
TLC	Fe(III)/ immobilised 2,2'-dipyridyl (dipy)	10^{-4} to 10^{-3}	5.6×10^{-6}	2008	[21]
Potentiometry	Ni (II) Schiff bases	10^{-5} to 10^{-3}	7.3×10^{-6}	2010	[56]
Voltammetry	Ag nanoparticles/Graphene oxide	10^{-5} to 10^{-4}	9.6×10^{-6}	2013	[57]
Amperometry	Polypyrrole / C Nanotubes	10^{-5} to 10^{-3}	3.0×10^{-5}	2011	[58]
Spectro photometry	Prussian blue	10^{-4} to 10^{-2}	1.0×10^{-4}	1998	[59]
Voltammetry	DMF-exfoliated graphene	10^{-4} to 10^{-3}	1.2×10^{-4}	2010	[60]
Voltammetry	Tulium oxide	10^{-4} to 10^{-3}	4.2×10^{-4}	2013	[61]
Amperometry	Electrographted ortho aminophenol film	10^{-3} to 10^{-2}	8.6×10^{-4}	2008	[62]

The major challenge in implementing ceria as a sensor for an extremely water soluble molecule like vitamin C is its incompatibility with water. In the absence of any chemical modification, surface of ceria is hydrophobic due to their unique electronic structure which prevents it from hydrogen bonding with interfacial water.[63] The high surface energy of the nanoparticles in association with their enhanced surface to volume ratio again rattle the situation, as they tend to aggregate and settle in their aqueous dispersion. Therefore, the preparation of ceria based stable

aqueous dispersion is one of the critical concerns to be overcome, before tailoring it as a practical device in aqueous media. A careful inspection of literatures on ceria broaches different synthetic routes for achieving stable aqueous dispersion of ceria. Among these, while some methods demand expensive equipments and modifiers,[64] some others insist the pH of the dispersion in the acidic range.[65] Also the stringent synthetic conditions and multiple processing steps are the stumbling blocks for the practical adaptation of some methods.[64] In the present context, a facile two step synthetic strategy involving bilayer surface modification using a readily available and inexpensive fatty acid, oleic acid has been adopted to render surface of ceria nanoparticles hydrophilic.

The water dispersible nanoparticles retained its size dependent properties even after bilayer modification. The realistic perspective of the hydrophilic nanoparticles as a vitamin C sensor by modulating the Ce^{3+} content have also been demonstrated. To date, there is only one study exploring the capability of ceria for sensing vitamin C, thus justifying further research in this area. The study was conducted by Sharpe *et al.* and was based on the colorimetric change of ceria nanoparticle after interaction with antioxidants.[66] The assay could detect a group of antioxidant in food including vitamin C, but the detection range was 20 to 400 mM implying its limitation to sense the molecule in dilute conditions which is highly desirable for its pharmaceutical estimation. Moreover, certain issues like selectivity have not been addressed in the context, causing concern on its practical applicability. The highlight of the present method is the ease and efficiency to sense Vitamin C at a concentration as low as 6 µM with higher reproducibility, selectivity and rapidness. In short, the present chapter aims at projecting ceria as a novel 'turn-on' fluorescent sensor by making use of its redox property.

4. 3 Experimental

Cerium acetate (99.9%), the precursor used, ascorbic acid (99%), potassium permanganate (99%), citric acid anhydride (99%) and calcium carbonate (99%) were purchased from Merck (India), titanium dioxide (99%) was purchased from CDH Chemicals, India, D-glucose (>99.5%), diphenyl ether (99%) and oleyl amine (70%) were procured from Sigma Aldrich, oleic acid (90%) was obtained from Alfa Aesar (UK), ammonium hydroxide (25%, analytical grade) was bought from Qualigens Fine Chemicals, India. Common solvents such as acetone, cyclohexane and toluene (analytical grade) were procured from Merck, India. Branded pharmaceutical formulations as well as supplements of vitamin C in the form of tablets have been supplied by Glaxo Smithkline Pharmaceuticals Ltd., India and Wipro Care India, the amount of the vitamin in each tablet was 500 mg and 1 mg respectively. Water utilised during the synthesis procedure was acquired after double distillation using a quartz glass distillation unit.

4.3.1 Bilayer surface functionalisation of the oleophilic ceria nanoparticles.

Monolayer oleic acid coated ceria nanoparticles, OANP has been synthesised *via* a thermal decomposition strategy, as illustrated in the second chapter. In a typical synthesis, 4.8 g of cerium acetate (0.015 moles) was dissolved in 300 ml diphenyl ether in a round bottom flask. To this, 0.06 moles oleic acid (OA) and 0.069 moles oleylamine were added and the reaction mixture was refluxed at its natural boiling point (~260ºC) for 1 h. After cooling, acetone was added to precipitate the OA coated ceria nanoparticles. The precipitate was washed thoroughly with acetone and dried to obtain OANP.

OA was again employed as a secondary surfactant to provide a bilayer coating over OANP. About 1 g of OANP was combined with 20 ml of distilled water, which was almost immiscible, due to the hydrophobic nature of the surface. 20 ml of 10% (w/v) ammonium oleate in water was added drop-wise to this and stirred vigorously. Ammonium oleate was prepared by adding adequate amount of ammonium hydroxide to OA, so that the pH of the resultant solution is about 9, which is mandatory for the ionisation of the acid. After stirring the initial mixture of nanoparticle and oleate salt in water for about 3 h, mixture has been transformed into a stable suspension signifying the bilayer surface modification of oleate ions over the nanoparticle surface. The water in the suspension was allowed to evaporate slowly by providing a consistently boiling water bath as heat source. The nanoparticles obtained were washed thoroughly with cyclohexane, followed by acetone to remove any uncoated particles as well as unreacted oleate ions, which were later, dried and redispersed in water to yield a stable dispersion. The sample is named as BLNP henceforth.

The different synthetic parameters mentioned above in the bilayer modification process have been adopted after necessary optimisation of the experimental factors. The ratio of surfactant in the monolayer to that in the bilayer has been varied by experimenting different volumes of the added ammonium oleate, from 2 to 25 ml, which was finally optimised to 20 ml. Also the stirring time for the reaction has been optimised to 3 h, after the continuous observation of OANP in the reaction mixture to get fully dispersed in the aqueous media.

4.3.2 Preparation of ceria dispersions for sensing vitamin C under different concentrations

A parent dispersion of the nanoparticles in water has been prepared with a concentration of 0.0008 M, the photoluminescence spectra of which is recorded. To 2 ml of this dispersion, different volume (0.1 to 0.5 ml) of potassium permanganate solution (0.5 mM) was added and its photoluminescence was continuously monitored to optimise the volume of permanganate solution required to quench its fluorescence. A set of vitamin C solution in water at µM to mM concentration ranges have been prepared and 2 ml of each solution has been added to 2 ml of the ceria dispersion whose fluorescence has been quenched by the addition of permanganate. The quantitative estimation of vitamin C has been carried out by the acquisition of the photoluminescence spectra of the respective samples. For demonstrating the selectivity of the sensor towards vitamin C, different concentrations of common pharmaceutical ingredients such as citric acid, calcium hydroxide, glucose and titanium dioxide in water have been added to BLNP dispersion and the PL spectra of the same was acquired. The interference study has also been carried out by monitoring the PL spectra of BLNP with vitamin C in the presence of all ingredients.

4.3.3 Analysis of vitamin C in commercial pharmaceutical formulations

A solution of one tablet (tablet 1) in water was prepared, which was made up to 1000 ml in a standard flask. 1 ml aliquot was taken and again diluted to 1000 ml. 2 ml of this solution was added to 2 ml of the BLNP dispersion (0.0008 M) whose fluorescence has been quenched by the addition of permanganate and the PL intensity of the same has been monitored. Likewise for tablet 2, one tablet was dissolved in 1000 ml water and 2 ml of this solution was added to the fluorescence quenched

BLNP dispersion. The quantification was carried out by deriving the concentration of vitamin C corresponding to the respective PL intensity from the linear calibration plot and subsequently its concentration in the parent solution (in each tablet) has been calculated. The experiment was conducted in triplicate and the final value was represented in terms of Relative Standard Deviation (RSD) as tabulated in Table 4.3.

4.4 Results and discussion

4.4.1 Synthetic strategy involving bilayer surface functionalisation

The substrate for the bilayer functionalisation is OANP, the nanoparticles synthesised by thermal decomposition approach as described in the second chapter which possesses a monolayer of OA surfactant. The success in the monolayer capping is brought about by the chemisorption of oleate ligands over the positive nanoparticle core. The detailed mechanism behind the monolayer coating *via* a free radical intermediate formation has been already illustrated. The particular mode of attachment of oleate ion with the nanoparticle resulted in the protrusion of non-polar alkyl chain over the particle surface, thus inducing hydrophobicity on its surface. As the prepared nanoparticle dispersibility is limited to organic solvents, their incompatibility with water is in turn, a hurdle for applications intended on aqueous media. In order to make the particles attuned to hydrophilic surroundings, slight polarity has been induced over the surface of nanoparticles by oleic acid mediated bilayer surface encapsulation. The conceptual pathway of the synthetic strategy for bilayer functionalisation has been depicted in Scheme 4.2.

The long, non-polar alkyl chain of the oleate ion in the monolayer intertwines with that of the oleate ions which have been added during the bilayer surface modification process. This interlink has been effected by the hydrophobic-

hydrophobic interaction among the two alkyl chain[67] which ultimately resulted in the projection of the carboxylate group of the oleate ion over the nanoparticle surface. The polarity brought about by the C–O^- bond in the carboxylate ions reversed the characteristics of nanoparticle surface from hydrophobic to hydrophilic.

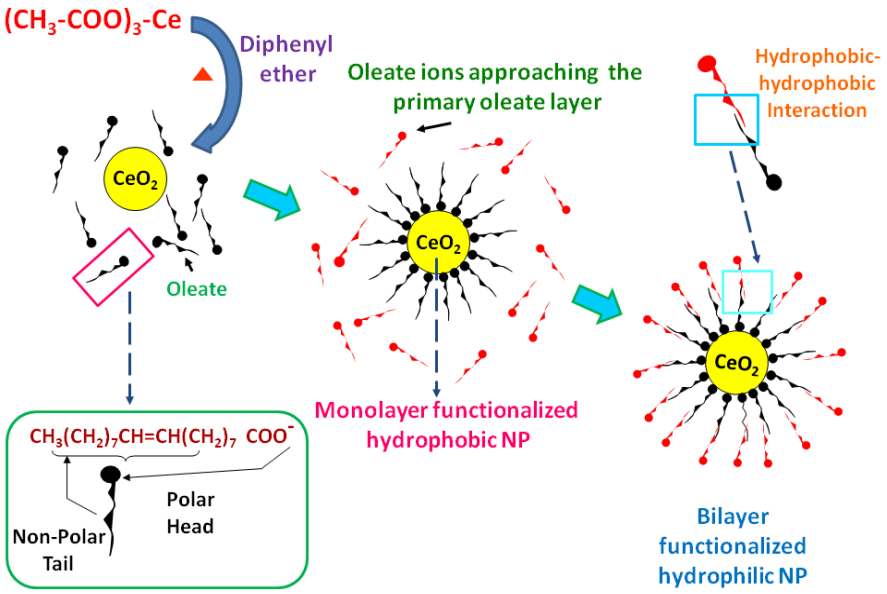

Scheme 4.2 Synthetic Protocol for the bilayer surface functionalisation.

The visual change in the appearance of the nanoparticles after bilayer modification has been depicted in Fig. 4.1. It could be observed that whereas OANP had a sticky nature, BLNP was more powder like. This is an initial evidence for the change in the nanoparticle surface from hydrophobic to hydrophilic.

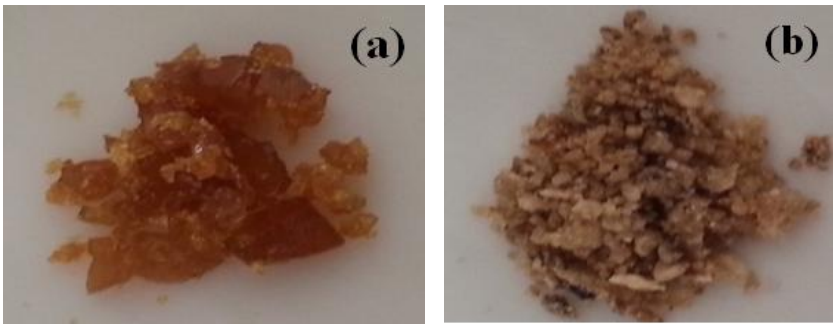

Fig. 4.1 Optical photographs of (a) OANP and (b) BLNP implying change in appearance after bilayer functionalisation.

The behaviour of the bilayer modified nanoparticle, BLNP in water was examined to evaluate the success in the adopted synthetic protocol. It was observed that BLNP was well dispersible in water to yield a stable aqueous suspension, thus justifying the experimental parameters for the bilayer functionalisation. The optical photographs of the nanoparticles suspensions in water as provided in Fig.4.2, confirm the hydrophilic nature of BLNP surface.

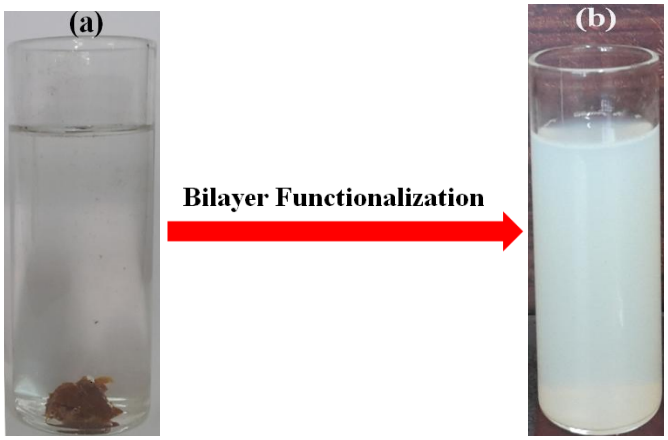

Fig. 4.2 The interaction of nanoparticles with water (a) OANP and (b) BLNP in aqueous media.

4.4.2 Preliminary Characterisation

The XRD pattern of BLNP shown in Figure 1, revealed that the core of the nanoparticle belongs to pure face-centred cubic fluorite phase of ceria with the space group *Fm*3*m* (JCPDS no. 43-1002).[68] The characteristic peaks in the diffractogram has been indexed to the reflections from the crystal planes in the (111), (220), (311) and (331) directions as denoted in the figure.[69]

It could be concluded that synthetic procedure involving bilayer functionalisation has not created any alteration in the crystal structure of the nanoparticle core. Also it could be noted in mind that any change brought about by the modification process is limited only to the surface of the nanoparticle. The

extremely broadened XRD peaks as similar to OANP indicate the nanoscale of the crystallites.

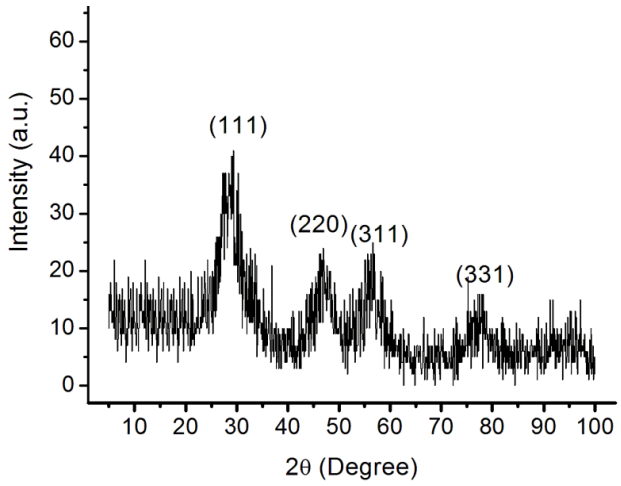

Fig. 4.3 X-ray diffraction patterns of BLNP showing the characteristics peaks corresponding to the crystal facets of ceria.

HR-TEM images of BLNP, as shown in Figure 4.4 vividly illustrate that the spherical morphology as well as the size of the nanoparticle was retained even after modification by the second layer. The calculated average size on 100 particles was 2.2 ± 0.2 nm, almost same as that of OANP, indicating the absence of any crystal growth during the synthetic process.

TEM images show that OANP produced well separated nanoparticles. Slight aggregation of BLNP compared to that in OANP may be attributed to the electrostatic attraction between the nanoparticles owing to the slightly polar C=O group over the BLNP surface, which overcame the sterric repulsion induced by the surfactants between the particles. The visual examination of the exposed crystal facets of BLNP indicate that the lattice fringes corresponds to predominant (111) and (100) planes of ceria with corresponding interplanar spacing of 0.31 nm and 0.27 nm respectively, indicating the crystal purity of the core structure.

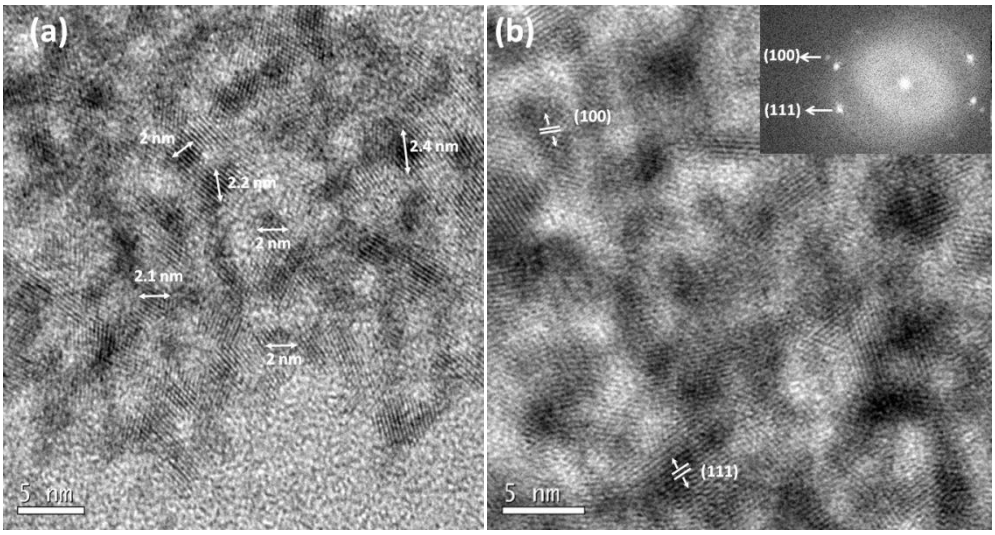

Fig. 4.4 HR-TEM images of BLNP (a) showing the size of particles and (b) indicating the exposed crystal facets.

The hydrodynamic size of BLNP in the aqueous medium has been showed in Fig. 4.5. The D_{PCS} value of the nanoparticle is higher than the D_{TEM} and the difference as already discussed in the second chapter, D_{TEM} provides only the core size of the nanoparticle, D_{PCS} considers the size of the core-shell structure comprising of nanoparticle and oleic acid.[70]

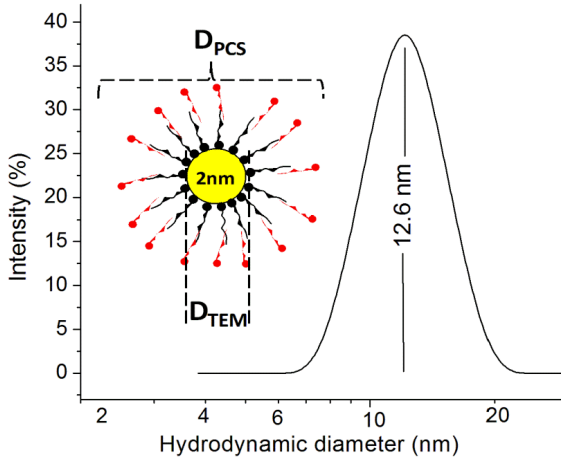

Fig. 4.5 The photon correlation spectra of BLNP in water for deriving its hydrodynamic diameter.

Earlier in the second chapter, the D_{PCS} of OANP was evaluate to be 4.5 nm which was justified by considering the effective chain length of oleic acid, ~1 nm on

both sides of the 2 nm sized central ceria core. While considering two layers of oleic acid over the surface, the theoretical D_{PCS} of BLNP is ~6 nm, i.e., 4 nm corresponding to two oleic acid groups on both sides, along with the central 2 nm core. But the experimental value of ~12 nm was slightly higher, which may be due to the scattering of photons from more than one particle aggregated together *via* electrostatic attraction induced by the surface polarity after bilayer functionalisation.

4.4.3 Surface properties of the nanoparticles

The thermogravimetric profiles of the samples, OANP and BLNP as shown in Fig. 4.7(a) shows significant loss in weight between 240 to 450ºC on account of the surfactants present on the surface of the nanoparticles. OANP showed a single step weight loss corresponding to the monolayer chemisorbed oleate ions over the nanoparticles. The bilayers of surfactant in BLNP resulted in a two step weight loss in its thermal stability data, the first and the second step being related to the outer and inner layers respectively.

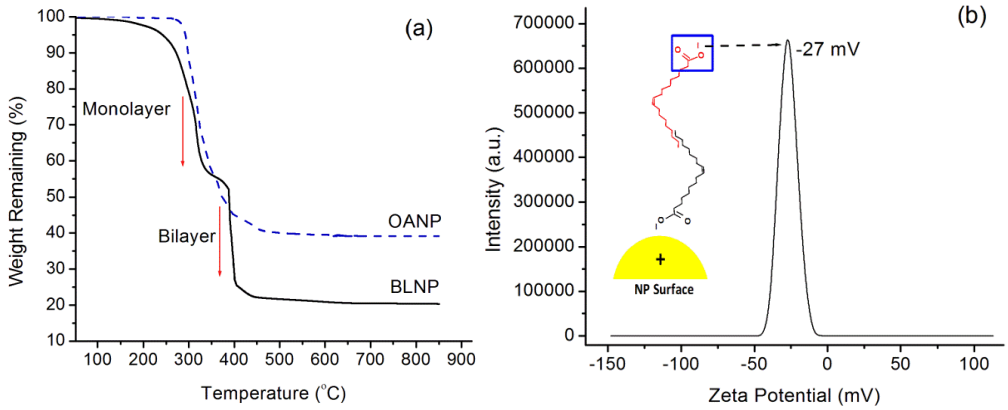

Fig.4.7 (a) The thermogravimetric profiles of OANP and BLNP, and (b) zeta potential measurement of BLNP in water.

As the outer layer is linked to the inner layer by relatively weak hydrophobic-hydrophobic interaction, the oleate ions in that layer could get rid of the chemical

force and undergo decomposition at a lower temperature compared to that in the inner layer. In the primary layer, owing to the strong chemisorption between the oleate ions and the nanoparticle surface, the surfactant molecules undergo decomposition at a slightly higher temperature as implied by the TGA. In fact, the two-step weight loss in BLNP implies the effectiveness of surface functionalisation proffered by the adopted synthetic strategy.

In order to evaluate the surface charge of the particles after bilayer surface functionalisation, the zeta potential of the aqueous BLNP dispersion (pH ~7) has been measured and given as Fig. 4.7(b). The particles showed a negative zeta potential value of about -27 mV which is attributed to the negative carboxylate groups projected out of the nanoparticle surface after bilayer modification. The value, which in turn implies the polarity over the surface, indicates the successful grafting of hydrophilic layer over the nanoparticles by functionalisation.

The change in the nature of the nanoparticles from hydrophobic to hydrophilic has also been demonstrated in Fig. 4.8, which reveals the water contact angle measurements of glass slides coated with dispersions of OANP and BLNP.

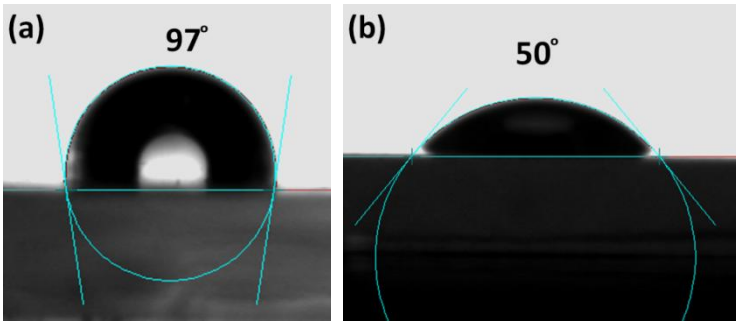

Fig. 4.8 Sessile drop water contact angle measurement of glass slide coated with (a) OANP and (b) BLNP.

The wetting behaviour exhibited by the particles before and after bilayer functionalisation was drastically different. Whereas OANP coated surface made a

contact angle of 97º with water, which falls in the hydrophobic range, glass slide with BLNP over the surface exhibited a hydrophilic contact angle of 50º. The difference in wettability of the two samples is featured by the change in the functional groups present over the particle surface brought about by bilayer modification. In OANP, due to the non-polar alkyl chain over the nanoparticle, the surface is rather hydrophobic as implied by Fig. 4.8(a). On the other hand, the surface polarity of BLNP as endowed by the carboxylate group, due to the tail-tail manner of attachment of the alkyl chains in the two layers, rendered the glass surface hydrophilic.

The hydrophilic surface of BLNP facilitated its dispersion in water, which was stable over a period of several weeks. The turbidity measurement of the dispersion for more than 1 month has been tabulated in Table 4.2.

Table 4.2 Turbidity Measurement data of BLNP aqueous dispersion

Time of Ageing (Days)	Turbidity (NTU)	Decrease in Turbidity (%)
1	22	0
7	19	13
14	19	13
21	19	13
28	19	13
35	19	13

Even though, the initial value of the turbidity *i.e.*, 22 NTU was slightly decreased to 19 NTU after 1 week, later, the dispersion showed a consistency in the values for more than 1 month. The dispersion did not show any visible change in

appearance or formation of precipitate over the time of ageing. The zeta potential value of the dispersion, -27 mV also indicates the stability of the dispersion, as the values in the range 25–30 mV specifies the electrostatic stabilisation of the nanoparticles.[71] Thus the turbidity data, along with the zeta potential of the dispersion corroborates the higher stability offered by the hydrophilic nanoparticles in water.

4.4.4 Optical properties of the nanoparticles

The absorption and emission spectra of BLNP is depicted in Fig. 4.9. The particles showed its absorption edge at ~400 nm and the corresponding emission was in the

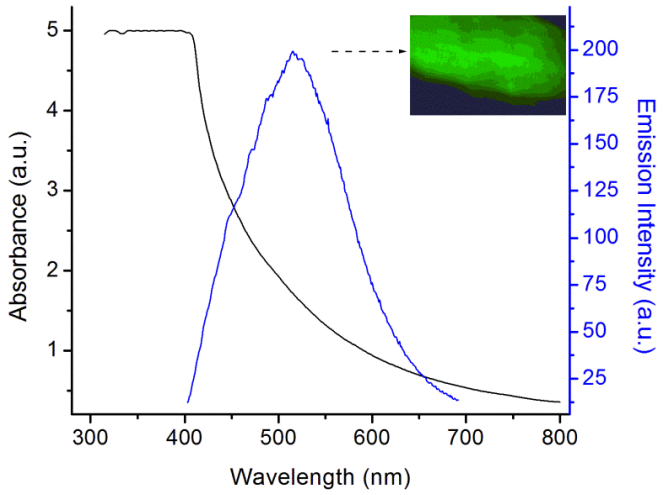

Fig. 4.9 UV and PL spectra of BLNP showing its absorption and emission in the visible region. The inset shows the visual image of the green coloured emission.

visible region with its emission maximum at 515 nm in the green region. It could be understood that the bilayer functionalisation process does not have any impact on the nanoparticles core and retained its size induced green coloured emission. The observation is not a surprising piece of information because, as disclosed by TEM and XRD, bilayer modification does not have any direct influence on the properties of the central nanoparticle. The only notable effect is a subsequent increase in its

hydrodynamic diameter along with surface hydrophilicity, which is least expected to induce an alteration in the optical properties of the core.

In the second chapter, the green coloured emission of the OANP, as a result of red shift in optical properties has been attributed to the size related increase in Ce^{3+} to Ce^{4+} ratio in the crystal. It was postulated that the higher Ce^{3+} ions in the crystal lattice create an intermediate band in between the valence and conduction bands of ceria. As a result, the excitation of electrons from valence band occurs to this new band, which is of lower energy than the conduction band. Thus the overall energy of absorbance was lowered to bring up a red shift in optical properties. Consequently, the absorption edge of the particles will be shifted to 400 nm with a strong emission in the visible region. As an evidence of the postulate, the total Ce^{3+} content in OANP has been assessed in the second chapter using XPS spectroscopy, which came out to be ~42%.

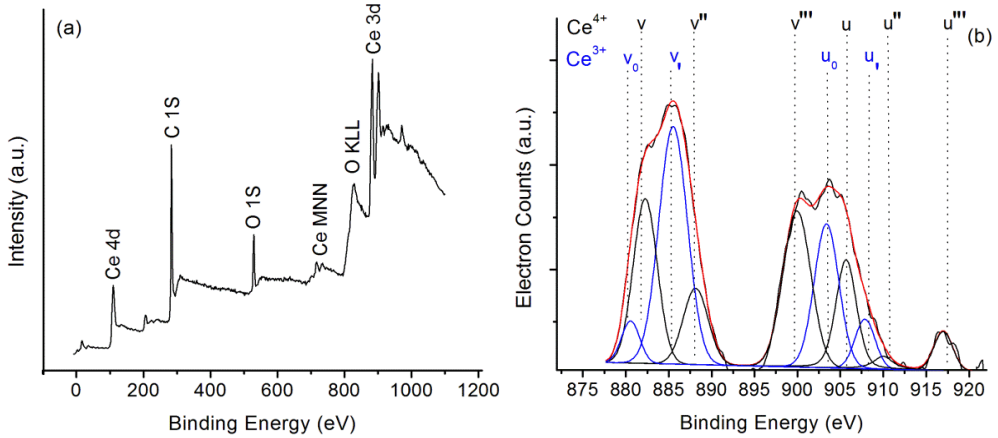

Fig. 4.10 XPS spectra of BLNP (a) Survey spectrum, and (b) deconvoluted Ce 3d core level spectrum.

As the principle of the proposed sensor in the present context solemnly depend on the Ce^{3+} content, the XPS spectra of BLNP has also been procured, which is demonstrated in Fig. 4.10. The Ce^{3+} content of BLNP was calculated to be ~38%

which is almost similar to OANP. Thus it could be presumed that the consistent optical property of the nanoparticles even after a second step modification is because the total Ce^{3+} content is almost same for both OANP and BLNP. Also it could be confirmed that the refunctionalisation process does not have much effect on the Ce^{3+} content and the related redox ability of the particles is preserved as such.

4.4.5 Sensing of vitamin C by the nanoparticles

With respect to the optical properties of the nanoparticles, the role of Ce^{3+} is pivotal in the fluorescence exhibited by the nanoparticles. The dependence of fluorescence on the Ce^{3+} content has been verified by monitoring the emission intensity of the nanoparticles with varying Ce^{3+} concentrations. Being an oxidising agent, $KMnO_4$ has been used as a mediator to vary the Ce^{3+} content in BLNP dispersion. $KMnO_4$ converts Ce^{3+} to Ce^{4+} according to the equation [46]

$$3Ce^{3+} + MnO^{4-} + 2H_2O \rightarrow 3Ce^{4+} + Mn^{4+} + 4OH^- \quad (1)$$

Different amounts of $KMnO_4$ were added to BLNP dispersions (0.0008 M), the PL spectra of which are shown as Fig. 4.11.

It was observed that, the PL spectra showed a relative decrease in intensity with respect to the amount of $KMnO_4$ added. This is because, as Ce^{3+} is oxidised to Ce^{4+} by $KMnO_4$, the abundance of the intermediate energy level created by Ce^{3+} in the band gap will be inversely affected. The consequential decrease in exciton transfer to the Ce^{3+} band allocated the diminishing of fluorescence exhibited by the nanoparticles.

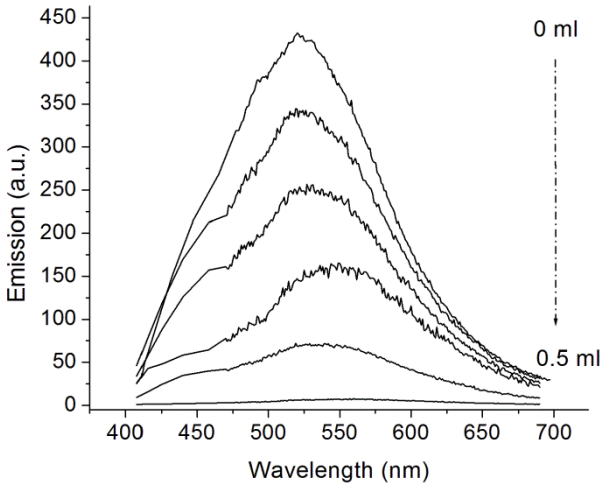

Fig. 4.11 The PL spectra of BLNP dispersion showing quenching of fluorescence with the addition of different volume of $KMnO_4$ solution.

The oxidation of Ce^{3+} to Ce^{4+} could also be observed visually by examining the colour change of the BLNP dispersion. The BLNP dispersion which was initially bluish-white in colour gradually changed to yellowish, after the addition of $KMnO_4$, indicating the formation of Ce^{4+} in the dispersion. The optical photograph of the dispersions before and after the addition of $KMnO_4$ has been supplied as Fig. 4.12.

Fig. 4.12 Visual change in the colour of BLNP dispersion to yellowish, after the addition of $KMnO_4$, indicating the oxidation of Ce^{3+} to Ce^{4+}.

The amount of $KMnO_4$ needed to quench the fluorescence of BLNP dispersion under the preferred experimental conditions has been optimised to 0.5 ml, the addition of which extinguished the fluorescence of the nanoparticles almost completely.

The principle of the present nanoparticle based sensor is laid on the fact that the reverted conversion of Ce^{3+} to Ce^{4+} by vitamin C can fetch the extinct fluorescence to its initial vigour. The structure of vitamin C is such that the two enolic hydroxyl groups attached to the C3 and C2 carbon of the lactone ring are prone to release electron under favourable conditions so as to form the comparatively stable and oxidised deprotonated intermediate.[20]

$$2Ce^{4+} + \underset{\text{(Vitamin C)}}{C_6H_8O_6} \rightarrow 2Ce^{3+} + C_6H_6O_6 + 2H^+ \qquad (2)$$

The sensing of vitamin C by nanoparticles stems from its the ability to convert the oxidised Ce^{4+} back to Ce^{3+} by the donation of electron as represented as shown in Scheme 4.3. The stoichiometric equation displaying the interaction between vitamin C and cerium ions is shown as equation (2).[46]

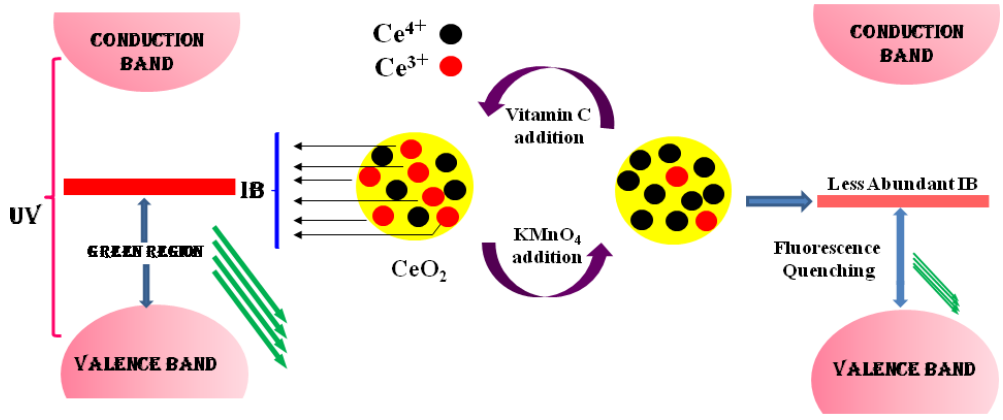

Scheme 4.3 Representation of the principle behind the sensing of vitamin C by ceria nanoparticles.

Different amounts of vitamin C in water at concentration range of µM to mM have been added to BLNP dispersions, whose fluorescence has been quenched by the oxidation of Ce^{3+}. Upon addition of vitamin C, the oxidised cerium ions (Ce^{4+}) will return to their initial +3 state along with the regain of the extinct fluorescence. The analysis of PL spectra of the respective dispersions revealed that the intensity of emission by the nanoparticles is in fact a function of the concentration of vitamin C present in the dispersion. The PL intensity of the dispersion showed a linear correlation with the concentration of vitamin C as indicated in Fig. 4.13. The linearity could be observed over a wide range of concentration of vitamin C solution (µM to mM). However, there was no observable increase in PL intensity upon addition of vitamin C solution with concentration above ~2.6×10^{-4} M. Here the noteworthy fact is that, at this concentration, the PL spectra have almost regained its initial intensity implying complete retrieval of Ce^{4+} to Ce^{3+}. Fig. 4.13(b) shows the linear regression of the variation in PL intensity with the addition of ultra dilute vitamin C solution (µM) with an R^2 value of 0.9963. The linearity implies the efficiency of the proposed sensor to quantify vitamin C under ultra dilution.

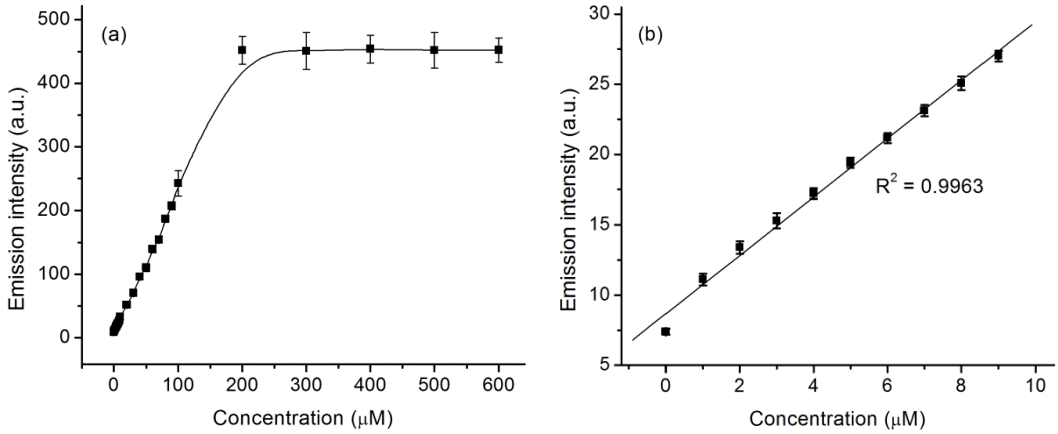

Fig. 4.13 (a) Variation in PL intensity of BLNP with the addition of different concentrations of vitamin C solution, and (b) linear fit of the PL intensity plotted against molarity of vitamin C at low concentration range.

The limit of detection (LoD) of the sensor, which is smallest analyte concentration that can be measured reliably by the proposed method, has been calculated as 3 times the standard deviation (σ) for replicates of the blank.[46] While the value of σ as 0.17 has been taken into consideration, the much lower LoD value compared to literature underlines the capability of the nanoparticles to sense vitamin C in solutions as dilute as 500 nM (5×10^{-7} M). In short, the dynamic range of detection of the sensor is assigned to be 10^{-7} to 10^{-4} M.

The selectivity of the sensor towards vitamin C in pharmaceutical formulations has been demonstrated in Fig. 4.14(a). Common pharmaceutical ingredients which are used as sweetening agents, stabilisers and binders have been employed along with BLNP and the PL spectra of the same was acquired.

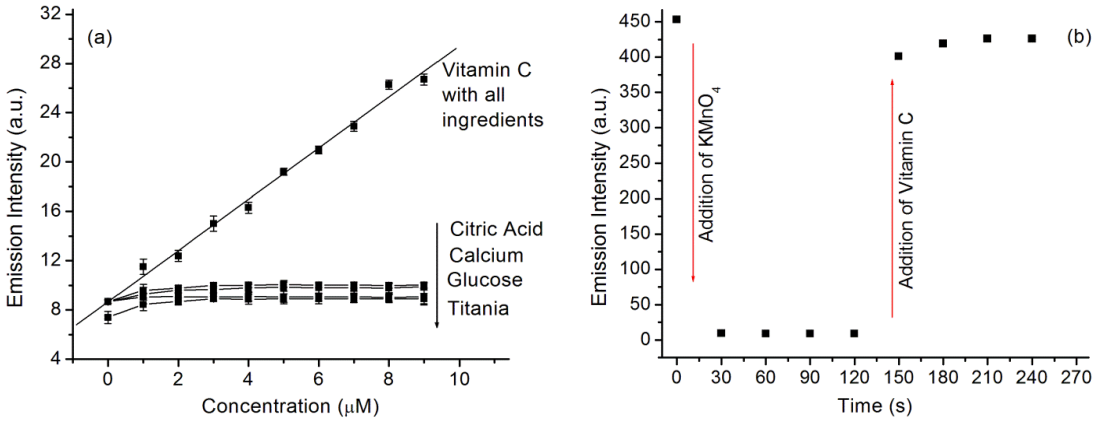

Fig. 4.14 (a) Variation in PL intensity of BLNP with the addition of different pharmaceutical ingredients at different concentrations. The same with the addition of vitamin C along with all ingredients is also shown (b) Time dependent variation in PL intensity of BLNP dispersion with the addition of $KMnO_4$ and vitamin C.

It was observed that almost all of the ingredients did not show any interaction with the nanoparticles so as to create any impact on its PL spectra. It is also revealed that any of the ingredients does not interfere with the interaction between vitamin C and the nanoparticles as implied by the retention of the linear progression of PL

intensity with vitamin C concentration in the presence of all ingredients. Fig. 4.14(b) illustrates that the response time of the sensor detecting vitamin C is within 1 min. The PL intensity of the dispersion as a function of time has been monitored and during the approach, the fluorescence was quenched and activated by the addition of $KMnO_4$ as well as Vitamin C. It was noticed that the PL intensity which was diminished by the addition of $KMnO_4$, could be resumed within 30 s after the addition of vitamin C.

In order to point up the reusability of the sensor, five consecutive addition of $KMnO_4$ followed by vitamin C was executed on the dispersion and the resultant PL intensity is featured as Fig. 4.15. The turn on/off behaviour of the nanoparticle emission intensity was retained even after 5 cycles without much difference in initial intensities. Thus the reversibility of fluorescence exhibited by the nanoparticles enhanced its long term usability, which is one among the prerequisites of a desirable sensor. Attempt has been made to elucidate the amount of vitamin C in some pharmaceutical formulations by means of the projected sensing procedure.

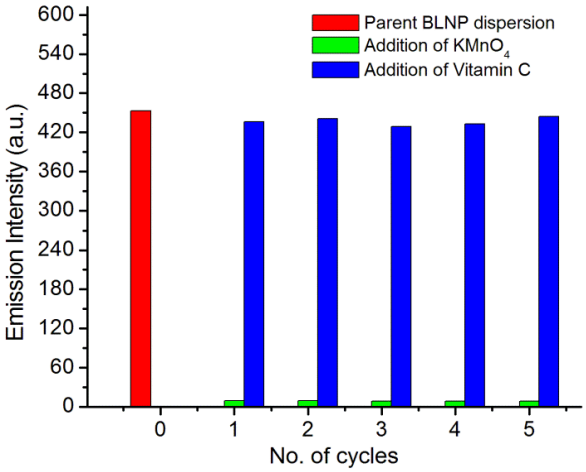

Fig. 4.15 Variation in PL intensity of BLNP with the alternate addition of $KMnO_4$ followed by vitamin C.

The tablets under study were dissolved in water so that its concentration falls in the µM range, which were added to BLNP, whose PL intensity was monitored. The amount of vitamin C in the tablet was deduced by means of this PL intensity and the linear calibration plot; the exact procedure is presented in detail in the experimental section. The results for the evaluation of vitamin C in real samples are presented in Table 4.3. The satisfactory RSD (Relative Standard Deviation) and Recovery % substantiates the reliable estimation of vitamin C in commercial formulations within error limits. Thus the practical applicability of the adapted method has been validated by the analysis of real samples.

Table 4.3 Calculation of vitamin C in commercial samples from linear progression of PL intensity against concentration

Sample	Replicates	PL Intensity (a.u.)	Concentration of vitamin C from linear plot (µM)	Amount of vitamin C per tablet (mg)	Mean	SD	RSD (%)	Recovery (%)
Tablet 1	1	15.58	3.35	590	528	56.32	0.107	105
	2	14.76	2.92	514				
	3	14.31	2.73	480				
Tablet 2	1	19.11	5.06	0.89	0.98	0.09	0.092	98
	2	20.02	6.13	1.08				
	3	21.3	5.51	0.97				

In short, without any tedious methodologies, expensive instrumentation or storage protocols, the presented method could rapidly and repeatedly sense vitamin C with high accuracy.

4.5 Conclusions

A novel turn–on fluorescent sensor based on cerium dioxide has been devised by a simple two step synthetic strategy. The principle of the sensor is relied on the redox property of ceria and its dependence on the size induced fluorescence. Nanosized ceria with average size 2.2 nm has been engineered by thermal decomposition approach. The oleophilic surface of the as synthesised nanoparticles has been renovated to hydrophilic by imparting a bilayer surface functionalisation. The consequent change in property was reflected in its surface polarity as well as wetting behaviour as revealed by the zeta potential and contact angle measurements. One of the appealing achievements of the demonstrated method is that, while the bilayer surface functionalisation allowed the surface of the particles hydrophilic, there was no inverse effect on the behaviour of the central ceria core including its optical and redox properties. The implemented hydrophilic features enabled the water compatibility of the nanoparticles to yield its aqueous dispersion, which exhibited long term stability. The emission intensity of the nanoparticles showed a quenching behaviour with respect to the oxidation of Ce^{3+} to Ce^{4+} in the nanoparticle dispersion by $KMnO_4$. The reversion of the oxidation state from Ce^{4+} to Ce^{3+} with the addition of vitamin C showed a linear increase in fluorescence intensity with concentration, thus enabling its quantitative assessment. The fascination with the proposed method is the efficiency to sense Vitamin C at a concentration as low as 500 nM with higher reproducibility, selectivity and rapidness, without any tedious protocol. The intriguing possibilities of the method for practical application have also been demonstrated by satisfactorily quantifying vitamin C in its commercial supplements with high accuracy.

4.6 References

1 T. Garcia, B. Solsona and S. H. Taylor, *Catal. Lett.*, 2005, **105**, 183-189.

2 S. Maensiri, C. Masingboon, P. Laokul, W. Jareonboon, V. Promarak, P. L. Anderson and S. Seraphin, *Cryst. Growth Des.*, 2007, **7**, 950-955.

3 P. Palmisano, N. Russo, P. Fino, D. Fino and C. Badini, *Appl. Catal. B*, 2006, **69**, 85-92.

4 M. G. Bellino, D. G. Lamas and N. E. W. de Reca, *Adv. Funct. Mater.*, 2006, **16**, 107-113.

5 Y. W. Zhang, R. Si, C. S. Liao and C. H. Yan, *J. Phys. Chem. B*, 2003, **107**, 10159-10167.

6 A. Corma, P. Atienzar, H. Garcia and J. Y. Chane-Ching, *Nat. Mater.*, 2004, **3**, 394-397.

7 M. Flytzani-Stephanopoulos, M. Sakbodin and Z. Wang, *Science*, 2006, **312**, 1508-1510.

8 R. W. Tarnuzzer, J. Colon, S. Patil and S. Seal, *Nano Lett.*, 2005, **5**, 2573-2577.

9 J. P. Chen, S. Patil, S. Seal and J. F. McGinnis, *Nature Nanotechnol.*, 2006, **1**, 142-150.

10 S. Patil, S. Reshetnikov, M. K. Haldar, S. Seal and S. Mallik, *J. Phys. Chem. C*, 2007, **111**, 8437-8442.

11 L. Almar, A. Tarancon, T. Andreu, M. Torrell, Y. Hu, G. Dezanneau and A. Morata, *Sensor Actuat. B*, 2015, **216**, 41-48.

12 M. M. Chakraboti, S. Dasgupta, S. Sengupta, J. Chakraborty, S. Ghosh, J. Ghosh, M. K. Mitra, A. Mishra, T. K. Mandal and D. Basu, *Ceram. Int.*, 2012, **3838** 941-949.

13 M. B. Gumpu, N. Nesakumar, S. Sethuraman, U. M. Krishnan and J. B. B. Rayappan, *Sensor Actuat. B*, 2014, **199**, 330-338.

14 M. Hosseini, M. R. K. Pur, P. Norouzi, M. R. Moghaddam, F. Faridbod, M. R. Ganjali and J. Shamsi, *Anal. Methods*, 2015, **7**, 1936-1942.

15 M. Singh, N. Nesakumar, S. Sethuraman, U. M. Krishnan and J. B. B. Rayappan, *J. Colloid Interf. Sci.*, 2014, **425**, 52-58.

16 D. Zhang, W. Wu, X. Ni, X. Cao, X. Zhang, X. Xu, S. Li, G. Han, A. Ying and Z. Tong, *J. Mat. Sci.*, 2009, **44**, 3344-3348.

17 A. Barberis, G. Bazzu, G. Calia, G. M. G. Puggioni, G. G. Rocchitta, R. Migheli, M. Schirra, M. S. Desole and P. A. Serra, *Anal. Chem.*, 2010, **82**, 5134-5140.

18 S. N. Faisal, M. M. Hossain and H. J. Lee, *J. Electrochem. Sci. Technol.*, 2010, **1**, 121-126.

19 Z. Gazdik, O. Zitka, J. Petrlova, V. Adam, J. Zehnalek, A. Horna, V. Reznicek, M. Beklova and R. Kizek, *Sensors*, 2008, **8**, 7097.

20 R. P. Tripathi, B. Singh, S. S. Bisht and J. Pandey, *Curr. Org. Chem.*, 2009, **13**, 99-122.

21 A. Abbaspour, A. Khajehzadeh and A. Noori, *Anal. Sci.*, 2008, **24**, 721-725.

22 Y. T. Chen, F. A. Isherwood and L. W. Mapson, *Biochem. J.*, 1953, **55**, 821-823.

23 H. Beitollahi, A. Mohadesi, M. Mostafavi, H. Karimi-Maleh, M. Baghayeri and A. Akbari, *Ionics*, 2013, **20**, 729-737.

24 S. S. Mitic, D. A. Kostic, D. C. Naskovic-Dokic and M. N. Mitic, *Trop. J. Pharm. Res.*, 2011, **10**, 105-111.

25 S. Lupu, A. Mucci, L. Pigani, R. Seeber and C. Zanardi, *Electroanal.*, 2002, **14**, 519-525.

26 J. Tillmans, P. Hirsch and W. Hirsch, *Untersuch. Lebensmitt*, 1932, **63, 1**

27 O. A. Bessey and C. G. King, *J. Biol. Chem.*, 1933, **103**, 687.

28 L. J. Harris and S. N. Ray, *Biochem. J.*, 1933, **27**, 580-589.

29 E. S. Tee, S. I. Young, S. K. Ho and S. S. Mizura, *Pertanika*, 1988, **11**, 39-44.

30 H. Tauber and I. S. Kleiner, *J. Biol. Chem.*, 1935, **108**, 563.

31 J. H. Roe and C. A. Kuether, *Science*, 1942, **95**, 77.

32 L. W. Mapson and S. M. Partridge, *Nature*, 1949, **164**, 479.

33 J. R. Kirk and N. Ting, *J. Food Sci.*, 1975, **40**, 463-466.

34 P. J. O'Connell, C. Gormally, M. Pravda and G. G. Guilbault, *Anal. Chim. Acta*, 2001, **431**, 239-247.

35 Y. Andreu, S. de Marcos, J. R. Castillo and J. Galban, *Talanta*, 2005, **65**, 1045-1051.

36 W. D. Mason and T. D. Gardner, *J. Pharm. Sci.*, 1972, **61**, 1301-1303.

37 M. Dominguez, A. Aldaz and Sanchez-Burgos, *J. Electroanal. Chem.*, 1976, **68**, 345.

38 J. J. Ruiz, A. Aldaz and M. Dominguez, *Can. J. Chem.*, 1977, **55**, 2799–2806.

39 X. Liu, X. Li, Y. Xiong, Q. Huang, X. Li, Y. Dong, P. Liu and C. Zhang, *Microchim. Acta*, 2013, **180**, 1309-1316.

40 B. B. Prasad, S. Srivastava, K. Tiwari and P. S. Sharma, *Mat. Sci. Eng. C*, 2009, **29**, 1082-1087.

41 V. K. Gupta, A. K. Jain and S. K. Shoora, *Electrochim. Acta*, 2013, **93**, 248-253.

42 S. A. Kumar, H. Cheng and S. Chen, *React. Funct. Polym.*, 2009, **69**, 364-370.

43 X. X. Wang, J.-M. Liu, S.-L. Jiang, L. Jiao, L. P. Lin, M. L. Cui, X. Y. Zhang, L.-H. Zhang and Z.-Y. Zheng, *Sensor Actuat. B*, 2013, **182**, 205-210.

44 S. Gheibi, H. Karimi-Maleh, M. A. Khalilzadeh and H. Bagheri, *J. Food Sci. Technol.*, 2015, **52**, 276-284.

45 H. W. Park, S. M. Alam, S. H. Lee, M. M. Karim, S. M. Wabaidur, M. Kang and J. H. Choi, *Luminescence*, 2009, **24**, 367-371.

46 W. Di, N. Shirahata, H. Zeng and Y. Sakka, *Nanotechnology*, 2010, **21**.

47 A. A. Ensafi, M. Taei, T. Khayamian and A. Arabzadeh, *Sensor Actuat. B*, 2010, **147**, 213-221.

48 M. Mazloum-Ardakani, M. A. Sheikh-Mohseni, H. Beitollahi, A. Benvidi and H. Naeimi, *Chin. Chem. Lett.*, 2010, **21**, 1471-1474.

49 M. J. R. Rama, A. R. Medina and A. M. Diaz, *Microchem. J.*, 2004, **78**, 157-162.

50 P. Tomcik, M. Krajcikova and D. Bustin, *Talanta*, 2001, **55**, 1065-1070.

51 A. A. Behfar, N. Sadeghi, B. Jannat and M. R. Oveisi, *Iran. J. Pharm. Res.*, 2010, **9**, 123-128.

52 P. Yang, X. Gao, L. Wang, Q. Wu, Z. Chen and X. Lin, *Microchim. Acta*, 2014, **181**, 231-238.

53 P. G. Veltsistas, M. I. Prodromidis and C. E. Efstathiou, *Anal.Chim. Acta*, 2004, **502**, 15-22.

54 A. Jo, M. Kang, A. Cha, H. S. Jang, J. H. Shim, N.-S. Lee, M. H. Kim, Y. Lee and C. Lee, *Anal. Chim. Acta*, 2014, **819**, 94-101.

55 J. C. B. Fernandes, L. T. Kubota and G. D. O. Neto, *Electroanal.*, 1999, **11**, 475-480.

56 A. A. Aziz and A. H. Kamel, *Talanta*, 2010, **80**, 1356-1363.

57 B. Kaur, T. Pandiyan, B. Satpati and R. Srivastava, *Colloid Surf. B*, 2013, **111**, 97-106.

58 D. Li, Y. Wen, H. He, J. Xu, M. Liu and R. Yue, *J. Appl. Polym. Sci.*, 2011, **126**, 882-893.

59 R. Koncki, T. Lenarczuk and S. Glab, *Anal. Chim. Acta*, 1999, **379**, 69-74.

60 G. P. Keeley, A. O'Neill, N. McEvoy, N. Peltekis, J. N. Coleman and G. S. Duesberg, *J. Mat. Chem.*, 2010, **20**, 7864-7869.

61 J. Singh, M. Srivastava, A. Roychoudhury, D. W. Lee, S. H. Lee and B. D. Malhotra, *J. Alloy Compd.*, 2013, **578**, 405-412.

62 H. M. Nassef, L. Civit, A. Fragoso and C. K. O'Sullivan, *Analyst*, 2008, **133**, 1736-1741.

63 G. Azimi, R. Dhiman, H.-M. Kwon, A. T. Paxson and K. K. Varanasi, *Nat. Mater.*, 2013, **12**, 315-320.

64 C. K. Kim, T. Kim, I. Y. Choi, M. Soh, D. Kim, Y. J. Kim, H. Jang, H. S. Yang, J. Y. Kim and H. K. Park, *Angew. Chem. Int. Edit.*, 2012, **124**, 11201-11205.

65 N. Rane, H. Zou, G. Buelna and J. Y. S. Lin, *J. Membrane Sci.*2005, **256**, 89-97.

66 E. Sharpe, T. Frasco, D. Andreescu and S. Andreescu, *Analyst*, 2013, **138**, 249-262.

67 L. Shen, A. Stachowiak, S. E. K. Fateen, P. E. Laibinis and T. A. Hatton, *Langmuir*, 2001, **17**, 288-299.

68 P. Maitarad, D. Zhang, R. Gao, L. Shi, H. Li, L. Huang, T. Rungrotmongkol and J. Zhang, *J. Phys. Chem. C*, 2013, **117**, 9999-10006.

69 M. Mari, B. Mueller, K. Landfester and R. Munoz-Espi, *ACS Appl. Mater. Interfaces*, 2014, **7**, 10727-10733.

70 T. S. Sreeremya, K. M. Thulasi, A. Krishnan and S. Ghosh, *Ind. Eng. Chem. Res.*, 2012, **51**, 318-326.

71 M. Bloemen, W. Brullot, L. Tai Thien, N. Geukens, A. Gils and T. Verbiest, *J. Nanopart. Res.*, 2012, **14,** 1100-1110.

Instrumental methods

Introduction: In this section, the basic principles and instrumental details of various characterization techniques adopted for the samples mentioned throughout the thesis will be described.

Characterisation techniques

X-ray diffraction (XRD) is a non-destructive analytic tool for deriving the detailed information about the crystallographic structure, phases, in polycrystalline samples and other structural parameters such as average grain size, crystallinity, strain and crystal defects and chemical composition, and physical properties of materials and thin films. When an X-ray beam hits an atom, the electrons around the atom start to oscillate with the same frequency as the incoming beam. In almost all directions we will have destructive interference, that is, the combining waves are out of phase and there is no resultant energy leaving the solid sample. However the atoms in a crystal are arranged in a regular pattern, and in a very few directions we will have constructive interference. The waves will be in phase and there will be well defined X-ray beams leaving the sample at various directions. Hence, a diffracted beam may be described as a beam composed of a large number of scattered rays mutually reinforcing one another. In short, when X-rays interact with a crystalline substance, one gets a diffraction pattern. The peak intensities are determined by the atomic orientation within the lattice planes. The interaction of the incident rays with the sample produces constructive interference when conditions satisfy Bragg's Law,

$$n\lambda = 2d \sin\theta \qquad (1)$$

where *n* is the order of diffraction, *d* is the interplanar spacing and θ is the angle of diffraction. By scanning the sample through a range of 2θ angles, all possible diffraction directions of the lattice should be attained due to the random orientation of the powdered material. Conversion of the diffraction peaks to *d*-spacings allows identification of the mineral because each mineral has a set of unique *d*-spacings.

In the present study, the phase composition of the solid products were determined from the powder X-ray diffraction patterns collected at room temperature using a Philips X'PERT PRO diffractometer with Ni-filtered CuKα_1 radiation (λ = 1.5406 Å). The X-ray data was collected on oven dried powders in the 2θ range 15–100 degree at a scanning rate 2° min^{-1} with a step size 0.04°. The crystallite size of the ceria powders was calculated from the line broadening of the XRD patterns using the Scherrer equation

$$D = \frac{0.9\lambda}{\beta \cos\theta} \qquad (2)$$

The lattice parameter of the cubic crystal can be calculated from the position of the observed diffraction lines in the XRD pattern, according to the following relation,

$$a = \lambda \frac{\sqrt{(h^2 + k^2 + l^2)}}{2\sin\theta} \qquad (3)$$

where *a* is the lattice parameter and *h, k, l* are the Miller indices of the considered Bragg reflection. The lattice strains ε were calculated using the Stokes–Wilson formula,

$$\varepsilon = \frac{\beta}{4\tan\theta} \qquad (4)$$

Thermogravimetric analysis (TGA) is used to study mass changes in a material due to physico-chemical or chemical changes in a material as a function of temperature. In this method, the sample is placed on a high-precision balance and subsequently heated

following a given temperature program. During the heating process, sample loses weight due to its decomposition on supply of heat which is monitored by a precision balance. The thermogravimetric profile is obtained as the plot of sample weight against temperature from which the thermal stability of the components can be interpreted. In the present study, TGA has been carried out on powder samples using a Perkin Elmer, STA 6000 thermogravimetric analyser in nitrogen/air atmosphere heated at a constant rate of 10 °C min^{-1} under nitrogen purge.

FT-IR spectroscopy is a spectroscopic technique used to identify the functional groups in ceria by making use of the energy involved in different bond vibrations in the materials. When electromagnetic radiations representing the IR region with the wavenumber range 400-4000 cm^{-1} are transmitted through the sample, it is absorbed by the functional groups present in the specimen for bond vibrations. As the frequency of energy absorbed depends on the masses, chemical environment of the atoms and the type of vibration, the resulting spectrum can easily convey the particular groups present in the sample. Fourier transform infrared (FTIR) spectra of the as prepared products were recorded at room temperature using the KBr (Sigma Aldrich, ~ 99%) pellet method on a Nicolet Magna IR-560 spectrometer ranging from 400 to 4000 cm^{-1} with average of 50 scans.

UV–visible spectroscopy refers to the absorbance or reflectance spectroscopy in the ultraviolet-visible spectral region between 190 nm to 800 nm which is divided into the ultraviolet (UV, 190–400 nm) and visible (Vis, 400-800 nm) regions. Molecules on irradiation with the UV-visible radiations undergo electronic transitions on absorbing the corresponding energy, the amount of energy absorbed being dependent on the structure of the compound. Therefore the absorbance spectrum of a molecule often serves as source

of identification of its electronic state. As a molecule absorbs energy, an electron is promoted from an occupied molecular orbital, usually a non-bonding *n* or bonding π orbital to an unoccupied anti-bonding molecular orbital, π∗ or σ*. In short, the molecule may undergo several energy transitions which is given in the increasing order of energy as *n* to π* < *n* to σ * < π to π* < σ to π* < σ to σ*. Since all these transitions require fixed amount of energy, the UV-Visible spectrum of a compound would consist of one or more well defined peaks, each corresponding to the transfer of an electron from one electronic level to another. The intensity of absorption is in accordance with Beer's and Lambert's Law which states that the fraction of incident radiation absorbed is proportional to the number of absorbing molecules in its path. Thus UV-Visible spectroscopy is a powerful analytical tool for the qualitative as well as quantitative assessment of molecules.

The measurements are usually carried out in very dilute solutions and the most important criterion in the choice of solvent is that it must be transparent within the wavelength range being examined. For preparing stock solutions, the sample is accurately weighed and made up to volume in volumetric flask. Aliquots are removed from this solution and appropriate dilutions are made to make solutions of desired concentration. For recording the spectrum 1 cm square quartz cell is commonly used which requires ~3 ml of solution. The quartz cell containing solution is placed in the path of light beam and spectrum is recorded by varying the wavelength of incident light. The spectrum can also be deducted from well powered solid samples which use special sample holders. In the present study, the absorbance spectra of the samples were obtained using a UV-visible 2401 PC spectrophotometer (Shimadzu, Japan) in the wavelength range of 200–800 nm. The absorbances of surface modified samples were conducted in their corresponding

dispersions, water and toluene being the dispersion media for hydrophilic and hydrophobic samples respectively. For bulk and uncoated samples, the measurements were done on powdered samples.

Photoluminescence spectroscopy is a non-contact, non-destructive method of probing the electronic structure of materials. In essence, light is directed onto a sample, which absorbs it to undergo a process called photo-excitation in which, the electron is excited to a higher electronic level. Following excitation, the fate of this species is varied, depending upon the exact nature of the surroundings, but the end result is deactivation or loss of energy and return to the ground state. The main deactivation processes which occur are fluorescence (loss of energy by emission of a photon), internal conversion and vibrational relaxation (non-radiative loss of energy as heat to the surroundings), and intersystem crossing to the triplet manifold and subsequent non-radiative deactivation. Time periods between absorption and emission may vary from short femto second regime for emission involving free-carrier plasma in inorganic semiconductors up to milliseconds for phosphorescent processes in molecular systems and under special circumstances delay of emission may even span to minutes or hours. Photoluminescence spectroscopy monitors the energy emitted by the excited electron which could give vital information regarding its electronic structure. In a typical procedure, the sample is usually excited using radiation of wavelength corresponding to its maximum absorbance (λ_{max}). The measurement can be done for solid as well as liquid sample as in the case of UV-Visible spectroscopy. The photons emitted by the sample after relaxation from the excited level to ground state with definite time intervals would be recorded which could

provide the luminescence property of the material along with time related luminescence decay.

Fluorescence occurs when a molecule in an excited state's lowest vibrational energy level returns to a lower energy electronic state by emitting a photon and as a result, the molecule possesses unique luminescence behaviour. A quantitative expression of fluorescence efficiency is the fluorescent quantum yield, ϕ, which is the fraction of excited state molecules returning to the ground state by fluorescence. The most reliable method for recording ϕ is the comparative method which involves the use of well characterised standard samples with known ϕ values. Essentially, solutions of the standard and test samples with identical absorbance at the same excitation wavelength are prepared which is assumed to be absorbing the same number of photons. Later the fluorescence spectra of the two samples are recorded and the peak area is deduced. A simple ratio of the integrated fluorescence intensities of the two solutions recorded under identical conditions will yield the ratio of the quantum yield values. Since ϕ for the standard sample is known, the ϕ of the sample can be derived using the equation

$$\phi_{overall} = \frac{n^2 A_{ref} I}{n_{ref}^2 A I_{ref}} \phi_{ref} \qquad (5)$$

where *n*, *A*, and *I* denote the refractive index of solvent, the absorbance at the excitation wavelength and the area of the emission spectrum, respectively, and ϕ_{ref} represents the quantum yield of the reference solution. In the present study, the photoluminescence measurements of samples were taken at room temperature using a Cary Eclipse spectrofluorometer (Varian, Australia). As discussed in UV-Visible spectroscopy, both nanoparticle dispersions as well as powdered samples were used during measurements. For calculating the quantum yield of the oleic acid coated samples, the nanoparticle

dispersion in toluene were employed and its ϕ was measured relative to a reference solution of quinine sulphate in 1 N sulphuric acid possessing a ϕ = 54.6%.

Transmission electron microscopy is a technique developed to obtain higher magnification images of samples to a much better level than the conventional optical microscopes. In TEM, a beam of electrons are accelerated up to high energy levels in the order of keV and is passed through an ultra-thin specimen, specially prepared for imaging. As the beam interact with the material, the electrons gets scattered and back scattered either elastically or inelastically. When the scattered electron beam is focused on an imaging device, such as a fluorescent screen, or a layer of photographic film or detected by a sensor such as a CCD camera, it produces an image of the specimen. The image contrast arises from mass-thickness differences in the various region of specimen, where thicker portions scatter more electrons compared to thinner regions. Since the de-Broglie wavelength of electrons are significantly smaller than that of light, they can form images with higher resolution. Thus this technique enables to examine details as fine as a single column of atoms, which is tens of thousands times smaller than the smallest resolvable object in a light microscope. Obviously, TEM has emerged as a major analysis method in a range of scientific fields, in both physical and biological sciences. In nanotechnology, TEM is a one of the indispensable tool for getting information about the morphology, crystallite size, crystal structure, defects, crystal phases and composition, and magnetic microstructure.

In the present study, the morphology and average size of the ceria nanoparticles were investigated by high resolution transmission electron microscopy (HR-TEM) using a FEI Tecnai 30 G^2 S-Twin microscope operated at 300 kV and equipped with a Gatan

CCD camera. Samples were prepared by dropping a micro droplet of suspension of the dried nanoparticle on to a 400 mesh carbon-coated copper grid. The excess solvents were allowed to dry naturally by ageing for 1 day after preparation. For samples with hydrophobic surface, the suspensions were prepared by dispersing the particles in toluene with continuous ultra-sonication for 30 minutes. For other samples, acetone was used as the dispersion medium.

Raman spectroscopy is a spectroscopic technique making use of the vibrational, rotational and other low-frequency energy transitions in a system. It relies on the inelastic scattering of monochromatic light, usually from a laser source in the visible, near infrared, or near ultraviolet range. The laser light interacts with molecular vibrations, phonons or other excitations in the system and as a result, the energy of the laser photons will be either shifted up or down commonly called as 'Raman effect'. This shift in energy provides information about the vibrational modes in the system, which in turn serves as a fingerprint of the molecules under study. Typically, the sample is illuminated with a laser beam and the radiations from the illuminated spot are collected with lenses which are being sent through a monochromator. Elastic scattered radiations corresponding to the wavelength of the laser line is filtered out and the rest of the collected light is dispersed onto a detector by either a notch filter or a band pass filter. Raman spectra of the solid specimens in the present study were recorded at room temperature using RFS (Bruker) FT-Raman spectrometer with excitation by a 150 mW Nd:YAG laser operating at 1064 nm wavelength.

X-ray Photoelectron Spectroscopy (XPS) is a surface-sensitive quantitative spectroscopic technique, that measures the elemental composition at the parts per thousand range. The

spectrum is obtained by irradiating the sample with a beam of X-rays while simultaneously measuring the kinetic energy and number of electrons that escape from the top. The kinetic energy is measured by an electron energy analyzer which further determines the binding energy of the corresponding photoelectrons. From the binding energy and intensity of a photoelectron peak, the elemental identity, chemical state, and quantity of an element are determined. X-ray photoelectron spectra (XPS) of the samples under study were recorded on VG Microtech Multilab ESCA 3000 spectrometer maintaining a base pressure of the analysis chamber in the range of $3–6\times10^{-10}$ Torr. Mg Kα (1253.6 eV, line width 0.7 eV) was used as the X-ray sources. Selected spectra, especially N 1s and valence band spectra were recorded to eliminate the overlap between different Auger and/or core levels. Binding energy (BE) calibration was performed with Au $4f_{7/2}$ core level at 83.9 eV. The spectrum was recorded using a Peltier cooled CCD detector with an acquisition time of 10 s using a 5× objective.

Nephelometry is the measurement of the degree of attenuation of a radiant beam incident on particles suspended in a medium, the measurement usually being made perpendicularly to the incident beam. The measurement may be done with a standard photoelectric filter photometer or spectrophotometer with illumination at an appropriate wavelength. The method is based upon a comparison of the intensity of light scattered by the sample under defined conditions with the intensity of light scattered by a standard reference suspension. The higher the intensity of scattered light, the higher is the turbidity, which is represented in NTU's. A primary standard suspension usually, a formazin polymer is used to calibrate the instrument. A secondary standard suspension is used as a daily calibration check and is monitored periodically for deterioration using one

of the primary standards. The typical nephelometric instrumentation consists of a photocell placed so as to receive the scattered light from sample and measures the particle density which then is a function of the light reflected into the detector from the particles. In the present study, the turbidity of the ceria dispersions have been monitored using a nephelometer (CL 52D, ELICO, India) by measuring turbidity as a function of time.

Photon Correlation Spectroscopy (PCS) is technique based on dynamic light scattering, which can be used to determine the size distribution profile of particles in colloidal suspension. The principle of this technique is based on the constant and random Brownian motion of the colloidal particle. As large particles move slower than their smaller colleagues, the rate of fluctuation of the light scattered from them is also slower. This time delay causes the intensity of light scattered from the particles to form a moving speckle pattern which can be detected as a change in intensity of scattered light with time. Photon correlation spectroscopy uses the rate of change of these light fluctuations to determine the size distribution of the particles, using the Mie theory of light scattering. Typically, a laser is shot through as polarizer in the sample and the scattered is collected by a photomultiplier. Zeta potential measurements can also be done on the colloidal suspension using the same instrument in which the sample is placed in an electrical field. As the zeta potential arises due to the charge accumulation over particle surface, the measurement can be used to determine the sign of surface charge of the particles and also its electrophoretic mobility. The sample preparing procedure for the PCS analysis in the present study involved dispersing the fine ground well samples in suitable medium using

ultrasonication to obtain a stable suspension. For zeta potential measurement of bilayer surfactant coated samples, the inherent pH of the aqueous dispersion was ~7.

Contact angle measurements, is a quantitative measure of the wetting of a substrate by a liquid. It is defined geometrically as the angle, θ formed by a liquid at the three-phase boundary where a liquid, gas and solid intersect. The well-known Young equation describes the balance at the three-phase contact as

$$\gamma_{sv} = \gamma_{sl} + \gamma_{lv} \cos \theta \qquad (6)$$

The interfacial tensions, γ_{sv}, γ_{sl} and γ_{lv}, form the equilibrium contact angle of wetting, θ. A low contact angle value indicates that the liquid spreads on the surface while high contact angle values show poor spreading. If the contact angle is less than 90° it is said that the liquid wets the surface, indicating hydrophilic behaviour. A zero contact angle represents complete wetting. If contact angle is greater than 90°, the surface is considered as hydrophobic with non-wetting behaviour of the liquid. Contact angles can be divided into static and dynamic angles. Static contact angles are measured when droplet is standing on the surface and the three-phase boundary is not moving. When the three-phase boundary is moving, dynamic contact an-gles can be measured, and are referred as advancing and receding angles. The water contact angle measurements in the present study were made on glass substrates coated with sample dispersions by the static method. The experiment were performed by the sessile drop method in a Data Physics OCA 40 micro automatic contact angle instrument which is equipped with a contact angle goniometer and high resolution cameras and software to capture the profile of a pure liquid on a solid substrate. For the contact angle measurement, a micro syringe steel needle (Hamilton) of capacity 500 µL was positioned above the surface of the coated glass slide, and a drop of

the test liquid (3 µL) was dispensed at a rate of 1 µL s^{-1}. After dispensing, the drop, shape was monitored with a digital camera, and the contact angle was determined by aligning the tangent of the sessile drop profile at the contact point with the surface. The angle formed between the liquid/solid interface and the liquid/vapour interface is the contact angle and was an average of 5 measurements.

Summary of investigations

Cerium dioxide is a prolifically utilized rare earth oxide for a variety of applications on account of its unique physiochemical properties. The popularity of this oxide is an outcome of its ability to switch oxidation states between III and IV based on environmental conditions. Consequently, ceria has been explored as polishing agent, automotive exhaust controls, SOFC electrolyte, oxygen buffers, UV blockers, synthetic antioxidants etc. The impact of nanotechnology has boosted the efficiency of this material by virtue of the high surface area and higher oxygen vacancies associated with nanoscaling process. In spite of the positive impacts of nanotechnology on ceria based research, little is known about the emergence of novel size related optical properties in this oxide, in comparison with other semiconductor counterparts. On that point of view, present thesis involves the size controlled synthesis of ceria by employing different synthetic strategies like non-aqueous thermal decomposition and aqueous precipitation method with the assistance of different surfactants.

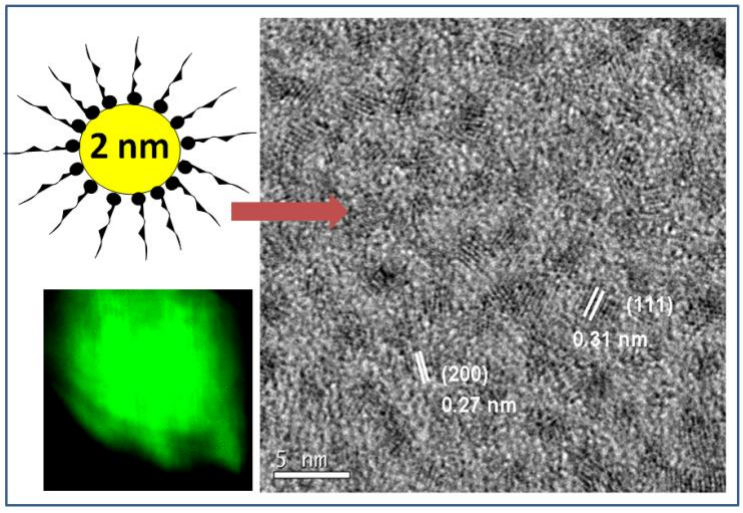

TEM image of the finest size ceria nanoparticles synthesised in the present study exhibiting green coloured fluorescence.

Accordingly, a set of ultra fine ceria nanoparticles with size preferably below 5 nm could be obtained by the adopted synthetic protocols, which have been presented in the second chapter of this thesis. Among these, the finest particles were of size ~2 nm, obtained by the thermolysis of cerium acetate in diphenyl ether in the presence of oleic acid as surfactant. Detailed spectroscopic investigation carried out on the synthesised samples in comparison with bulk ceria revealed that the nanoparticles exhibit a size dependent red shift in optical properties. When the dimension of the particles was reduced from bulk to 2 nm, the absorbance has undergone a shift of ~100 nm with a coloured emission in the green region. This observation was in contrast to the effect of size reduction in other semiconductor materials, in which the normal trend is a blue shift in optical properties. A mechanism have been proposed to justify the size related optical properties based on the higher concentration of Ce^{3+} and the associated defects originated in the nanocrystals which was corroborated by the XPS and Raman analysis. The present study also revealed that the size miniaturisation of ceria crystal is followed by a series of novel properties capable of imparting beneficial features to the oxide system.

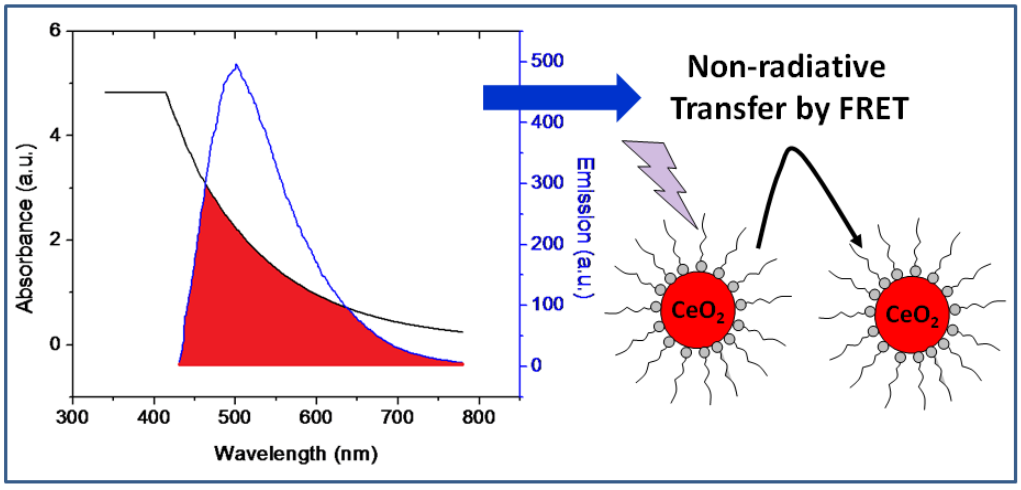

Spectral overlap of ceria nanoparticles facilitating the FRET based non-radiative energy transfer between them at higher concentration of dispersion.

The successful capping of oleic acid over the surface of the 2 nm sized ceria nanoparticles allowed its dispersibility in non-polar solvents to produce stable suspensions. The green coloured emission from the nanoparticle in the suspension exhibited a concentration dependent fluorescence quenching phenomenon. The studies carried out in the third chapter of this thesis proved that at higher concentration of suspension, when the particles are close to each other with an interparticle distance in the order of ~100 Å, they exchange the absorbed energy through a non-radiative pathway *via* Forster resonance energy transfer mechanism. The spectral data implied that the quenching phenomenon is brought about by the spectral overlap between the absorbance and emission spectra which is an outcome of the defects associated with the crystal during size miniaturisation. The fluorescence intensity exhibited an enhancement in intensity, when the distance between particles increases with respect to dilution of suspension. The distance dependence of FRET has been utilized to explicate the conformation and chain length of fatty acids, which has been endowed the role of spacers in the nanoparticle dispersions. As the distance created by the spacers in between the particles solemnly depends on their individual structures, the resulting fluorescence spectra serve as the structural signature of the fatty acid. Thus based on the concentration quenching phenomenon of nanoparticle dispersion *via* FRET, a simple analytical tool for the qualitative assessment of fatty acids have been projected in the third chapter.

In the last chapter, the practical applicability of the ceria particles under study has been improved by grafting a hydrophilic layer over its surface. This is brought about by a technique based on bilayer surface modification using oleic acid. Studies carried out in the chapter established the success in the accomplished strategy and the particles could be

well dispersed in water to produce stable dispersion. As the optical properties have dependence on the oxidation state of ceria, addition of an oxidising agent like $KMnO_4$ capable of converting the Ce^{3+} present in the sample to Ce^{4+}, in turn, quenched the fluorescence intensity of the dispersion. When vitamin C was added, the oxidation state of Ce ions reverted back to its initial state with an enhancement in emission intensity which depends on the concentration of the vitamin C.

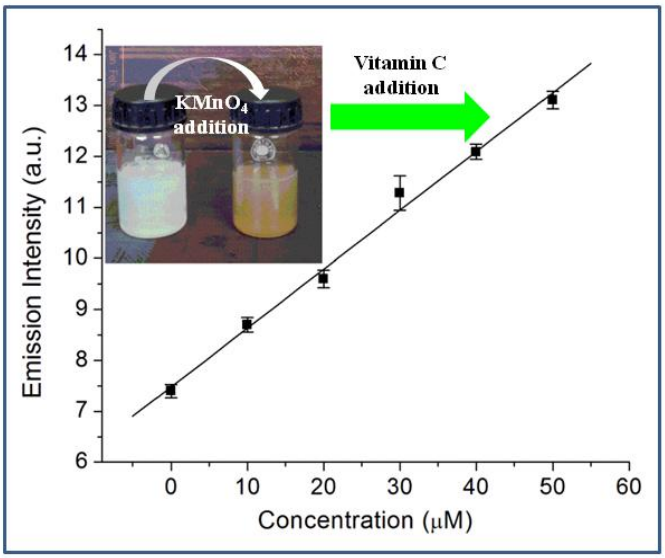

Linear response of emission intensity from fluorescence quenched ceria dispersion upon the addition of different concentrations of vitamin C.

In short, the emission intensity showed a linear response with concentration of vitamin C which was employed to sense the vitamin under ultra dilute conditions with concentration as low as 6 µM with higher reproducibility, selectivity and rapidness. The practical applicability of the designed sensor based on ceria nanoparticle was also demonstrated by successfully quantifying vitamin C in pharmaceutical formulations within satisfactory method.

LIST OF PUBLICATIONS

1. Morphological evolution and growth of cerium oxide nanostructures by virtue of organic ligands as well as monomer concentration, Asha Krishnan, Thadathil S. Sreeremya and Swapankumar Ghosh, ***CrystEngCommun*** 17 (2015) 7094–7106.

2. Concentration quenching in cerium oxide dispersions *via* a Förster resonance energy transfer mechanism facilitates the identification of fatty acids, Asha Krishnan, Thadathil S. Sreeremya, A. Peer Mohamed, Unnikrishnan Saraswathy Hareesh and Swapankumar Ghosh, ***RSC Adv***. 5 (2015) 23965–23972.

3. One-pot synthesis of ultra-small cerium oxide nanodots exhibiting multi-colored fluorescence, Asha Krishnan, Thadathil S. Sreeremya, Eoin Murray and Swapankumar Ghosh, ***J. Colloid Interf. Sci.*** 389 (2013) 16–22.

4. Dimension tuned hydrophilic cerium oxide nanoparticles as a 'turn-on' fluorescent sensor for the rapid detection of vitamin C under ultra dilution, (**Communicated**).

5. Shape Selective Oriented Cerium Oxide Nanocrystals Permit Assessment of the Effect of the Exposed Facets on Catalytic Activity and Oxygen Storage Capacity, Thadathil S. Sreeremya, Asha Krishnan, Kottayilpadi C. Remani, Kashinath R. Patil, Dermot F. Brougham and Swapankumar Ghosh, ***ACS Appl. Mater. Interfaces*** 7 (2015) 8545−8555.

6. Synthesis and characterization of cerium oxide based nanofluids: An efficient coolant in heat transport applications, Thadathil S. Sreeremya, Asha Krishnan, A. Peer Mohamed, U.S. Hareesh and Swapankumar Ghosh, ***Chem. Eng. J.*** 255 (2014) 282–289.

7. Facile synthetic strategy of oleophilic zirconia nanoparticles allows preparation of highly stable thermo-conductive coolant, Thadathil S. Sreeremya, Asha Krishnan Lakshmi N. Satapathy and Swapankumar Ghosh, ***RSC Adv***. 4 (2014) 28020– 28028.

8. Ultra-thin cerium oxide nanostructures through a facile aqueous synthetic strategy, Thadathil S. Sreeremya, Asha Krishnan, Srividhya J. Iyengar and Swapankumar Ghosh , ***Ceram. Int***. 38 (2012) 3023–3028.

9. A Novel Aqueous Route To Fabricate Ultrasmall Monodisperse Lipophilic Cerium Oxide Nanoparticles, Thadathil S. Sreeremya, Kunnambeth M. Thulasi, Asha Krishnan, and Swapankumar Ghosh, ***Ind. Eng. Chem. Res***., 51 (2012) 318–326.

Conference Proceedings

1. Poster entitled "Synthesis and optical properties of fluorescent cerium oxide nanoparticles", **Asha Krishnan**, et al., presented in the 78th ICS Conference, February 2-4th 2015, Kolkata.

2. Poster entitled "Surface modification of fluorescent cerium oxide nanocrystals from oleophilic to hydrophilic using CTAB as bilayer surfactant" **Asha Krishnan** et al. presented in the *International Conference on Advanced Functional Materials, February 2014,* Trivandrum.

3. Poster entitled "Novel size dependent optical properties in cerium oxide nano particles", **Asha Krishnan,** et al., presented in the National Seminar on current trends in chemistry, cTriC 2012 ,January 20-21, 2012, CUSAT, Kerala.

4. Poster entitled *"*Monodisperse ceria nanocrystals by facile aqueous method; phase transfer in to apolar solvents*",* **Asha Krishnan**, et al., presented in the DAE-BRNS 3rd International Symposium on Materials Chemistry, December 7-11, 2010, BARC, Mumbai.